NUCLEOTIDE-MEDIATED ALLOSTERY AND RECEPTOR BINDING BY THE MITOCHONDRIAL FISSION DYNAMIN

by

Raghav Kalia

A dissertation submitted to the faculty of
The University of Utah
in partial fulfilment of the requirements for the degree of

Doctor of Philosophy

Department of Biochemistry

The University of Utah

May 2018

The University of Utah Graduate School

STATEMENT OF THESIS APPROVAL

The thesis of **Raghav Kalia**

has been approved by the following supervisory committee members:

Adam Frost	, Chair	**January 2, 2018** Date Approved
Dennis R. Winge	, Member	**March 2, 2018** Date Approved
Wesley I. Sundquist	, Member	**March 8, 2018** Date Approved
Jared Rutter	, Member	**March 7, 2018** Date Approved
Diane M. Ward	, Member	**March 2, 2018** Date Approved

and by **Wesley I. Sundquist and Christopher P. Hill** , Chair/Dean of

the Department of **Biochemistry**

and by David B. Kieda, Dean of The Graduate School.

ABSTRACT

The morphology and function of mitochondria, the energy producing organelles of the eukaryotic cell, determine the fate of diverse cellular processes such as metabolic demand, embryonic development, and cell death. The cell uses a dedicated protein based machinery to divide mitochondria for distribution to daughter cells and to ensure faithful distribution of the mitochondrial genome. As a consequence, the impact of this division machinery applies to all processes that are influenced by the mitochondrial network. In mammals, this machinery is composed of the soluble protein Dynamin-Related Protein 1 and its membrane protein receptors Mitochondrial Dynamics 49kDa/51kDa (MiD49/51) and Mitochondrial Fission Factor (Mff). Drp1 forms assemblies that encircle the mitochondria. In addition, it binds and hydrolyzes the nucleotide guanosine triphosphate (GTP) which is thought to provide the necessary energy for mitochondrial membrane fission.

Although the importance of these proteins to the mitochondrial fission process is established, the mechanisms by which the receptor proteins recruit and mediate Drp1 activity are unknown. In this dissertation, I present functional and structural analyses of the interaction between Drp1 and its receptor proteins. In Chapter 3, I was a part of a study that showed that each single receptor can recruit Drp1 to the membrane of the mitochondria and cause mitochondrial fission. In Chapter 4, I extended this finding and used cryogenic electron microscopy (cryo-EM) to determine structures of Drp1 bound to

MiD49. These structures help us visualize Drp1 conformations in the recruited state on the mitochondrion and establish the role of nucleotide binding and hydrolysis on Drp1 activity. Specifically, we find that Drp1 assumes an extended conformational state upon nucleotide binding. This state enables Drp1 to bind to MiD49 and polymerize into filaments that are structurally suited to encircle mitochondrial tubules. Furthermore, the addition of GTP to this structure induces receptor dissociation and conversion to a ring-like state that is suited to constrict mitochondria. The dimensions of this ring-like state correspond to the Drp1 mediated constrictions observed in human cell cultures. Taken together, this work helps us understand the functional context for multiple receptors in mitochondrial fission and enables us to visualize the conformational dynamics of Drp1 required for its engagement with receptor proteins.

TABLE OF CONTENTS

CHAPTER 1

INTRODUCTION

1.1 Evolution, Organization, and Function of Mitochondria

Mitochondria originated when a primordial eukaryotic cell engulfed an α-proteobacterium, resulting in a symbiotic relationship. Some authors regard the primordial cell to be an archaebacterial cell that entered into a symbiotic relationship with another bacterium, resulting in the first ever eukaryotic cell (Gray, 2012; Henze & Martin, 2003). In any case, modern methods of phylogenetic analysis and sequencing have established the early bacterial origins of mitochondria with certainty.

In a typical cell in our body, mitochondria are essential organelles that produce adenosine triphosphate (ATP), the cellular energy currency (Andersson, Karlberg, Canback, & Kurland, 2003). Mitochondria are also home to the respiratory chain complexes, and play essential roles in lipid metabolism and calcium homeostasis (Mayr, 2014; Szabadkai et al., 2004). The normal course of embryonic development and cell death have also been linked to mitochondrial physiology and form (Chen et al., 2003; Estaquier & Arnoult, 2007; Flippo & Strack, 2017). Since mitochondria influence such a diverse set of cellular functions, disruption in normal mitochondrial health and shape leads to pathology.

Mitochondria have been depicted as bean shaped organelles as seen in cross sections of cells visualized by electron microscopy (Figure 1.1). The mitochondria are bound by a double membrane. Both the outer and inner mitochondrial membranes (OMM and IMM) are distinct in their lipid compositions and help in the compartmentalization of the organelle. The aqueous space between the two membranes is called the inner membrane space (IMS). The inner membrane encloses the bulk of the volume of the mitochondria. This volume is known as the matrix, and houses, among other proteins,

Figure 1.1 An image of a mitochondria: visualized with a transmission electron microscope. Image courtesy Louisa Howard, Dartmouth College, USA.

enzymes for respiratory pathways and the mitochondrial protein synthesis machinery. In addition, the inner membrane makes periodic invaginations into the matrix, called the cristae, which contain the protein machinery that produces ATP. The matrix of the mitochondria also contains mitochondrial DNA which encodes for some respiratory and translation machinery proteins (Kühlbrandt, 2015).

As a reservoir for calcium, mitochondria also perform critical roles in maintaining calcium levels in the cell. Calcium regulates the activity of multiple mitochondrial enzymes (Denton, 2009; Denton et al., 1980), and fluctuations in its levels are known to play a role in programmed cell death or apoptosis (Pinton et al., 2008). Apoptosis is accompanied by a loss of mitochondrial function, hyperfragmentation of the mitochondrial network, and the release of a respiratory enzyme cytochrome-c into the cytosol (Pinton et al., 2001; Szabadkai & Rizzuto, 2004; Szalai, Krishnamurthy, & Hajnóczky, 1999). Taken together, mitochondrial health and cellular well-being are interlinked.

1.2 Mitochondrial Dynamics and Human Health

Mitochondrial functions are diverse and mitochondria are not static organelles. Advances in fluorescence based microscopy have revealed mitochondrial motility within the cells (Nunnari et al., 1997; Okamoto & Shaw, 2005) and have enabled researchers to provide quantitative information on mitochondrial dynamics.

The processes that change mitochondrial morphology and distribution include mitochondrial fission, fusion, and transport (Bereiter-Hahn & Voth, 1994; Boldogh et al., 2001; Nunnari et al., 1997). The protein factors that are involved in these dynamic

processes have been discovered over the years using yeast genetic studies. Budding yeast has been widely utilized as a model organism to observe phenotypes of gene deletions. For mitochondrial dynamics, this system has provided critical hints about the factors responsible for mitochondrial fission, fusion, and transport.

Why would mitochondria divide or fuse? A balance of fission and fusion of mitochondria is critical for the organelles to exchange their DNA, prevent the spread harmful mutations and recycle damaged or old organelles (Twig, Hyde, & Shirihai, 2008). For this reason, multiple disorders are known to occur when mitochondrial fission or fusion go awry in human cells. Imbalance in fission and fusion of mitochondria occurs primarily owing to mutations in the proteins that execute these processes. The list of diseases that occur due to such an imbalance includes neurodegenerative diseases like Parkinson's (Schapira, 2008), Alzheimer's (Wang et al., 2009) and Huntington's diseases (Mattson, Gleichmann, & Cheng, 2008; Seong et al., 2005). Muscle atrophy and cardiovascular disorders are also known to occur upon mitochondrial dynamics dysfunction (Ashrafian et al., 2010; Romanello et al., 2010). In addition, optical atrophy and Charcot-Marie-Tooth syndrome can arise from mitochondrial dynamics imbalance (Davies et al., 2007; Züchner et al., 2004). The involvement of mitochondrial dynamics in human disease conditions makes it imperative to study the protein-based machinery that controls it.

1.3 Proteins of the Mitochondrial Membrane Fission Machinery

Mitochondria always come from preexisting cells. The progeny cells have to inherit at least one copy of the mitochondria from the parent cell for them to survive

(Boldogh, Fehrenbacher, Yang, & Pon, 2005). The cell has evolved a highly-regulated protein-based machinery for mitochondrial fission to tightly control the time and context of the division process.

In the early 1990's, genetic screens in the budding yeast *Saccharomyces cerevisiae* were used to identify proteins that are required for changes in mitochondrial morphology and distribution (Okamoto & Shaw, 2005). Subsequent studies revealed that fusion and fission are in fact two processes that exist in an equilibrium and work together to maintain mitochondrial morphology (Bleazard et al., 1999; Sesaki & Jensen, 1999). Significantly, the proteins maintaining mitochondrial fission and fusion are mostly conserved from yeast to human cells, suggesting that these processes are fundamental to eukaryotic life. Unregulated fission leads to hyper-fragmented mitochondria that exhibit loss of mitochondrial genome and defects in respiration. Conversely, unregulated fusion, hinders faithful distribution of mitochondria to daughter cells (Gorsich & Shaw, 2004).

The identification of the mitochondrial fission machinery in yeast revealed the requirement of a soluble protein of the large GTPase family- Dnm1 (Otsuga et al., 1998). Since Dnm1 cannot bind membranes by itself, it needs receptor proteins to recruit it to the mitochondrion. In yeast these receptors are Fis1 (Mitochondrial Fission 1) and Mdv1 (Mitochondrial Division Protein 1). Fis1 is a membrane-anchored protein that interacts with a soluble dimer of Mdv1 (Mozdy, McCaffery, & Shaw, 2000; Tieu & Nunnari, 2000). Mdv1 directly interacts with Dnm1 to form a ternary complex of the three proteins on the mitochondrial membrane. Mdv1 has a nonessential paralog in yeast cells- Caf4, which may function in the same fashion as Mdv1 (Griffin, Graumann, & Chan, 2005). While it is understood that mitochondrial fission occurs at sites that have assemblies of

both Mdv1 and Dnm1, the details of the mechanism of fission remain unclear (Cerveny & Jensen, 2003; Cerveny, McCaffery, & Jensen, 2001).

In mammalian cells, the function of Dnm1 is attributed to the homologous protein Dynamin-Related Protein 1 (Drp1). Fis1 also exists in mammalian systems, however its function is not understood. Homologs of Mdv1 and Caf4 are not found in mammalian cells. Instead, two classes of receptors have evolved to recruit Drp1 to mitochondrial membranes directly. One of these receptors, called the Mitochondrial Fission Factor (Mff) is conserved in metazoan organisms, but is absent from yeast (Gandre-Babbe & Bliek, 2008). The other set of receptors, the paralogs MiD49 and MiD51 (mitochondrial dynamics protein of 49kDa/51kDa) are found exclusively in vertebrates (Palmer et al., 2011). Mff does not show an apparent domain or sequence similarity to the MiD49/51 proteins. The membrane anchor position is also different for both the receptor classes, N-terminal in MiD49/51 versus C-terminal in Mff (Figure 1.2). The following sections describe briefly what is known about the mechanics of mitochondrial division, followed by an in-depth look at the known structural properties of the proteins described in this thesis.

1.4 Mitochondrial Division Is a Stepwise Process

Dynamin family proteins catalyze the fission of both mitochondria and endocytic vesicles, but the scale of constriction differs widely among the two processes. The width of endocytic necks are in the range of 20-30 nm whereas the mitochondria can be hundreds of nanometers wide (Frey & Mannella, 2000; Morlot & Roux, 2013). This difference in the width of the membrane necks being severed by the same machinery has

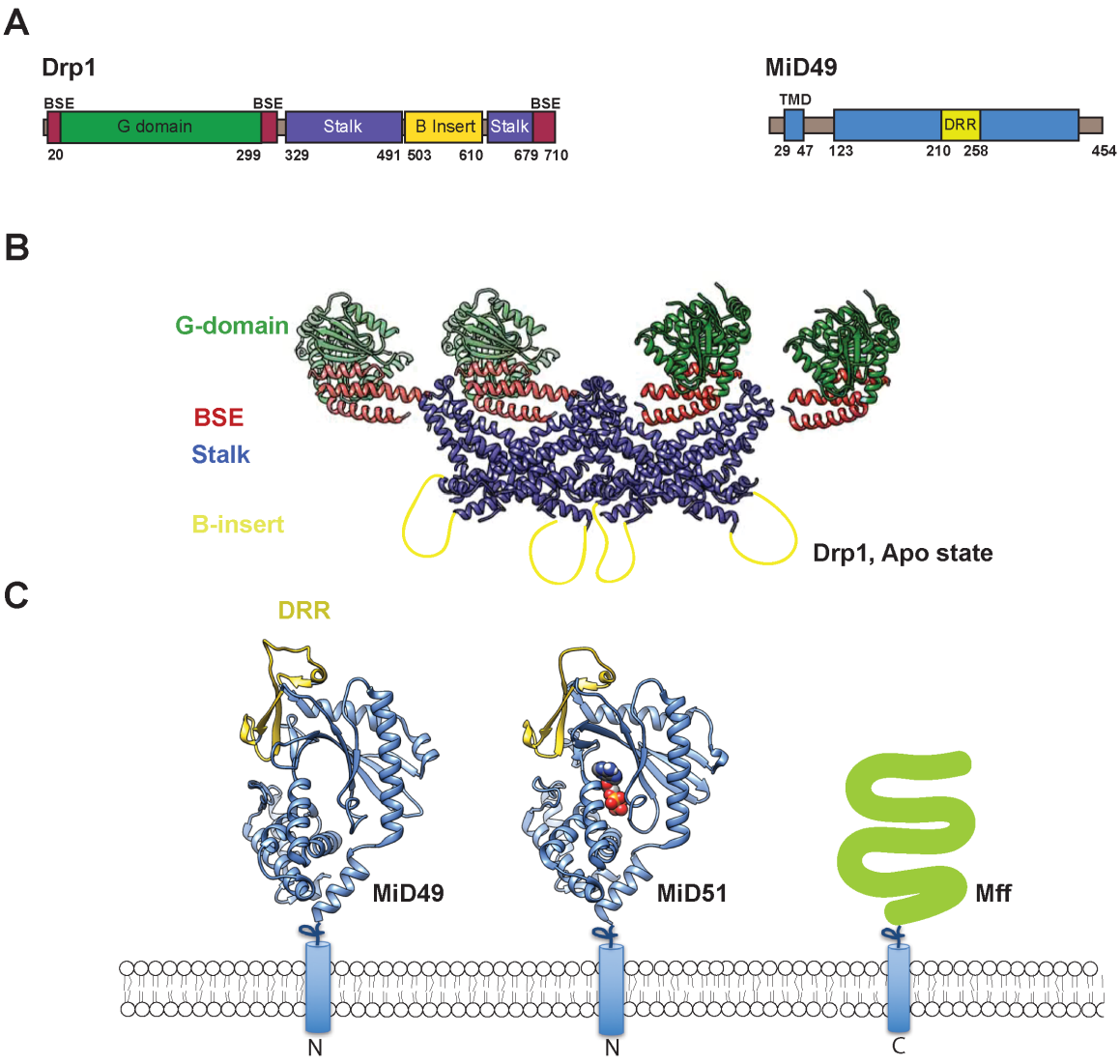

Figure 1.2: Drp1 and its Receptor Proteins. A) A schematic representation of the domain structure of Drp1 and MiD49. **B)** Crystal structure of Drp1, adapted from Frohlich et al., 2013. The PDB was adjusted to represent a tetramer, PDB ID: 4BEJ. **C)** Cartoon representation of the crystal structures of MiD49 (PDB ID 4WOY) and MiD51 (PDB ID 4NXT), and a cartoon representation of Mff on the outer mitochondrial membrane. The N- or the C-termini are indicated.

led to interesting adaptations in the mitochondrial fission mechanism. Mitochondrial division is an elaborate, stepwise process and the steps upstream of the final fission process are only beginning to be understood.

It is established that the endoplasmic reticulum (ER) and mitochondria make multiple contacts and these inter-organelle interactions are important for processes such as calcium homeostasis and lipid biosynthesis (de Brito & Scorrano, 2014; Vance & Tasseva, 2013). A protein complex called ERMES (ER Mitochondria Encounter Structure) mediates the interaction between the ER and mitochondria in yeast (Kornmann et al., 2009). Additional studies have established that ER-mitochondrial contact sites often mark the location of mitochondrial division (Friedman et al., 2011; Murley et al., 2013) and that the ER wraps around the mitochondria at future division sites (Friedman et al., 2011). This step is thought to preconstrict the mitochondria and reduce their diameter to a level where protein-based machinery can be recruited to carry out the final fission steps (Figure 1.3). Since the dynamin-based fission machinery may only act on tubules that are considerably thinner than steady-state mitochondria, the preconstriction process adds an important early step to mitochondrial fission.

Drp1 is known to localize to areas of ER-mediated mitochondrial constriction and live cell imaging has revealed a high degree of correlation between these sites and mitochondrial fission (Friedman et al., 2011; Murley et al., 2013). Mammalian cells do not have a functional homolog of the ERMES protein complex. Instead, motor proteins actin and myosin have been implicated in mediating ER-mitochondrial contact sites during mitochondrial division. Inverted formin 2 (INF2) is a protein that localizes to the ER. Its depletion is associated with elongated mitochondria and Charcot-Marie-Tooth

Figure 1.3: Steps in Mitochondrial Division: A) A steady-state mitochondrion about to divide. **B)** ER (in green) encircles the mitochondrion and provides a preconstriction. **C)** The Drp1 and receptor complex constricts the mitochondrion for fission. **D)** Fission is completed.

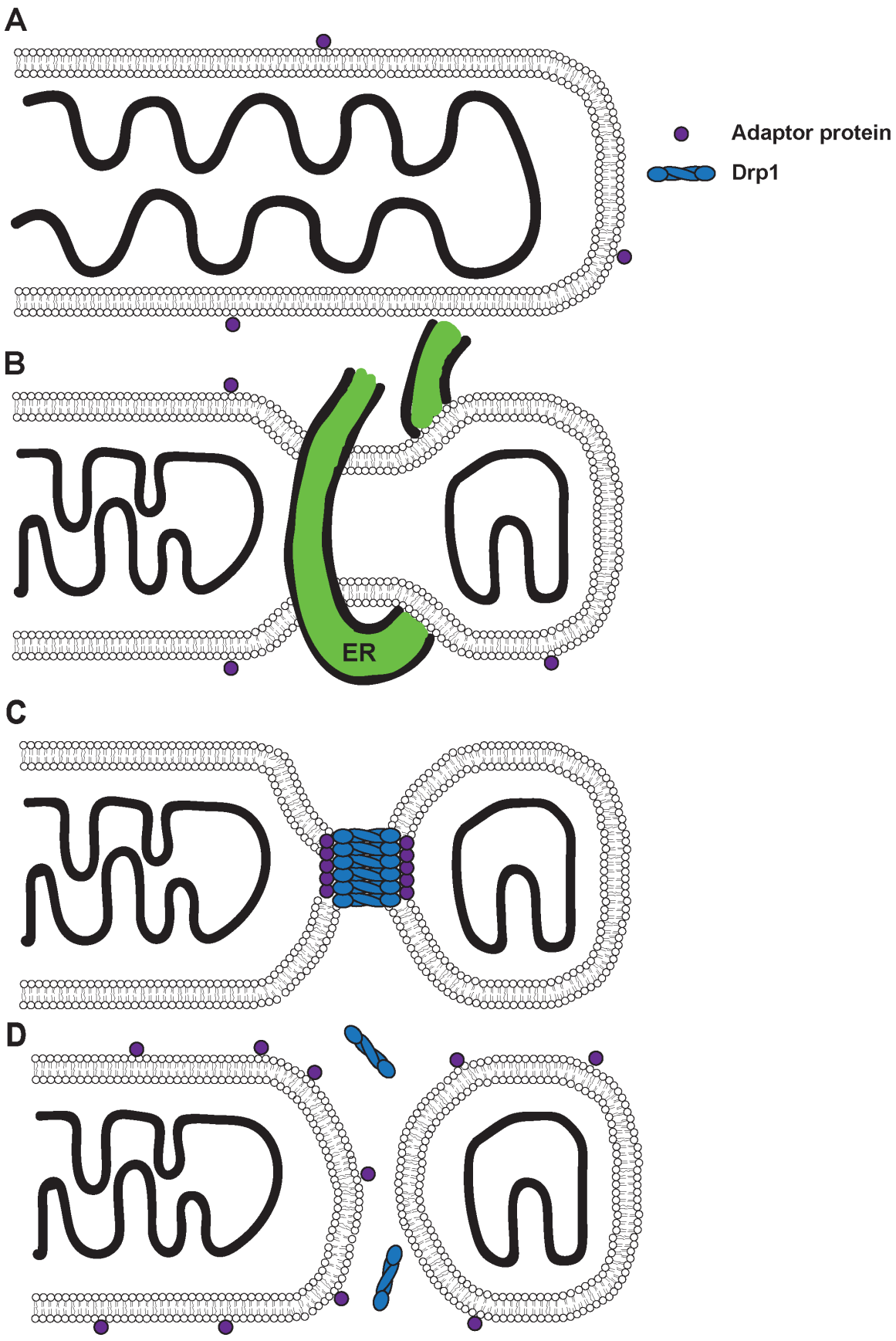
A
B
C
D
ER
Adaptor protein
Drp1

disease, a condition caused by mitochondrial division and fusion imbalance. INF2 mediates actin polymerization at ER-mitochondrial contact sites and stabilizes Drp1 oligomers (Ji et al., 2015; Korobova et al., 2013). Downstream of actin polymerization, myosin-II localizes at the ER-mitochondrial contact sites in an actin-dependent manner and its depletion reduces the amount of Drp1 on mitochondrial fission sites, resulting in decreased levels of mitochondrial division (Farida et al., 2014). This has led to a hypothesis where the "pulling" of the actin filaments by myosin-II contributes to the preconstriction step that leads to Drp1 assembly and fission of mitochondria.

The work in this dissertation deals with the steps downstream of the activity of actin and myosin. For the purposes of the experiments described in this thesis, the next sections focus on the structural and functional details of the dynamin superfamily and the receptors of the mitochondrial fission dynamin.

1.5 Structure and Function of Drp1 and the Dynamin Family Proteins

Drp1 displays multiple similarities with dynamin-1, the mechanistically better understood member of the dynamin family of proteins. Dynamin-1 severs the membranous necks of clathrin-coated vesicles during endocytosis. Most of what is known about dynamin function comes from the studies of the endocytic process in yeast (Morlot & Roux, 2013). Drp1 and endocytic dynamins have an N-terminal GTPase domain (G-domain) that binds and hydrolyzes guanosine triphosphate (GTP). The energy released as a result of this hydrolysis is thought to drive the constriction and fission activity of the dynamins (Roux, Uyhazi, Frost, & De Camilli, 2006). Following the G-domain is the 3-helix containing Bundle Signaling Element (BSE). The BSE consists of short helical

segments that are far apart in the primary sequence of the protein. Following the BSE is a four-helix bundle called the stalk. This region also mediates dynamin dimerization and higher order oligomerization. (Faelber et al., 2011; Ford, Jenni, & Nunnari, 2011; Reubold et al., 2015).

There are interesting differences in the structure of endocytic dynamins and Drp1. The C-terminal region of endocytic dynamins consists of a proline-rich domain (PRD). This domain interacts directly with the SH3 domains of endophilin molecules. The PRD is absent in Drp1. The four-helix stalk region contains insertions in the case of the endocytic dynamin and well as Drp1. In the case of the endocytic dynamins, this insertion is called the pleckstrin homology (PH) domain. This domain binds the plasma membrane lipid $PI(4,5)P_2$ (Ferguson & De Camilli, 2012). A PH domain is not present in Drp1 and is replaced by a 100-residue region called the B-insert, that has been shown to interact weakly with membranes. Interestingly, this region is also the site of most of the post-translational modifications known for Drp1 (Bui & Shaw, 2013).

How do dynamins act as fission machines? Two properties of dynamins are critical for membrane severing activity. First, these proteins bind and hydrolyze GTP, presumably providing the energy for membrane fission (Roux et al., 2006). Second, these proteins can self-assemble into spirals and rings on membranes, thereby tubulating and constricting them. This constriction is thought to cause the inner leaflets of two opposing membranes to undergo the process of hemi-fusion, leading to lipid mixing and finally coalescing of the opposing membranes (Pucadyil & Schmid, 2008; Roux & Antonny, 2008). Structural studies have pointed towards mechanisms where dynamin G-domains from the adjacent rungs of a dynamin spiral interact, leading to assembly-stimulated

hydrolysis which ultimately leads to constriction and fission of membranes (Chappie et al., 2010; Chappie & Dyda, 2013; Chappie et al., 2011).

The conformation of the dynamin molecule with and without GTP bound has been the focus of intense study. The differences in the conformation of the molecule in the two states could suggest how nucleotide binding favors membrane constriction and fission activities of dynamin. Crystallographic studies of minimal segments of the dynamin proteins have demonstrated "hinge movements" within the molecule (between the G-domain and BSE) that result as a consequence of nucleotide binding (Chappie et al., 2011, 2010). Collectively, all the hinge movements (between G-BSE and BSE-stalk) within the dynamin molecule may give rise to a conformation that is favorable for (or results from) nucleotide hydrolysis, leading to membrane fission. Such movements have not been observed in the context of full-length dynamin proteins owing to a lack of high-resolution structural information for the full-length chains in the nucleotide bound state. In this dissertation, I present a structure of full-length Drp1 bound to a nonhydrolysable GTP analog, that catches Drp1 in a receptor- and nucleotide-bound state. This structure reveals the details of the conformational changes in Drp1 upon nucleotide binding and helps to explain how such movements enable dynamins to bind receptors and constrict membranes. In the next section, the current knowledge from the atomic-level structural studies of dynamins is described for comparison to my structures (described in later chapters).

1.6 Comparative Structural Studies of the Dynamin Superfamily Proteins

Nucleotide hydrolysis by dynamins is best understood from crystallographic studies of endocytic dynamin fragments. Dynamins have traditionally been difficult candidates for crystallography because they oligomerize, have a large size, and display complex folds (Chappie & Dyda, 2013). As a result, the constructs used in the early crystallographic studies were truncated to contain just the G-domains of rat dynamin-1 and the Dictyostelium homolog DynA (Niemann et al., 2001; Reubold et al., 2005). Longer constructs that provided more information were crystallized later, including those of human dynamin-1, dynamin-3, and the related antiviral protein MxA (Faelber et al., 2011; Ford et al., 2011; Gao et al., 2011; Reubold et al., 2015). The underlying discovery that made some of these studies possible was the identification of mutations in the stalk region, 395-IHGIR-399 to 395-AAAAA-399 (in the context of human dynamin-1), that impaired higher order oligomerization. This identification was guided by the structure of the stalk region of MxA (Gao et al., 2010). In addition to these mutations, the proline rich domain (PRD) from endocytic dynamins and the viral substrate-binding loop from MxA were removed to aid in crystal formation. Similar manipulations have been used to determine the Drp1 crystal structure (Fröhlich et al., 2013).

Both the endocytic dynamin and MxA crystal structures have revealed the complex structural organization of the dynamin superfamily. Both chain termini are present in the BSE region, which resides between the G-domain and the helical stalk (Faelber et al., 2011; Ford et al., 2011; Gao et al., 2010; Reubold et al., 2015). In dynamin-1, the PH domain is an insertion between the 3rd and 4th stalk helices and is present adjacent to the stalk region. In MxA/B proteins, the same region is replaced by

the viral binding loops. In Drp1, this region contains the B-insert (Fröhlich et al., 2013). These structures have also revealed three distinct interfaces through which the stalks interact within the dynamin tetramer. These have been named interfaces 1 through 3. Hinges that lack any apparent secondary structure form flexible connections between the G-BSE and the BSE-stalk regions. The flexibility of this region aids in the movements that occur as a result of nucleotide binding, as seen in our structures in Chapter 4. All of the above structures are in the apo-state, meaning that they do not contain a nucleotide or a binding partner (Faelber et al., 2011; Ford et al., 2011; Gao et al., 2010; Reubold et al., 2015).

Details of the nucleotide binding pocket have been revealed by the crystal structure of a minimal construct of human dynamin-1 that contains most of the residues from the G-domain and the GTPase effector domain (GED), connected by a flexible linker. This construct crystallized as a dimer in the presence of a transition state analog GDP-AlF_4^- and revealed critical information regarding the coordination of the nucleotide within the binding pocket. In addition, this structure also revealed the movement of the "G2/switch 1" loop that changes conformation upon nucleotide binding (Chappie et al., 2010).

The GMPPCP bound structure of the same construct has revealed major movements in the BSE region, owing to differences in nucleotide coordination. In this state, the BSE swings ~69° relative to its position in the GDP-AlF_4^- -bound structure. This GMPPCP-bound structure has thus provided key insights into the nucleotide-based movements within the G-BSE region (Chappie et al., 2011). This movement has only been observed in the context of this engineered, smaller variant of the dynamin molecule,

and visualization of the same movement in the context of the full-length molecule could tell us how this conformational change is useful for the membrane fission activity of dynamins.

A low resolution cryo-EM structure of dynamin-1 on liposome tubules has been determined and has suggested that a dimer interface may form between adjacent rungs of a dynamin helix, favoring a G-G interaction that leads to nucleotide hydrolysis, constriction and fission (Chappie et al., 2011). This phenomenon is often referred to as assembly-mediated hydrolysis. Although Drp1 shares 33% sequence identity with dynamin-1, it is not known whether similar mechanisms govern nucleotide binding, hydrolysis and the subsequent membrane constriction. A low-resolution structure of Drp1 on nonphysiological lipid membranes (without receptors) is also available (Mears et al., 2011). This structure was different from the known cryo-EM structure of dynamin-1 because of different helical properties. This polymer was a 2-start helix compared to a 1-start helix for dynamin-1 (Chappie et al., 2011). Consequently, there were differences in the helical rise and twist between these helical assemblies. The authors also demonstrated constriction of Drp1-decorated lipid tubules upon addition of GTP. However, Drp1 also has the added complexity that it assembles on membranes only when recruited by the receptor proteins. To understand conformational changes and the effects of nucleotide binding and hydrolysis for Drp1, the context of the receptors is important. In addition, these structures that appear in the "pre-revolution" age of cryo-EM also suffer from inaccurate assignment of low resolution densities with atomic models. It is important to revisit these assemblies in the light of recent advancements in cryo-EM that have enabled considerably higher resolution data to be collected and analyzed.

1.7 Structure and Function of Drp1 Receptors

The mitochondrial fission dynamin receptor systems are very different in yeast versus mammalian cells. A summary of the basic structural details of each system is presented here.

1.7.1 Yeast receptors. Pioneering work in the structural and functional analyses of yeast receptors has revealed key insights about their roles in mitochondrial fission. It was determined that Mdv1 co-localized with Dnm1 and this interaction was important for mitochondrial fission (Cerveny et al., 2001; Tieu & Nunnari, 2000). Later, a study reported that Mdv1 interacts preferentially with assembled Dnm1 and that Mdv1 assemblies colocalized with Dnm1 assemblies at later time points in the division lifetime (Naylor et al., 2006). This study also reported that Mdv1 stays with Dnm1 until the completion of the fission process, suggesting that Mdv1 coassembles with Dnm1. The amino-terminal extension (NTE) of Mdv1 binds Fis1 and the β-propeller domain interacts with Dnm1 (Tieu et al., 2002). In this fashion, Mdv1 acts as a bridge between Dnm1 and Fis1.

Structural analyses have revealed the details of interaction between the yeast receptors and Dnm1. The TPR (tetratricopeptide repeat) domain of Fis1 interacts with a helix-loop-helix motif on Mdv1. In addition, more sites of interaction exist between the coiled coil domain of Mdv1 and the tip of the cytoplasmic domain of Fis1. The resulting complex has two molecules each of Fis1 and Mdv1 which in turn results in the presentation of two β-propeller domains of Mdv1 for the recruitment of a Dnm1 dimer (Koirala et al., 2010; Suzuki, Neutzner, Tjandra, & Youle, 2005; Tieu & Nunnari, 2000; Tieu et al., 2002; Zhang & Chan, 2007; Zhang, Chan, Ngo, Gristick, & Chan, 2012).

Mdv1 dimerizes via a coiled-coil motif and the sequence and length of the coiled coil are critical for the formation of the ternary complex of Fis1-Mdv1-Dnm1 (Koirala et al., 2010). Moreover, Mdv1 interacts with a GTP-bound form of Dnm1 and also stimulates the GTPase activity of Dnm1 in vitro (Lackner et al., 2009). The structural details of Dnm1 bound to the Fis1-Mdv1 complex are unknown.

1.7.2 Mammalian receptors. In the mammalian system, Fis1 has little or no role in mitochondrial fission (Lee et al., 2004; Otera et al., 2010). The receptors Mff, MiD49 and MiD51 are membrane anchored and interact directly with Drp1 to facilitate its recruitment to the mitochondria (Gandre-Babbe & Bliek, 2008; Otera et al., 2010; Palmer et al., 2011). The structure of Mff is unknown. Its depletion by knockdown in cultured cells produces elongated mitochondria, a phenotype similar to that of Drp1. Mff knockouts in mice are not embryonic lethal, whereas those of Drp1 are. This suggested that additional receptors can take over the role of Drp1 recruitment and cause Drp1-based fission (Chen et al., 2015). The B-insert region of Drp1 precludes interaction with Mff. Consequently, this region had to be excluded from constructs used in assembly studies with MFF (Clinton et al., 2015). In these studies, Drp1 lacking the B-insert assembles into polymers when incubated with the soluble domain of MFF. MFF also slightly enhanced the GTPase activity of Drp1 lacking the B-insert (Clinton et al., 2015). Other studies have reported that Mff recruits an oligomeric form of Drp1 (Liu & Chan, 2015). In these studies, assembly defective Drp1 mutants were also defective for Mff binding as seen by yeast two-hybrid, GST pulldown, and size exclusion chromatography experiments.

The knockdown of MiD proteins in cultured cells also results in elongated

mitochondria. Curiously, MiD overexpression also leads to the same phenotype despite Drp1 recruitment (Palmer et al., 2011; Zhao et al., 2011). Crystal structures of the soluble domains of MiD49/51 have revealed an enzymatically non-functional nucleotidyltransferase-like domain (Losón et al., 2014, 2015; Richter et al., 2014). In the case of MiD51 (not MiD49), an ADP molecule was bound to the nucleotide binding pocket. Moreover, the authors in these studies identified a region on the MiD molecules, called the Dynamin recruitment region (DRR, Figure 1.2C) that was necessary for recruiting Drp1 to the mitochondria. How the MiD proteins target Drp1 to the mitochondria was a major question that is answered in this dissertation.

Simultaneous knockdown of Mff and MiD proteins leads to a more pronounced mitochondrial division defect than either protein alone (Losón, Song, Chen, & Chan, 2013; Otera, Miyata, Kuge, & Mihara, 2016). This suggests a distribution of the fission load between the receptors with a more pronounced affect observed when no receptor is present. Due to a lack of structural knowledge of the Drp1-receptor complexes, it is not known whether the mechanism of Drp1 recruitment differs within the receptors. Studies in Chapter 3 of this dissertation establish redundant roles for mitochondrial receptors. Studies in Chapter 4 describe the mechanism by which the MiD receptors recruit and activate Drp1 for mitochondrial fission.

1.8 Thesis Layout

In the second chapter of this thesis, I describe the methodology behind the expression, purification, and in vitro assembly of the proteins of the dynamin superfamily, including dynamin -1 and Drp1, with their adaptors and receptors. Also in

the second chapter, I introduce the reader to cryogenic electron microscopy, the method utilized in Chapter 4. In the third chapter, I describe collaborative work with scientists in the biochemistry department at the University of Utah, where using fluorescence microscopy and yeast genetics, we established that any single receptor is enough to localize Drp1 to the mitochondrial membrane and cause fission. In addition, I carried out the experiments that showed for the first time that addition of a receptor can change the polymeric properties of a fission dynamin. In Chapter 4, I extend this observation from a structural standpoint, and describe how we used cryogenic electron microscopy to determine the first structures of Drp1 in complex with its receptor protein MiD49, illuminating new principles of nucleotide binding, allostery and conformational changes within these proteins. A discussion follows in the fifth chapter that summarizes the information in this thesis. In that chapter, I also discuss how the posttranslational modifications of Drp1 may affect its function, when analyzed via the lens of our new structures.

1.9 References

Andersson, G. E., Karlberg, O., Canback, B., & Kurland, C. G. (2003). On the origin of mitochondria: A genomics perspective. *Philosophical Transactions of the Royal Society B: Biological Sciences*, *358*(1429), 165–179. https://doi.org/10.1098/rstb.2002.1193

Ashrafian, H., Docherty, L., Leo, V., Towlson, C., Neilan, M., Steeples, V., … Dear, T. N. (2010). A mutation in the mitochondrial fission gene Dnm1l leads to cardiomyopathy. *PLoS Genetics*, *6*(6), 1–18. https://doi.org/10.1371/journal.pgen.1001000

Bereiter-Hahn, J., & Voth, M. (1994). Dynamics of mitochondria in living cells: Shape changes, dislocations, fusion, and fission of mitochondria. *Microscopy Research and Technique*, *27*, 198–219. https://doi.org/10.1002/jemt.1070270303

Bleazard, W., McCaffery, J. M., King, E. J., Bale, S., Mozdy, A., Tieu, Q., … Shaw, J. M. (1999). The dynamin-related GTPase Dnm1 regulates mitochondrial fission in yeast. *Nature Cell Biology*, *1*(5), 298–304. https://doi.org/10.1038/13014

Boldogh, I. R., Fehrenbacher, K. L., Yang, H. C., & Pon, L. A. (2005). Mitochondrial movement and inheritance in budding yeast. *Gene*, *354*, 28–36. https://doi.org/10.1016/j.gene.2005.03.049

Boldogh, I. R., Yang, H. C., & Pon, L. A. (2001). Mitochondrial inheritance in budding yeast. *Traffic*, *2*(6), 368–374. https://doi.org/10.1034/j.1600-0854.2001.002006368.x

Bui, H. T., & Shaw, J. M. (2013). Dynamin assembly strategies and adaptor proteins in mitochondrial fission. *Current Biology*, *23*, 891–899.

Cerveny, K. L., & Jensen, R. E. (2003). The WD-repeats of Net2p interact with Dnm1p and Fis1p to regulate division of mitochondria. *Molecular Biology of the Cell*, *14*, 4126–4139. https://doi.org/10.1091/mbc.E03

Cerveny, K. L., McCaffery, J. M., & Jensen, R. E. (2001). Division of mitochondria requires a novel DMN1-interacting protein, Net2p. *Molecular Biology of the Cell*, *12*(2), 309–21. https://doi.org/10.1091/mbc.12.2.309

Chappie, J. S., Acharya, S., Leonard, M., Schmid, S. L., & Dyda, F. (2010). G domain dimerization controls dynamin's assembly-stimulated GTPase activity. *Nature*, *465*(7297), 435–440. https://doi.org/10.1038/nature09032

Chappie, J. S., & Dyda, F. (2013). Building a fission machine--structural insights into dynamin assembly and activation. *Journal of Cell Science*, *126*(Pt 13), 2773–84. https://doi.org/10.1242/jcs.108845

Chappie, J. S., Mears, J. A., Fang, S., Leonard, M., Schmid, S. L., Milligan, R. A., … Dyda, F. (2011). A pseudoatomic model of the dynamin polymer identifies a hydrolysis-dependent powerstroke. *Cell*, *147*(1), 209–22. https://doi.org/10.1016/j.cell.2011.09.003

Chen, H., Detmer, S. A., Ewald, A. J., Griffin, E. E., Fraser, S. E., & Chan, D. C. (2003). Mitofusins Mfn1 and Mfn2 coordinately regulate mitochondrial fusion and are essential for embryonic development. *Journal of Cell Biology*, *160*(2), 189–200. https://doi.org/10.1083/jcb.200211046

Chen, H., Ren, S., Clish, C., Jain, M., Mootha, V., McCaffery, J. M., & Chan, D. C. (2015). Titration of mitochondrial fusion rescues Mff-deficient cardiomyopathy. *Journal of Cell Biology*, *211*(4), 795–805. https://doi.org/10.1083/jcb.201507035

Clinton, R. W., Francy, C. A., Ramachandran, R., Qi, X., & Mears, J. A. (2015). Dynamin-Related Protein 1 oligomerization in solution impairs functional

interactions with membrane-anchored mitochondrial fission factor. *Journal of Biological Chemistry*, *291*(1), 478–92. https://doi.org/10.1074/jbc.M115.680025

Davies, V. J., Hollins, A. J., Piechota, M. J., Yip, W., Davies, J. R., White, K. E., … Votruba, M. (2007). Opa1 deficiency in a mouse model of autosomal dominant optic atrophy impairs mitochondrial morphology, optic nerve structure and visual function. *Human Molecular Genetics*, *16*(11), 1307–1318. https://doi.org/10.1093/hmg/ddm079

de Brito, O. M., & Scorrano, L. (2014). Mitofusin 2 tethers endoplasmic reticulum to mitochondria. *Nature*, *513*(7517), 266–266. https://doi.org/10.1038/nature13550

Denton, R. M. (2009). Regulation of mitochondrial dehydrogenases by calcium ions. *Biochimica et Biophysica Acta - Bioenergetics*, *1787*(11), 1309–1316. https://doi.org/10.1016/j.bbabio.2009.01.005

Denton, R. M., McCormack, J. G., & Edgell, N. J. (1980). Role of calcium ions in the regulation of intramitochondrial metabolism. Effects of Na^{+}, Mg^{2+} and ruthenium red on the Ca^{2+}-stimulated oxidation of oxoglutarate and on pyruvate dehydrogenase activity in intact rat heart mitochondria. *The Biochemical Journal*, *190*(1), 107–117.

Estaquier, J., & Arnoult, D. (2007). Inhibiting Drp1-mediated mitochondrial fission selectively prevents the release of cytochrome c during apoptosis. *Cell Death and Differentiation*, *14*(6), 1086–1094. https://doi.org/10.1038/sj.cdd.4402107

Faelber, K., Posor, Y., Gao, S., Held, M., Roske, Y., Schulze, D., … Daumke, O. (2011). Crystal structure of nucleotide-free dynamin. *Nature*, *477*(7366), 556–60. https://doi.org/10.1038/nature10369

Ferguson, S. M., & De Camilli, P. (2012). Dynamin, a membrane-remodelling GTPase. *Nature Reviews. Molecular Cell Biology*, *13*(2), 75–88. https://doi.org/10.1038/nrm3266

Flippo, K. H., & Strack, S. (2017). Mitochondrial dynamics in neuronal injury, development and plasticity. *Journal of Cell Science*, *130*(4), 671–681. https://doi.org/10.1242/jcs.171017

Ford, M. G. J., Jenni, S., & Nunnari, J. (2011). The crystal structure of dynamin. *Nature*, *477*(7366), 561–6. https://doi.org/10.1038/nature10441

Frey, T. G., & Mannella, C. A. (2000). The internal structure of mitochondria. *Trends in Biochemical Sciences*, *4*(July), 319-324. Retrieved from papers2://publication/uuid/07A16125-F493-43E7-8CEE-EF344B83E701

Friedman, J. R., Lackner, L. L., West, M., DiBenedetto, J. R., Nunnari, J., & Voeltz, G. K. (2011). ER tubules mark sites of mitochondrial division. *Science*, *334*(6054),

358–362. https://doi.org/10.1126/science.1207385

Fröhlich, C., Grabiger, S., Schwefel, D., Faelber, K., Rosenbaum, E., Mears, J., … Daumke, O. (2013). Structural insights into oligomerization and mitochondrial remodelling of dynamin 1-like protein. *The EMBO Journal*, *32*(9), 1280–1292. https://doi.org/10.1038/emboj.2013.74

Gandre-Babbe, S., & van der Bliek, A. M. (2008). The novel tail-anchored membrane protein Mff controls mitochondrial and peroxisomal fission in mammalian cells. *Molecular Biology of the Cell*, *19*(June), 2402–2412. https://doi.org/10.1091/mbc.E07

Gao, S., Von der Malsburg, A., Dick, A., Faelber, K., Schröder, G. F., Haller, O., … Daumke, O. (2011). Structure of myxovirus resistance protein A reveals intra- and intermolecular domain interactions required for the antiviral function. *Immunity*, *35*(4), 514–525. https://doi.org/10.1016/j.immuni.2011.07.012

Gao, S., von der Malsburg, A., Paeschke, S., Behlke, J., Haller, O., Kochs, G., & Daumke, O. (2010). Structural basis of oligomerization in the stalk region of dynamin-like MxA. *Nature*, *465*(7297), 502–506. https://doi.org/10.1038/nature08972

Gorsich, S. W., & Shaw, J. M. (2004). Importance of mitochondrial dynamics during meiosis and sporulation. *Molecular Biology of the Cell*, *15*(October), 4569–4381. https://doi.org/10.1091/mbc.E03

Gray, M. W. (2012). Mitochondrial evolution. *Cold Spring Harbor Perspectives in Biology*, *4*(9). https://doi.org/10.1101/cshperspect.a011403

Griffin, E. E., Graumann, J., & Chan, D. C. (2005). The WD40 protein Caf4p is a component of the mitochondrial fission machinery and recruits Dnm1p to mitochondria. *The Journal of Cell Biology*, *170*(2), 237–48. https://doi.org/10.1083/jcb.200503148

Henze, K., & Martin, W. (2003). Evolutionary biology: Essence of mitochondria. *Nature*, *426*(6963), 127–128. https://doi.org/10.1038/426127a

Ji, W., Hatch, A. L., Merrill, R. A., Strack, S., & Higgs, H. N. (2015). Actin filaments target the oligomeric maturation of the dynamic GTPase Drp1 to mitochondrial fission sites. *eLife*, *1*(November), 1689–1699. https://doi.org/10.1017/CBO9781107415324.004

Koirala, S., Bui, H. T., Schubert, H. L., Eckert, D. M., Hill, C. P., Kay, M. S., & Shaw, J. M. (2010). Molecular architecture of a dynamin adaptor: Implications for assembly of mitochondrial fission complexes. *The Journal of Cell Biology*, *191*(6), 1127–39. https://doi.org/10.1083/jcb.201005046

Kornmann, B., Currie, E., Collins, S. R., Schuldiner, M., Nunnari, J., Weissman, J. S., & Walter, P. (2009). An ER-mitochondria tethering complex revealed by a synthetic biology screen. *Science*, *325*(5939), 477–481. https://doi.org/10.1126/science.1175088

Korobova, F., Gauvin, T. J., & Higgs, H. N. (2014). A role for myosin II in mammalian mitochondrial fission. *Current Biology*, *24*(4), 409–14. https://doi.org/10.1016/j.cub.2013.12.032

Korobova, F., Ramabhadran, V., & Higgs, H. N. (2013). An actin-dependent step in mitochondrial fission mediated by the ER-associated formin INF2. *Science*, *339*(6118), 464–467. https://doi.org/10.1126/science.1228360

Kühlbrandt, W. (2015). Structure and function of mitochondrial membrane protein complexes. *BMC Biology*, *13*(1), 89. https://doi.org/10.1186/s12915-015-0201-x

Lackner, L. L., Horner, J. S., & Nunnari, J. (2009). Mechanistic analysis of a dynamin effector. *Science (New York, N.Y.)*, *325*(5942), 874–7. https://doi.org/10.1126/science.1176921

Lee, Y., Jeong, S.-Y., Karbowski, M., Smith, C. L., & Youle, R. J. (2004). Roles of the mammalian mitochondrial fission and fusion mediators Fis1, Drp1, and Opa1 in apoptosis. *Molecular Biology of the Cell*, *15*, 5001–5011. https://doi.org/10.1091/mbc.E04

Liu, R., & Chan, D. C. (2015). The mitochondrial fission receptor Mff selectively recruits oligomerized Drp1. *Molecular Biology of the Cell*, *26*, 4466–4477. https://doi.org/10.1091/mbc.E15-08-0591

Losón, O. C., Liu, R., Rome, M. E., Meng, S., Kaiser, J. T., Shan, S.-O., & Chan, D. C. (2014). The mitochondrial fission receptor MiD51 requires ADP as a cofactor. *Structure*, *22*, 1–11. https://doi.org/10.1016/j.str.2014.01.001

Losón, O. C., Meng, S., Ngo, H., Liu, R., Kaiser, J. T., & Chan, D. C. (2015). Crystal structure and functional analysis of MiD49, a receptor for the mitochondrial fission protein Drp1. *Protein Science*, *24*(3), 386–394. https://doi.org/10.1002/pro.2629

Losón, O. C., Song, Z., Chen, H., & Chan, D. C. (2013). Fis1, Mff, MiD49, and MiD51 mediate Drp1 recruitment in mitochondrial fission. *Molecular Biology of the Cell*, *24*(5), 659–67. https://doi.org/10.1091/mbc.E12-10-0721

Mattson, M. P., Gleichmann, M., & Cheng, A. (2008). Mitochondria in neuroplasticity and neurological disorders. *Neuron*, *60*(5), 748–766. https://doi.org/10.1016/j.neuron.2008.10.010

Mayr, J. A. (2014). Lipid metabolism in mitochondrial membranes. *Journal of Inherited*

Metabolic Disease, *38*(1), 137–144. https://doi.org/10.1007/s10545-014-9748-x

Mears, J. A., Lackner, L. L., Fang, S., Ingerman, E., Nunnari, J., & Hinshaw, J. E. (2011). Conformational changes in Dnm1 support a contractile mechanism for mitochondrial fission. *Nature Structural & Molecular Biology*, *18*(1), 20–6. https://doi.org/10.1038/nsmb.1949

Morlot, S., & Roux, A. (2013). Mechanics of dynamin-mediated membrane fission. *Annual Review of Biophysics*, *42*, 629–649. https://doi.org/10.1146/annurev-biophys-050511-102247

Mozdy, A. D., McCaffery, J. M., & Shaw, J. M. (2000). Dnm1p GTPase-mediated mitochondrial fission is a multi-step process requiring the novel integral membrane component Fis1p. *Journal of Cell Biology*, *151*(2), 367–379. https://doi.org/10.1083/jcb.151.2.367

Murley, A., Lackner, L. L., Osman, C., West, M., Voeltz, G. K., Walter, P., & Nunnari, J. (2013). ER-associated mitochondrial division links the distribution of mitochondria and mitochondrial DNA in yeast. *eLife*, *2013*(2), 1–16. https://doi.org/10.7554/eLife.00422

Naylor, K., Ingerman, E., Okreglak, V., Marino, M., Hinshaw, J. E., & Nunnari, J. (2006). Mdv1 interacts with assembled dnm1 to promote mitochondrial division. *The Journal of Biological Chemistry*, *281*(4), 2177–83. https://doi.org/10.1074/jbc.M507943200

Niemann, H. H., Knetsch, M. L. W., Scherer, A., Manstein, D. J., & Kull, F. J. (2001). Crystal structure of a dynamin GTPase domain in both nucleotide-free and GDP-bound forms. *EMBO Journal*, *20*(21), 5813–5821. https://doi.org/10.1093/emboj/20.21.5813

Nunnari, J., Marshall, W. F., Straight, A., Murray, A., Sedat, J. W., & Walter, P. (1997). Mitochondrial transmission during mating in Saccharomyces cerevisiae is determined by mitochondrial fusion and fission and the intramitochondrial segregation of mitochondrial DNA. *Molecular Biology of the Cell*, *8*(7), 1233–1242. https://doi.org/10.1091/mbc.E12-03-0182

Okamoto, K., & Shaw, J. M. (2005). Mitochondrial morphology and dynamics in yeast and multicellular eukaryotes. *Annual Review of Genetics*, *39*(1), 503–536. https://doi.org/10.1146/annurev.genet.38.072902.093019

Otera, H., Miyata, N., Kuge, O., & Mihara, K. (2016). Drp1-dependent mitochondrial fission via MiD49/51 is essential for apoptotic cristae remodeling. *The Journal of Cell Biology*, jcb.201508099. https://doi.org/10.1083/jcb.201508099

Otera, H., Wang, C., Cleland, M. M., Setoguchi, K., Yokota, S., Youle, R. J., & Mihara,

K. (2010). Mff is an essential factor for mitochondrial recruitment of Drp1 during mitochondrial fission in mammalian cells. *The Journal of Cell Biology*, *191*(6), 1141–58. https://doi.org/10.1083/jcb.201007152

Otsuga, D., Keegan, B. R., Brisch, E., Thatcher, J. W., Hermann, G. J., Bleazard, W., & Shaw, J. M. (1998). The dynamin-related GTPase, Dnm1p, controls mitochondrial morphology in yeast. *Journal of Cell Biology*, *143*(2), 333–349. https://doi.org/10.1083/jcb.143.2.333

Palmer, C. S., Osellame, L. D., Laine, D., Koutsopoulos, O. S., Frazier, A. E., & Ryan, M. T. (2011). MiD49 and MiD51, new components of the mitochondrial fission machinery. *EMBO Reports*, *12*(6), 565–73. https://doi.org/10.1038/embor.2011.54

Pinton, P., Ferrari, D., Rapizzi, E., Di Virgilio, F., Pozzan, T., & Rizzuto, R. (2001). The Ca^{2+} concentration of the endoplasmic reticulum is a key determinant of ceramide-induced apoptosis: Significance for the molecular mechanism of Bcl-2 action. *EMBO Journal*, *20*(11), 2690–2701. https://doi.org/10.1093/emboj/20.11.2690

Pinton, P., Giorgi, C., Siviero, R., Zechini, E., & Rizzuto, R. (2008). Calcium and apoptosis: ER-mitochondria Ca^{2+} transfer in the control of apoptosis. *Oncogene*, *27*(50), 6407–6418. https://doi.org/10.1038/onc.2008.308.Calcium

Pucadyil, T. J., & Schmid, S. L. (2008). Real-time visualization of dynamin-catalyzed membrane fission and vesicle release. *Cell*, *135*(7), 1263–1275. https://doi.org/10.1016/j.cell.2008.11.020

Reubold, T. F., Eschenburg, S., Becker, A., Leonard, M., Schmid, S. L., Vallee, R. B., … Manstein, D. J. (2005). Crystal structure of the GTPase domain of rat dynamin 1. *Proceedings of the National Academy of Sciences of the United States of America*, *102*(37), 13093–13098. https://doi.org/10.1073/pnas.0506491102

Reubold, T. F., Faelber, K., Plattner, N., Posor, Y., Ketel, K., Curth, U., … Noe, F. (2015). Crystal structure of the dynamin tetramer. *Nature*, *525*, 404–408. https://doi.org/10.1038/nature14880

Richter, V., Palmer, C. S., Osellame, L. D., Singh, A. P., Elgass, K., Stroud, D. A., … Ryan, M. T. (2014). Structural and functional analysis of MiD51, a dynamin receptor required for mitochondrial fission. *The Journal of Cell Biology*, *204*(4), 477–486. https://doi.org/10.1083/jcb.201311014

Romanello, V., Guadagnin, E., Gomes, L., Roder, I., Sandri, C., Petersen, Y., … Sandri, M. (2010). Mitochondrial fission and remodelling contributes to muscle atrophy. *The EMBO Journal*, *29*(10), 1774–1785. https://doi.org/10.1038/emboj.2010.60

Roux, A., & Antonny, B. (2008). The long and short of membrane fission. *Cell*, *135*(7), 1163–1165. https://doi.org/10.1016/j.cell.2008.12.003

Roux, A., Uyhazi, K., Frost, A., & De Camilli, P. (2006). GTP-dependent twisting of dynamin implicates constriction and tension in membrane fission. *Nature*, *441*(7092), 528–531. https://doi.org/10.1038/nature04718

Schapira, A. H. (2008). Mitochondria in the aetiology and pathogenesis of Parkinson's disease. *The Lancet Neurology*, *7*(1), 97–109. https://doi.org/10.1016/S1474-4422(07)70327-7

Seong, I. S., Ivanova, E., Lee, J. M., Choo, Y. S., Fossale, E., Anderson, M. A., … MacDonald, M. E. (2005). HD CAG repeat implicates a dominant property of huntingtin in mitochondrial energy metabolism. *Human Molecular Genetics*, *14*(19), 2871–2880. https://doi.org/10.1093/hmg/ddi319

Sesaki, H., & Jensen, R. E. (1999). Division versus fusion: Dnm1p and Fzo1p antagonistically regulate mitochondrial shape. *The Journal of Cell Biology*, *147*(4), 699–706.

Suzuki, M., Neutzner, A., Tjandra, N., & Youle, R. J. (2005). Novel structure of the N terminus in yeast Fis1 correlates with a specialized function in mitochondrial fission. *Journal of Biological Chemistry*, *280*(22), 21444–21452. https://doi.org/10.1074/jbc.M414092200

Szabadkai, G., & Rizzuto, R. (2004). Participation of endoplasmic reticulum and mitochondrial calcium handling in apoptosis: More than just neighborhood? *FEBS Letters*, *567*(1), 111–115. https://doi.org/10.1016/j.febslet.2004.04.059

Szabadkai, G., Simoni, A. M., Chami, M., Wieckowski, M. R., Youle, R. J., & Rizzuto, R. (2004). Drp-1-dependent division of the mitochondrial network blocks intraorganellar Ca^{2+} waves and protects against Ca^{2+}-mediated apoptosis. *Molecular Cell*, *16*(1), 59–68. https://doi.org/10.1016/j.molcel.2004.09.026

Szalai, G., Krishnamurthy, R., & Hajnóczky, G. (1999). Apoptosis driven by IP3-linked mitochondrial calcium signals. *EMBO Journal*, *18*(22), 6349–6361. https://doi.org/10.1093/emboj/18.22.6349

Tieu, Q., & Nunnari, J. (2000). Mdv1p is a WD repeat protein that interacts with the dynamin-related GTPase, Dnm1p, to trigger mitochondrial division. *Journal of Cell Biology*, *151*(2), 353–365. https://doi.org/10.1083/jcb.151.2.353

Tieu, Q., Okreglak, V., Naylor, K., & Nunnari, J. (2002). The WD repeat protein, Mdv1p, functions as a molecular adaptor by interacting with Dnm1p and Fis1p during mitochondrial fission. *Journal of Cell Biology*, *158*(3), 445–452. https://doi.org/10.1083/jcb.200205031

Twig, G., Hyde, B., & Shirihai, O. S. (2008). Mitochondrial fusion, fission and autophagy as a quality control axis: The bioenergetic view. *Biochimica et*

Biophysica Acta - Bioenergetics, *1777*(9), 1092–1097. https://doi.org/10.1016/j.bbabio.2008.05.001

Vance, J. E., & Tasseva, G. (2013). Formation and function of phosphatidylserine and phosphatidylethanolamine in mammalian cells. *Biochimica et Biophysica Acta - Molecular and Cell Biology of Lipids*, *1831*(3), 543–554. https://doi.org/10.1016/j.bbalip.2012.08.016

Wang, X., Su, B., Lee, H.-G., Li, X., Perry, G., Smith, M. A., & Zhu, X. (2009). Impaired balance of mitochondrial fission and fusion in Alzheimer's disease. *Journal of Neuroscience*, *29*(28), 9090–9103. https://doi.org/10.1523/JNEUROSCI.1357-09.2009

Zhang, Y., & Chan, D. C. (2007). Structural basis for recruitment of mitochondrial fission complexes by Fis1. *Proceedings of the National Academy of Sciences*, *104*(47), 18526–18530. https://doi.org/10.1073/pnas.0706441104

Zhang, Y., Chan, N. C., Ngo, H. B., Gristick, H., & Chan, D. C. (2012). Crystal structure of mitochondrial fission complex reveals scaffolding function for Mitochondrial division 1 (Mdv1) coiled coil. *Journal of Biological Chemistry*, *287*(13), 9855–9861. https://doi.org/10.1074/jbc.M111.329359

Zhao, J., Liu, T., Jin, S., Wang, X., Qu, M., Uhlen, P., … Nister, M. (2011). Human MIEF1 recruits Drp1 to mitochondrial outer membranes and promotes mitochondrial fusion rather than fission. *The EMBO Journal*, *30*(14), 2762-2778.

Züchner, S., Mersiyanova, I. V, Muglia, M., Bissar-Tadmouri, N., Rochelle, J., Dadali, E. L., … Vance, J. M. (2004). Mutations in the mitochondrial GTPase mitofusin 2 cause Charcot-Marie-Tooth neuropathy type 2A. *Nature Genetics*, *36*(5), 449–451. https://doi.org/10.1038/ng1341

CHAPTER 2

STRUCTURAL AND FUNCTIONAL STUDIES OF MEMBRANE REMODELING MACHINES

Raghav Kalia*, Nathaniel Talledge* and Adam Frost
*- Equal Contribution

doi: 10.1016/bs.mcb.2015.02.007

CHAPTER

Structural and functional studies of membrane remodeling machines

10

Raghav Kalia[*,§,a], **Nathaniel Talledge**[*,§,a], **Adam Frost**[*,§,1]

[*]*Department of Biochemistry, University of Utah, School of Medicine, Salt Lake City, UT, USA*
[§]*Department of Biochemistry and Biophysics, University of California, San Francisco, San Francisco, CA, USA*
[1]*Corresponding author: E-mail: adam.frost@ucsf.edu*

CHAPTER OUTLINE

[a]Denotes equal contribution.

Methods in Cell Biology, Volume 128, ISSN 0091-679X, http://dx.doi.org/10.1016/bs.mcb.2015.02.007

Abstract

Building cells from their component parts will hinge upon our ability to reconstitute biochemical compartmentalization and exchange between membrane-delimited organelles. By contrast with our understanding of other cellular events, the mechanisms that govern membrane trafficking has lagged because the presence of phospholipid bilayers complicates the use of standard methods. This chapter describes in vitro methods for purifying, reconstituting, and visualizing membrane remodeling activities directly by electron cryomicroscopy.

INTRODUCTION TO MEMBRANE REMODELING

Chemical compartmentalization was as critical in the evolution of life as was the realization of self-replicating molecules. Robert Hooke's use of the metaphorical "cell" draws our attention to the inhabitants of the "small rooms" he observed with his microscope, but also to the walls that outline a room, distinguish it from its neighbors, and segregate inside from outside activities (Hooke, 1665). Boundaries—and the cells that the boundaries define—arose when amphipathic molecules formed self-sealing but semipermeable membranes to enclose chemical activities and to isolate them from dilution or admixture.

The goal expressed in this volume of *Methods in Cell Biology*, to build cells from their component parts, depends upon our understanding of biochemical compartmentalization. Specialized reactions occur more efficiently within confined, concentrated, and chemically tailored spaces, but the benefits of compartmentalization require mechanisms for sorting and transporting molecules through membranes in order to maintain raw material supplies and remove by-products. Cells also need to detect and respond to milieu variation outside their walls. The success of eukaryotic cells and multicellular cooperatives, moreover, depends upon robust mechanisms

for moving and sorting molecules between organelles and between cells. Evolutionary forces have therefore fashioned protein modules that can reversibly mold membranes into cylindrical, spherical, and saddle-shaped surfaces (Frost, Unger, & De Camilli, 2009a). It takes significant amounts of energy to shape, fuse, or fission membranes (Kozlov, McMahon, & Chernomordik, 2010; McMahon, Kozlov, & Martens, 2010). Nevertheless, cells constantly transform the sizes, shapes, and connectivity of their membranes and such remodeling underlies cell division, migration, differentiation, and communication (Frost, Unger, & De Camilli, 2009b; McMahon & Gallop, 2005). In addition, essentially every pathogen hijacks or disrupts membrane-associated protein complexes in order to infect or escape from host cells (Cossart & Roy, 2010; Laliberté & Sanfaçon, 2010; Moyer & Nemerow, 2011).

Despite such fundamental importance, we lack detailed views of the cellular machines that remodel the size, shape, or topology of cellular membranes. In comparison with other cellular processes, our understanding of the mechanisms driving membrane remodeling has lagged because the presence of phospholipid bilayers precludes the use of many standard methods in cell biology. Until very recently, for example, we have had almost no structural information about membrane-bound protein assemblies (Chappie et al., 2011; Frost et al., 2008; Low, Sachse, Amos, & Löwe, 2009; Mim et al., 2012). This chapter describes in vitro methods for purifying, reconstituting, and visualizing membrane remodeling complexes directly in their membrane-bound states.

Although many proteins are recruited from the cytosol to coat, bend, and ultimately fission membranes, one major focus of research in this field centers on large GTPases of the dynamin family (Doherty & McMahon, 2009). This chapter focuses on methods for studying dynamin-family proteins and their binding partners. Dynamin proteins assemble into helical collars around the necks of budding vesicles and channel GTP energy into mechanochemical constriction of the collar to promote fission (Ferguson & De Camilli, 2012; Morlot et al., 2012). Major unanswered questions now concern the mechanisms by which dynamin proteins are recruited to their target membranes and regulated by their binding partners (Daumke, Roux, & Haucke, 2014; Meinecke et al., 2013). All dynamin proteins engage in avid interactions with other proteins, many of which are membrane-binding or *trans*-membrane proteins themselves. Efforts in our lab are focused in part on testing the hypothesis that dynamins are recruited by binding partners that can coassemble with dynamin and thereby modulate the properties of the helical collars in order to regulate or repurpose membrane fission reactions for different contexts (Figure 1).

The majority of work on dynamin proteins is focused on endocytosis at the plasma membrane, but dynamin-family proteins also function at intracellular organelles and some evidence suggests that the latter are the more ancient activity (Figures 1 and 2) (Elde, Morgan, Winey, Sperling, & Turkewitz, 2005; Osteryoung & Nunnari, 2003; Rahaman, Elde, & Turkewitz, 2008). Chloroplasts, peroxisomes, and mitochondria are the best known sites of intracellular activity for the dynamin-like proteins, with Dnm1 (yeast) and Drp1 (humans) receiving considerable attention for their role in regulating mitochondrial morphology and metabolism

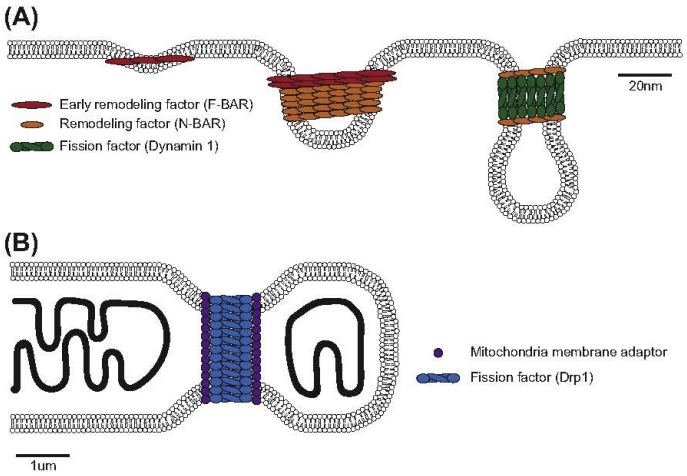

FIGURE 1 Dynamin-family GTPases drive diverse membrane remodeling events.

(A) In concert with a number of BAR-domain containing proteins, Dynamin-family GTPases shape and fission endocytic tubules from the plasma membrane. (B) Dynamin-family GTPases partner with transmembrane proteins to help shape and fission mitochondria and other intracellular organelles.

(Lackner & Nunnari, 2009). How did dynamin GTPases adapt to catalyze fission in diverse contexts and on different spatial scales—from the <50 nm necks of clathrin-coated pits to the >1 μm tubules of peroxisomes, chloroplasts, and mitochondria? Recent work indicates that the minimal machine that fragments large mitochondrial tubules comprises a dynamin and at least one transmembrane adaptor of the mitochondrial outer membrane (Koirala et al., 2013). In this chapter we describe our protocols for purifying and reconstituting the cocomplexes formed by mitochondrial outer membrane proteins MiD49/MiD51 and the dynamin-related protein Drp1 (Figures 1 and 2).

We will also describe our approach to purifying, assembling, and imaging a heteropolymer of Dynamin1 and the BAR domain-containing protein EndophilinA1 (Daumke et al., 2014). The heterocomplex of Dynamin1 and EndophilinA1 assembles around narrow endocytic tubules, but its precise function remains poorly understood. This complex was implicated recently in a fast mode of clathrin-independent endocytosis that appears to be critical in migrating cells that internalize cell-surface signaling complexes from the leading edge (Boucrot et al., 2014). Genetic studies in many organisms, however, have indicated that EndophilinA1 and Dynamin1 *null* mutants have distinctly different phenotypes and, by contrast with Dynamin1 alone,

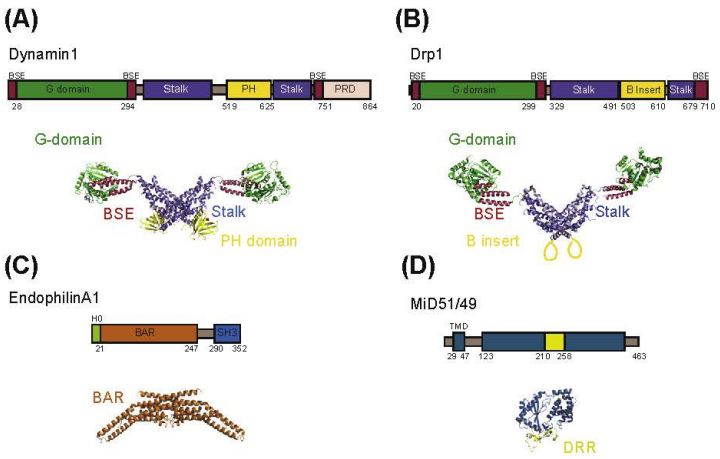

FIGURE 2 Domain architectures and X-ray crystal structures of the human proteins discussed in this chapter.

(A) Dynamin1 (PDB: 3SNH) (Faelber et al., 2011; Ford, Jenni, & Nunnari, 2011). (B) Dynamin-related protein 1 or Drp1 (PDB: 4BEJ) (Fröhlich et al., 2013). (C) EndophilinA1 (PDB: 1X03) (Gallop et al., 2006; Masuda et al., 2006). (D) Mitochondrial Dynamics protein 49/51 or MiD49/51 (PDB: 4NXT) (Losón et al., 2014; Richter et al., 2014). (See color plate)

this cocomplex cannot mediate fission in vitro as assayed by electron microscopy (Milosevic et al., 2011; Schuske et al., 2003; Verstreken et al., 2002). In this chapter we outline our approach to purifying, reconstituting, and visualizing the Dynamin1 and EndophilinA1 copolymer in its membrane-bound state (Figure 5).

The large sizes, the inherent heterogeneity of lipid mixtures, and the complexity of multicomponent protein complexes make membrane-associated machines intractable for the mature techniques of X-ray crystallography or NMR spectroscopy (Figures 4 and 5). By contrast, electron microscopy is well suited to visualizing lipid bilayers and bound protein complexes directly (Chappie et al., 2011; Frost et al., 2008; Low et al., 2009; Mim et al., 2012; Szwedziak, Wang, Bharat, Tsim, & Löwe, 2014). Recent advances in electron microscopes, direct electron detectors, and new statistical approaches to image analysis have pushed the resolution limit for electron cryomicroscopy (cryo-EM) into the near-atomic regime (Henderson, 2013; Kim et al., 2014; Liao, Cao, Julius, & Cheng, 2013; Lu et al., 2014). The application of these technologies to membrane-associated protein complexes will, in the near future, illuminate the protein–protein and protein–lipid interactions that determine membrane remodeling reactions and that enable biochemical compartmentalization or life within the walls of our little rooms.

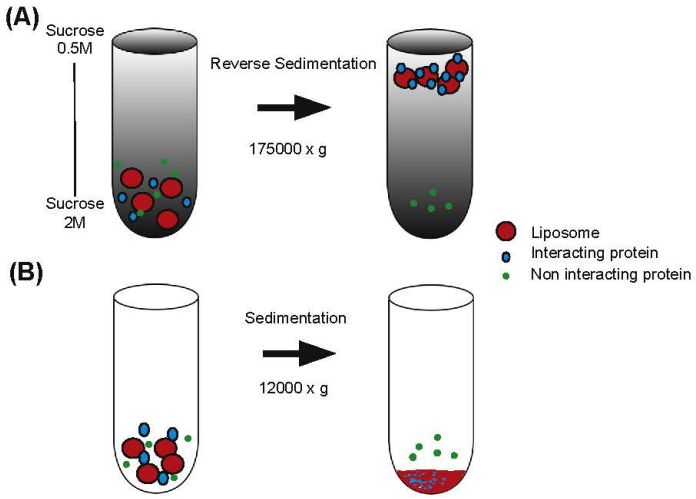

FIGURE 3 Centrifugation assays for qualitative membrane binding.

(A) Flotation or reverse sedimentation exploits the buoyancy of vesicles within a density gradient to separate bound from unbound protein and to avoid contamination with unstable protein aggregates. This assay rarely yields false-positives due to its stringency, but weak membrane interactions are typically missed. (B) In a traditional sedimentation assay vesicles are pelleted rapidly at high G-forces along with bound proteins. If the target lipid or the bulk properties of the vesicles are chosen appropriately for the protein being investigated, this assay rarely results in false-negatives. However, unstable proteins or protein oligomers may pellet nonspecifically.

1. METHODS

1.1 PURIFICATION OF PROTEINS FROM *ESCHERICHIA COLI*

1.1.1 BAR domain-containing protein overexpression in E. coli

This protocol is specifically adapted to express full-length and GST-tagged EndophilinA1 protein utilizing the pGEX6p1 expression vector (Mim et al., 2012). Alternative expression plasmids will also express other BAR domain-containing proteins. It is important to adapt this protocol to ensure that your expression vector and bacterial strain have been selected for the correct media and expression conditions.

1.1.1.1 Transforming *E. coli* cells

1.1.1.1.1 Reagents, equipment, and buffers

- Human EndophilinA1 ORF cloned in pGEX6p1 plasmid. This vector introduces an N-terminal GST tag followed by a PreScission protease recognition site (GE, 88947, Little Chalfont, UK).

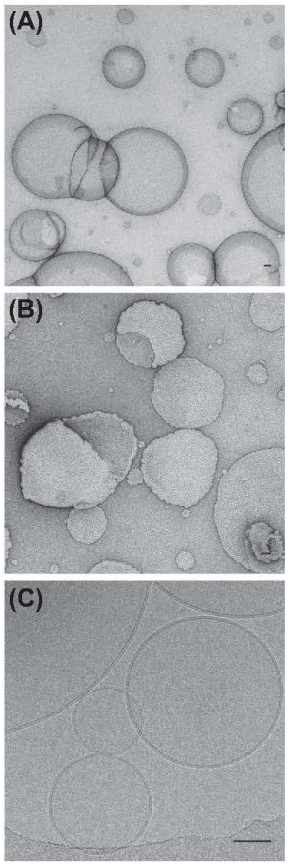

FIGURE 4 Visualizing model membranes with transmission electron microscopy.

(A) An electron micrograph of osmotically stable vesicles stained with uranyl acetate. (B) An electron micrograph of "ruffled" vesicles due to an osmotic imbalance and volume shrinking during the negative staining procedure. (C) Electron cryo-micrograph of vitrified liposomes with diverse diameters. Note the phospholipid headgroups that define the 5 nm bilayer. Bars 50 nm.

- BL21 (DE3) RIPL competent cells (Agilent Technologies, 230280, Santa Clara, CA). This strain of *E. coli* has been engineered to have an expanded set of tRNA genes that improve heterologous protein expression. Other competent bacterial strains with similar features may also work.

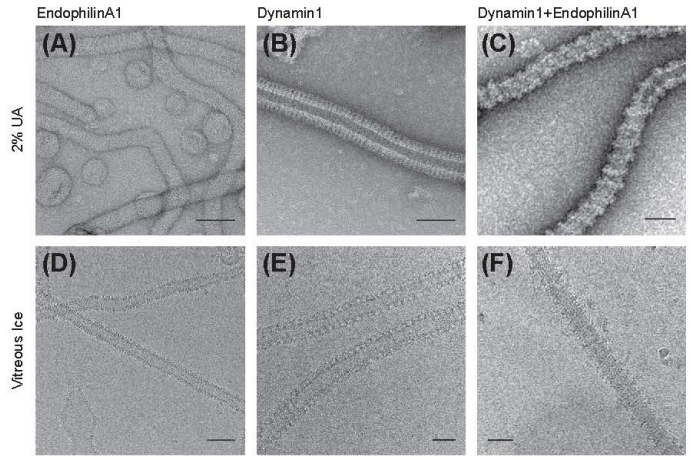

FIGURE 5 Membrane-remodeling complexes visualized with negative stain versus cryo-electron microscopy.

EndophilinA1 (A and D), Dynamin1 (B and E), or the heterocomplex formed by both proteins (C and F). In all cases, the purified proteins remodel spherical vesicles into high-curvature cylinders wrapped in an oligomeric protein coat. In the heterocomplex the adjacent turns of the Dynamin1 helix are separated by 2, 3, or 4 copies of an interleaving molecule of EndophilinA1. Bars 50 nm.

- Autoclave
- LB liquid media (Sigma–Aldrich, L2542, St Louis, MO)
- Bunsen burner
- Inoculation loop
- 10 mL culture tubes (Kimble Chase, 73500-13100, Vineland, NJ)
- Temperature-controlled water bath (42 °C) or equivalent
- Temperature-controlled shaking incubator (37 °C)
- LB agar plates with ampicillin and chloramphenicol (Teknova, L5204, Hollister, CA).

1.1.1.1.2 Detailed procedure

1. Thaw stock of BL21 competent cells on ice (50 μL aliquot).
2. Add 50–100 ng of EndophilinA1 expression plasmid to the thawed cells.
3. Incubate on ice for 30 min, with gentle mixing every 5–10 min.
4. Heat shock cells in 42 °C water bath for 45 s.
5. Place the heat-shocked cells on ice for 5 min.
6. Transfer cells to 900 μL of LB liquid media and allow cells to incubate at 37 °C with shaking at 100 rpm for 45–60 min in a 10 mL culture tube.

7. Allow LB agar plates with ampicillin (100 μg/mL) and chloramphenicol (34 μg/mL) to equilibrate to room temperature.
8. Plate 50–100 μL of the starter culture onto the LB agar selection plates using sterile technique with a Bunsen burner and an inoculation loop.
9. Use sterile glass beads or a sterile bacterial spreader to absorb the culture onto the plate.
10. Incubate plates at 37 °C until individual bacterial colonies are observed (8–16 h). Glycerol stocks stored at −80 °C can be made from cultures of individual colonies from these plates to preserve this specific expression strain of *E. coli*.

1.1.1.2 Protein overexpression

1.1.1.2.1 Reagents, equipment, and buffers

- BL21 (DE3) RIPL cells expressing EndophilinA1
- Autoclave
- Inoculation loop
- LB liquid media (Sigma–Aldrich, L2542, St Louis, MO)
- Ampicillin (Gold Biotechnology, A-301-5, St Louis, MO)
- Chloramphenicol (Gold Biotechnology, C-105-25, St Louis, MO)
- 500 mL Erlenmeyer flask (Thermo Fisher Scientific, FB-500-500, Waltham, MA)
- Temperature-controlled shaking incubator (37 °C)
- Spectrophotometer with 600 nm absorbance setting
- Cuvettes
- 2.8 L Fernbach flasks (Corning, 4424-2XL, Corning, NY)
- ZY auto-induction media (Studier et al., 2005)
  - ZY—10 g Bacto-tryptone, 5 g yeast extract, 925 mL water
  - 50X 5052—0.5% Glycerol, 0.05% Glucose, 0.2% α-Lactose
  - 20X NPS—0.5 M $(NH_4)_2SO_4$, 1 M KH_2PO_4, 1 M Na_2HPO_4
  - Trace metals mix—50 mM $FeCl_3 \cdot 6H_2O$, 20 mM $CaCl_2 \cdot 2H_2O$, 10 mM $MnCl_2 \cdot 4H_2O$, 10 mM $ZnSO_4 \cdot 7H_2O$, 2 mM $CoCl_2 \cdot 6H_2O$, 2 mM $CuCl_2 \cdot 2H_2O$, 2 mM $NiCl_2 \cdot 6H_2O$, 2 mM $Na_2MoO_4 \cdot 2H_2O$, 2 mM H_3BO_4.
  - Before use, mix per liter—928 mL ZY, 1 mL 1 M $MgSO_4$, 1 mL Trace metals mix, 20 mL 50X 5052 solution, 50 mL 20X NPS solution.
- Temperature-controlled shaking incubator (19 °C)
- Balance
- Centrifuge with Avanti JLA 8.1 rotor (Beckman Coulter, Indianapolis, IN) or equivalent
- 1 L centrifuge bottles (Beckman Coulter, 363676, Indianapolis, IN).

1.1.1.2.2 Detailed procedure

1. Prepare 100 mL of LB media with ampicillin (100 μg/mL) and chloramphenicol (34 μg/mL) in a 500 mL Erlenmeyer flask. Ensure that culture media and glassware have been autoclaved.

2. Utilize a sterile inoculation loop to pick an *E. coli* colony from the agar plate and inoculate 100 mL LB media plus antibiotics. Following proper sterile techniques during all bacterial expression steps is crucial to prevent contamination.
3. Shake the culture at 150 rpm at 37 °C overnight (8–12 h).
4. Measure culture density utilizing optical density (OD_{600}) reading in a spectrophotometer—Culture density = dilution factor * OD_{600} reading.
5. Prepare 500 mL of sterile ZY autoinduction media with 100 μg/mL ampicillin and 34 μg/mL chloramphenicol in a 2.8 L Fernbach flask.
6. Add enough starter culture to 500 mL flasks to obtain an OD_{600} of 0.05. Volume to add = (desired OD_{600} * expression culture volume)/OD_{600} reading of starter culture.
7. Shake the culture at 150 rpm at 37 °C until bacteria is in mid-log phase (OD_{600} = 0.7–0.8).
8. Shift the culture to 19 °C and shake-incubate overnight (8–20 h). We have found that the 19 °C temperature shift aids in protein stability during overexpression and leads to an increased yield of stable protein.
9. Harvest the cultures using 1 L centrifuge tubes.
10. Centrifuge the cells at 4000× g for 10 min at 4 °C in an Avanti JLA 8.1 rotor.
11. Collect the cell pellet in a disposable 50 mL centrifuge tube. Typical yields are 5–20 g of cell culture pellet per 1 L of liquid culture.
12. You may proceed immediately to the next step or freeze and store cell pellets in 50 mL disposable centrifuge tubes at −80 °C until ready for the next step.

1.1.2 BAR domain-containing protein purification and storage

1.1.2.1 Reagents, equipment, and buffers

- BL21 (DE3) RIPL EndophilinA1 cell pellet
- 250 mL Griffin stainless steel beaker (Sigma–Aldrich, Z155527, St Louis, MO)
- Aprotinin (Roche, 10236624001, Mannheim, Germany)
- Phenylmethylsulfonyl fluoride (PMSF) (Roche, 10837091001, Mannheim, Germany)
- Leupeptin (Roche, 11034626001, Mannheim, Germany)
- Pepstatin (Roche, 11524488001, Mannheim, Germany)
- DNase I (Roche, 10104159001, Mannheim, Germany)
- Lysozyme (Sigma–Aldrich, L6876, St Louis, MO)
- Branson sonifier with 0.5 inch tip (Thermo Fisher Scientific, 22309783, Waltham, MA) or equivalent
- 50 mL Oak Ridge centrifuge tubes (Thermo Fisher Scientific, 3139-0030, Waltham, MA)
- Centrifuge with Avanti JA 25.50 rotor (Beckman Coulter, Indianapolis, IN) or equivalent
- 0.45 μm syringe filter (Thermo Fisher Scientific, 190-9945, Waltham, MA)
- Glutathione sepharose 4 fast flow affinity beads (GE, 17513202, Little Chalfont, UK)

- Glass gravity columns 25 mm ID; 200 mm length (Kimble Chase Kontes, K420400-2520, Vineland, NJ)
- Vivaspin 3 kDa MWCO centrifugal concentrator (Sartorius Stedim Biotech VS2092, New York, NY)
- PreScission protease (GE, 88947, Little Chalfont, UK)
- Dialysis tubing 12–14 kDa MWCO (Thermo Fisher Scientific, 2115214, Waltham, MA)
- SDS PAGE supplies
- Bio-Rad NGC chromatography system (Bio-Rad, 788-0003, Hercules, CA) or equivalent
- HiLoad 16/600 Superdex 200 column (GE, 28989335, Little Chalfont, UK)
- Liquid nitrogen
- BAR-buffer A: 300 mM KCl, 50 mM Tris pH 7.4, 5 mM Imidazole, 1 mM DTT, 1% Triton X-100.
- BAR-buffer B: 150 mM KCl, 50 mM Tris pH 7.4, 1 mM DTT.

1.1.2.2 Detailed procedure

1. Thaw and resuspend the cell pellet in BAR-buffer A containing protease inhibitors PMSF (1 mM), pepstatin (1 μM), leupeptin (10 μM), and aprotinin (0.5 μM). Use 50 mL BAR-buffer A per 20 g cell pellet and place the homogenized mixture into a 250 mL Griffin stainless steel beaker prechilled on ice. Remainder of purification steps should be performed on ice unless otherwise noted.
2. Add 500 units of DNase I per 50 mL lysate. DNase I digests the bacterial DNA present in the lysate. The removal of cellular DNA prevents partial insolubility of the overexpressed protein by preventing entanglement of the two.
3. Add 15 mg powdered lysozyme to the lysate and incubate on ice for 30 min with gentle stirring every 5 min.
4. Sonicate the resuspended cell pellet at 90% duty cycle for 30 min with 30 s sonication and 1 min rest cycles.
5. Clear the lysate with a 20,000× g spin for 1 h at 4 °C in 50 mL oak ridge centrifuge tubes.
6. Decant the supernatant into a prechilled 250 mL beaker and filter the solution with a 0.45 μm syringe filter and a 60 mL syringe into a clean prechilled beaker.
7. Prepare an affinity column by loading 5 mL (bed volume) of glutathione sepharose bead slurry into a glass gravity column prefilled with deionized water.
8. Wash beads with ≥200 mL of deionized water.
9. Equilibrate beads with three 100 mL washes of BAR-buffer A.
10. Apply the clarified filtered lysate onto the glutathione sepharose beads and incubate at 4 °C for 4–12 h with gentle rocking.
11. Let the unbound lysate flow through the gravity column.

12. Wash unbound protein impurities with 40 bed volumes BAR-buffer A.
13. Resuspend the GST-tagged BAR protein bound to sepharose beads into 10 bed volumes of BAR-buffer B and add 20 units of PreScission protease.
14. Incubate at 4 °C for 8 h.
15. Elute the cleaved protein from the affinity column into a 50 mL centrifuge tube on ice.
16. Evaluate cleaved protein purity and molecular weight with SDS-PAGE followed by Coomassie blue staining.
17. Dialyze the protein against 2 L of BAR-buffer B using a 12–14 kDa MWCO dialysis tubing for 8–12 h.
18. Concentrate the eluate with 3 kDa MWCO centrifugal concentrators to <2 mL final volume.
19. Inject the concentrated protein solution over a HiLoad 16/600 Superdex 200 column preequilibrated with BAR-buffer B. EndophilinA1 elutes at ~85 mL.
20. Pool the peak fractions and check the concentration using a spectrophotometer. Concentrate the protein using 3 kDa MWCO centrifugal concentrators to a final concentration >5 mg/mL.
21. Aliquot into 10–50 μL aliquots (single use). This prevents exposing the purified protein to freeze–thaw cycles that cause degradation.
22. Flash freeze the protein with liquid nitrogen and store at −80 °C.

1.1.3 Soluble MiD49/51 adaptor protein truncation overexpression in E. coli

The protocol described below is for the expression and purification of MiD49 from *E. coli*. The protocol also can be used to purify MiD51. The soluble domain of MiD49 (amino acids 126–454) was used for this purification. Variations of this protocol have previously been described (Losón et al., 2014; Richter et al., 2014).

1.1.3.1 Reagents, equipment, and buffers

- Human MiD49 soluble domain (amino acids 126–454) ORF cloned in pGEX6p1 vector. This vector introduces an N-terminal GST tag followed by a PreScission protease recognition site.
- Same reagents as protocol step 1.1.1.1.1 for transformation.
- Same reagents as protocol step 1.1.1.2.1 for protein overexpression.

1.1.3.2 Detailed procedure

Same protocol as BAR domain protein overexpression in *E. coli*. Follow protocol steps 1.1.1.1.2 for transformation and protocol steps 1.1.1.2.2 for protein overexpression.

1.1.4 Soluble MiD adaptor protein truncation purification and storage

1.1.4.1 Reagents, equipment, and buffers

- All protein purification reagents and equipment as described for Section 1.1.2.1

- MiD-buffer A: 50 mM Tris pH 8.0, 500 mM NaCl, 5%glycerol, 1 mM DTT, 0.1%, Triton X-100
- MiD-buffer B: 50 mM Tris pH 8.0, 500 mM NaCl, 5% glycerol, 1 mM DTT
- MiD-buffer C: 20 mM Tris pH 8.0, 200 mM NaCl, 5% glycerol, 1 mM DTT.

1.1.4.2 Detailed procedure

1. Thaw and resuspend the cell pellet in MiD-buffer A containing protease inhibitors PMSF (1 mM), pepstatin (1 μM), leupeptin (10 μM), and aprotinin (0.5 μM). Use a volume of 50 mL per 20 g of pellet. Transfer the resuspended pellet to a 250 mL Griffin stainless steel beaker prechilled on ice. Remainder of purification steps should be performed on ice unless otherwise noted.
2. Add 500 units DNase I per 50 mL lysate.
3. Add 15 mg powdered lysozyme to the lysate and incubate the resuspended pellet on ice for 30 min with gentle stirring every 5 min.
4. Sonicate the resuspended cell pellet at 90% duty cycle for 30 min with 30 s sonication and 1 min rest cycles.
5. Spin at 20,000× g for 1 h at 4 °C in 50 mL oak ridge centrifuge tubes to separate the soluble and insoluble portions.
6. Decant the supernatant into a prechilled 250 mL beaker and filter the solution with a 0.45 μM syringe filter and a 60 mL syringe into a clean prechilled beaker.
7. Prepare an affinity column by adding 5 mL of the glutathione sepharose bead slurry into a glass gravity column prefilled with deionized water.
8. Incubate the clarified lysate from step 6 for 12 h with glutathione sepharose beads equilibrated with MiD-buffer A at 4 °C.
9. Allow the unbound protein to flow through and wash the beads with 40 times the bed volume with MiD-buffer A followed by MiD-buffer B.
10. Incubate the beads overnight with 20 units of PreScission protease at 4 °C with gentle rocking for 12 h.
11. Pass the supernatant over a gravity column and obtain the flow through. The flow through should contain the cleaved MiD49. Evaluate the molecular weight and percentage purity of the cleaved protein with SDS-PAGE followed by Coomassie blue staining.
12. Concentrate the cleaved protein using a 3 kDa MWCO centrifugal concentrator to a volume <2 mL and load on a HiLoad 16/600 Superdex 200 column preequilibrated with MiD-buffer C for size exclusion. The column volume for the Superdex 200 is 120 mL and the MiD49 peak appears at ~72 mL.
13. Evaluate protein purity and molecular weight with SDS-PAGE followed by Coomassie blue staining.
14. Collect the fractions positive for MiD49 and concentrate using a 3 kDa MWCO centrifugal concentrator. Concentration of the protein preparation can be estimated at this stage using a spectrophotometer. Concentrate the protein to ~5 mg/mL.

15. Divide into 20 μL aliquots (single use) and flash freeze using liquid nitrogen and store at −80 °C until further use.

1.1.5 Drp1 overexpression in E. coli

Full-length dynamin proteins have been challenging to purify historically, owing to their propensity to oligomerize and poor stability/solubility when overexpressed in bacteria. As a result, multiple protocols have been developed to purify dynamins from yeast and insect cell-based expression systems. This protocol describes overexpression and purification of human Drp1 from *E. coli*. The combination of specialized buffers utilized here results in highly pure, stable, and assembly-competent Drp1 protein. Variations of this protocol have been reported (Fröhlich et al., 2013; Koirala et al., 2013).

1.1.5.1 Reagents, equipment, and buffers

- Human Drp1 gene cloned in pET16b vector. This vector introduces an N-terminal 6X-histidine tag followed by a PreScission protease recognition site.
- Same reagents as protocol step 1.1.1.1.1 for transformation.
- Same reagents as protocol step 1.1.1.2.1 for protein overexpression.

1.1.5.2 Detailed procedure

Same protocol as BAR domain protein overexpression in *E. coli*. Follow protocol steps 1.1.1.1.2 for transformation and protocol steps 1.1.1.2.2 for protein overexpression.

1.1.6 Drp1 purification and storage

1.1.6.1 Reagents, equipment, and buffers

- BL21 (DE3) RIPL cells expressing human Drp1
- All protein purification reagents and equipment as described for Section 1.1.1.1.2
- Qiagen Ni-NTA Agarose beads (Qiagen 30230, Venlo, Netherlands)
- Drp1-buffer A: 50 mM HEPES/NaOH pH 7.5, 400 mM NaCl, 20 mM imidazole, 5 mM $MgCl_2$, and 1 mM DTT
- Drp1-buffer B: 50 mM HEPES/NaOH pH 7.5, 800 mM NaCl, 5 mM $MgCl_2$, 20 mM imidazole, 1 mM DTT, 1 mM ATP, 10 mM KCl
- Drp1-buffer C: 50 mM HEPES/NaOH pH 7.5, 400 mM NaCl, 20 mM imidazole, 5 mM $MgCl_2$ and 1 mM DTT, 0.5% CHAPS
- Drp1-buffer D: 50 mM HEPES/NaOH pH 7.5, 400 mM NaCl, 300 mM imidazole, 5 mM $MgCl_2$ and 1 mM DTT
- Drp1-buffer E: 20 mM HEPES/NaOH pH 7.5, 300 mM NaCl, 2.5 mM $MgCl_2$ and 1 mM DTT.

1.1.6.2 Detailed procedure

1. Thaw and resuspend the cell pellet in Drp1-buffer A containing protease inhibitors PMSF (1 mM), pepstatin (1 μM), leupeptin (10 μM), and aprotinin

(0.5 μM). Use a volume of 50 mL per 20 g of pellet. Transfer the resuspended pellet to a stainless steel beaker.
2. Add 0.5 mg DNase1 and 50 mg powdered Lysozyme. Incubate the mixture on ice for 30 min with constant stirring every 5 min.
3. Sonicate the resuspended cell pellet at 90% duty cycle for 30 min with 30 s sonication and 1 min rest cycles.
4. Spin the lysate at 20,000× g for 1 h at 4 °C to separate the soluble and insoluble portions.
5. Decant the supernatant in a prechilled 250 mL beaker and filter the solution with a 0.45 μm syringe filter and a 60 mL syringe into a clean prechilled beaker.
6. Prepare an affinity column by equilibrating 5 mL of the Qiagen nickel-NTA beads in Drp1-buffer A.
7. Incubate the beads with the clarified lysate for 1 h at 4 °C with gentle rocking.
8. Allow the unbound portion of the lysate to flow through using a gravity column.
9. Wash the beads with 40 bed volumes of Drp1-buffer A, followed by Drp1-buffer B and Drp1-buffer C (40 bed volumes each).
10. Wash with 40 bed volumes of Drp1-buffer A once more.
11. Elute the protein with 10 bed volumes of Drp1-buffer D.
12. Cleave the eluted protein overnight at 4 °C using 20 units of PreScission protease while dialyzing to Drp1-buffer A (2 L) for 12 h.
13. Rebind cleaved protein to fresh beads equilibrated with Drp1-buffer A.
14. The protein can bind to the beads despite cleavage of the His tag. After washing the beads with 40 bed volumes of Drp1-buffer A, elute with 10 bed volumes of Drp1-buffer D.
15. Concentrate the eluate using a 3 kDa MWCO centrifugal concentrator and reduce the volume to <2 mL.
16. Inject the concentrated protein over a HiLoad 16/600 Superdex 200 column preequilibrated with Drp1-buffer E for size exclusion.
17. Elute from the size exclusion column with 1 column volume of Drp1-buffer E. The column volume for the Superdex 200 is 120 mL and the Drp1 peak appears at ~60 mL.
18. Collect the fractions from the protein peak, estimate percentage purity and molecular weight using SDS-PAGE followed by Coomassie blue staining.
19. Concentrate to 9 mg/mL using a 3 kDa MWCO centrifugal concentrator. Divide into 20 μL single use aliquots. Flash freeze using liquid nitrogen and store at −80 °C.

1.2 PURIFICATION OF SH3 DOMAINS FROM *E. COLI*

This protocol is for the preparation of recombinant purified GST-Amphiphysin2 SH3 domain protein. The application for this protein is to prepare an SH3 affinity resin that can be utilized to purify untagged full-length Dynamin1 protein from any source. GST-tagged Amp2SH3 (residues 494−588) binds to glutathione sepharose

beads and creates a Dynamin1 affinity resin. This allows you to affinity purify Dynamin1 using the Amphiphysin SH3 domain and Dynamin1 proline-rich domain interaction (Owen et al., 1998).

1.2.1 SH3 domain protein overexpression in E. coli

The same protocol and reagents as the BAR domain protein overexpression in *E. coli* can be followed for the transformation and overexpression of SH3 domain (Section 1.1.1).

1.2.1.1 Reagents, equipment, and buffers

- Human Amphiphysin SH3 (Amp2SH3) gene cloned in pGEX6p1 expression vector. This vector introduces an N-terminal GST tag followed by a PreScission protease recognition site.
- Same reagents as protocol step 1.1.1.1.1 for transformation.
- Same reagents as protocol step 1.1.1.2.1 for protein overexpression.

1.2.1.2 Detailed protocol

Same protocol as BAR domain protein overexpression in *E. coli*. Follow protocol steps 1.1.1.1.2 for transformation and protocol steps 1.1.1.2.2 for protein overexpression.

1.2.2 SH3 domain protein purification and storage

The same protocol and reagents as the BAR domain protein purification and storage (Section 1.1.2) can be followed for the purification of the Amp2SH3 protein with the following alterations to the protocol.

1.2.2.1 Reagents, equipment, and buffers

- Same reagents as protocol step 1.1.2.1
- BL21 (DE3) RIPL Amp2SH3 cell pellet
- Reduced glutathione (Sigma–Aldrich, G4251, St Louis, MO)
- SH3-buffer A: 300 mM KCl, 50 mM Tris pH 8.0, 5 mM imidazole, 1 mM DTT
- SH3-buffer B: 300 mM KCl, 50 mM Tris pH 8.0, 5 mM imidazole, 1 mM DTT, 20 mM glutathione.

1.2.2.2 Detailed procedure

1. Follow protocol steps 1.1.2.2.1 to 1.1.2.2.10 except with BL21 (DE3) RIPL Amp2SH3 cell pellet as the starting material.
2. Bind the clarified filtered Amp2SH3 lysate to the glutathione sepharose beads for 4–12 h at 4 °C.
3. Allow the unbound protein to flow through a gravity column.
4. Wash unbound protein impurities with 40 bed volumes of SH3-buffer A.
5. Elute the Amp2SH3 with 10 bed volumes of SH3-buffer B containing 20 mM reduced glutathione.

6. Concentrate the eluate with 3 kDa MWCO centrifugal concentrators to a final volume of 5 mL.
7. Dialyze the Amp2SH3 protein using a 3 kDa MWCO dialysis tubing against 2 L SH3-buffer B for 12 h at 4 °C.
8. Evaluate protein purity and molecular weight with SDS-PAGE followed by Coomassie blue staining.
9. Calculate protein concentration using a spectrophotometer.
10. Divide the purified protein into 10 mg aliquots (single use) using micro-centrifuge tubes. Flash freeze the tubes in liquid nitrogen and store at −80 °C. These aliquots contain sufficient protein for the generation of an SH3 affinity resin (Section 1.2.3).

1.2.3 Preparation of an SH3 affinity resin

This protocol is to be followed for the purification of untagged Dynamin1 (protocol step 1.3.3).

1.2.3.1 Reagents, equipment, and buffers

- Amp2SH3 purified protein
- Glutathione sepharose 4 fast flow affinity beads (GE, 17513202, Uppsala, Sweden)
- Glass gravity columns 25 mm ID; 200 mm length (Kimble Chase, K420400-2520, Vineland, NJ)
- SH3-buffer A: 300 mM NaCl, 50 mM Tris pH 8.0, 5 mM Imidazole, 1 mM DTT.

1.2.3.2 Detailed procedure

1. Thaw a 10 mg aliquot of Amp2SH3 protein on ice.
2. Prepare an affinity column by loading 5 mL (bed volume) of glutathione sepharose bead slurry into a glass gravity column prefilled with deionized water.
3. Wash beads with ≥200 mL of deionized water. Elute 95% of the buffer from the column ensuring that the beads remain in solution and are kept at 4 °C for all affinity column steps.
4. Equilibrate beads with three 100 mL washes of SH3-buffer A.
5. Apply 10 mg purified Amp2SH3 onto the glutathione sepharose beads and incubate at 4 °C for 2–4 h with gentle rocking.
6. Allow the unbound protein to flow through the gravity column.
7. Wash the beads with 40 bed volumes of SH3-buffer A to remove any unbound Amp2SH3.
8. The column is ready for the Purification of Dynamin1 via the SH3 affinity resin (Section 1.3.3).

1.3 EXPRESSION OF FULL-LENGTH, UNTAGGED DYNAMIN1 IN INSECT CELLS

1.3.1 Preparation of viruses

This protocol is to produce high-titer recombinant baculovirus stock of Dynamin1 (Warnock, Terlecky, & Schmid, 1995). This protocol is prepared according to the Expression Systems protocol. All information detailed here is also found in the Expression Systems protocols.

1.3.1.1 Reagents, equipment, and buffers

- Human Dynamin1 gene cloned in pVL1392 Baculovirus transfer vector
- 125 mL Erlenmeyer culture flasks (Corning, 431143, Corning, NY)
- BSL2 biological fume hood
- Spodoptera frugiperda (Sf9) cells
- 1.5 mL sterile microcentrifuge tubes
- Lipofectamine 3000 (Life Technologies, L3000-015, Carlsbad, CA)
- 24 deep well block (Life Technologies, CS15124, Carlsbad, CA)
- ESF 921 Insect Cell Culture Medium, Protein-Free (Expression Systems, 96-001, Davis, CA)
- Transfection-buffer A: 2 μg recombinant transfer vector, 0.5 μg linearized viral DNA, 100 μL transfection medium
- Transfection-buffer B: 6 μL lipofectamine 3000, 100 μL transfection medium.

1.3.1.2 Detailed protocol

All cell transfer and reagent mixing steps need to be performed in a BSL2-certified biological tissue culture hood.

1.3.1.2.1 Generation of P0 viral stock

1. Inoculate 1×10^6 SF9 cells in 0.5 mL ESF 921 media per well of a 24 deep well block.
2. Mix solution A and incubate for 5 min.
3. Mix solution B and incubate for 5 min.
4. Combine transfection-buffer A and B and incubate at room temperature for 30 min.
5. Add 1 mL of transfection media to the well of SF9 cells and incubate at 27 °C for 4–5 h.
6. Add 3 mL ESF 921 to the well.
7. Cover the wells and incubate at 27 °C with 120–150 rpm orbital shaking for 4–5 days.
8. Clear cell debris with a 2500 rpm room temperature spin for 5 min and collect and save the supernatant as the P0 viral stock. Store all viral stock solutions in light-protected containers and keep at 4 °C.

1.3.1.2.2 Generation of P1 viral stock

1. In a 125 mL Erlenmeyer culture flask transfer SF9 cells grown at mid-log phase to a final concentration of 1×10^6 cells/mL with a final volume of 30 mL.

2. Grow cells for 24 h at 27 °C with gentle shaking.
3. Inoculate the culture with 0.5 mL of P0 viral stock.
4. Incubate infected cells for 4–5 days at 27 °C with gentle shaking.
5. Clear cell debris with a 2500 rpm room temperature spin for 5 min and collect and save supernatant at P1 stock.
6. Titer virus to determine multiplicity of infection (MOI) by performing viral plaque assay (refer to Expression Systems protocol here: www.expressionsystems.com/documents/Plaque%20Assay.pdf).
7. Typical P1 titers are 1×10^6–1×10^8 infectious units per mL. P1 virus can be stored at −80 °C in aliquots sufficient to generate P2 viral stocks.

1.3.1.2.3 Generation of P2 viral stock

1. Follow the same protocol as for the P1 viral stock but infect the cells at an MOI of 0.1.
2. Use the following equation to determine the volume of P1 stock to obtain a specific MOI.
3. Inoculum required (mL) = Desired MOI (pfu/cell) × number of cells/titer of viral stock (pfu/mL).
4. Typical P2 titers are 5×10^8 infectious units per mL.

1.3.1.2.4 Generation of P3 viral stock

1. Follow the same protocol as for the P1 viral stock using P2 stock to infect. Excessive passage of baculovirus can cause unwanted mutations or undesirable variants of baculovirus amplifying in your stock culture. Therefore, it is recommended to use P2 or P3 stocks for infection of expression cultures. It is better to regenerate the P2 and P3 viral stocks from saved P1 viral stocks when additional virus is required.

1.3.2 Infection and culture of SF9 cells

1.3.2.1 Reagents, equipment, and buffers

- P2 or P3 Dynamin1 virus
- 125 mL Erlenmeyer culture flasks (Corning, 431143, Corning, NY)
- 2.8 L unbaffled Fernbach flasks (Corning, 4420-2XL, Corning, NY)
- Gentamicin (Life Technologies, 15750-060, Carlsbad, CA)
- 25 mL transfer pipette
- Centrifuge with Avanti JLA 8.1 rotor (Beckman Coulter, Indianapolis, IN) or equivalent
- 1 L centrifuge bottles (Beckman Coulter, 363676, Indianapolis, IN)
- ESF 921 Insect Cell Culture Medium, Protein-Free (Expression Systems, 96-001, Davis, CA).

1.3.2.2 Detailed procedure

1. In a 2.8 L unbaffled Fernbach flask, transfer SF9 cells grown at mid-log phase to a final concentration of 1.8×10^6 to 2.0×10^6 cells/mL with a final volume of

500 mL with ESF 921 media. Add gentamicin to a final concentration of 10 μg/mL to prevent bacterial contamination.
2. Grow cells at 27 °C with gentle shaking until cells have reached a culture density of 1.0×10^6 cells/mL.
3. Inoculate the culture with 10 mL of P2 viral stock.
4. Incubate the infected cells for 48 h at 27 °C with 150 rpm shaking. Forty-eight hours infection time is optimal for Dynamin1 purification as longer incubations tend to lead to increased degradation of Dynamin1. The C-terminal proline-rich domain is susceptible to cleavage from the protein during longer viral incubations.
5. Collect the cells with a 2500× g spin for 10 min at 4 °C in 1 L centrifuge tubes and Avanti JLA 8.1 rotor.
6. Remove the supernatant and resuspend the cells in 50 mL fresh ESF 921 media per 500 mL cell culture pellet with gentle shaking for 5 min.
7. Collect the resuspended cell pellet in a disposable 50 mL centrifuge tube.
8. Spin the tubes in a benchtop swinging bucket centrifuge at 2500 rpm at 4 °C.
9. Remove the supernatant. The cells can be stored at −80 °C until the purification steps. Typical yields are 5−10 g of cell pellet per 500 mL culture.

1.3.3 Purification of Dynamin1 via SH3 affinity resin

This procedure utilizes an affinity resin comprised of glutathione sepharose beads bound to GST amphiphysin-2 SH3 domain (Owen et al., 1998). The Amp2SH3 domain captures full-length Dynamin1 through a high affinity interaction with its PRD.

1.3.3.1 Reagents, equipment, and buffers

- SH3 affinity resin as prepared in 1.2.3.2
- Protease inhibitor cocktail tablets (Roche, 05892791001, Mannheim, Germany)
- Glass gravity columns 25 mm ID; 200 mm length (Kimble Chase, K420400-2520, Vineland, NJ)
- 100 mL glass dounce tissue homogenizer (Kimble Chase 885303, Vineland, NJ)
- 32 mL tube, thick wall, polycarbonate (Beckman Coulter, 355631, Indianapolis, IN)
- Centrifuge and 50.2 Ti fixed angle rotor (Beckman Coulter, 337901, Indianapolis, IN)
- Vivaspin 50 kDa MWCO centrifugal concentrator (Sartorius Stedim Biotech VS2031)
- 0.45 μm syringe filter (Thermo Fisher Scientific, 190-9945, Waltham, MA)
- Rocker shaker
- SDS PAGE supplies
- Dynamin-buffer A: 150 mM NaCl, 20 mM HEPES pH 7.4, 1 mM EGTA, 1 mM DTT, 5% (v/v) glycerol, Protease inhibitor cocktail tablets (Roche)
- Dynamin-buffer B: 150 mM NaCl, 20 mM HEPES pH 7.4, 1 mM EGTA, 1 mM DTT, 5% (v/v) glycerol

- Dynamin-buffer C: 1.2 M NaCl, 20 mM PIPES pH 6.5, 1 mM DTT, 5% glycerol
- Dynamin-buffer D: 100 mM NaCl, 20 mM HEPES pH 7.4, 50% glycerol.

1.3.3.2 Detailed procedure

1. Thaw Dynamin1 SF9 cell pellets on ice.
2. Add 50 mL of Dynamin-buffer A per 10 mL of cell pellet.
3. Obtain a homogeneous mixture with gentle vortex mixing.
4. Lyse the cells by tissue grinding the solution in a 100 mL glass dounce.
5. Initial 10 plunges with course (smaller) pestle and final 10–40 plunges with fine pestle.
6. A small sample may be directly visualized under a compound light microscope to ensure all cells have been lysed.
7. Clear the lysate with ultracentrifugation at 45,000× g for 1 h at 4 °C.
8. Filter the cleared lysate supernatant through a 0.45 μm syringe filter (PN) and collect into a clean beaker on ice.
9. During the centrifugation step prepare the SH3 affinity resin according to procedure steps 1.2.3.
10. Add the cleared filtered Dynamin1 lysate to the column and allow protein binding for 4 h with gentle rocking at 4 °C.
11. Allow the supernatant to flow through the column and collect this entire fraction.
12. Wash the beads with 40 bed volumes of Dynamin-buffer B. Elute Dynamin1 off of the column with 10 bed volumes of Dynamin-buffer C.
13. Evaluate the purity and molecular weight of the eluate with SDS-PAGE followed by Coomassie blue staining.
14. Concentrate the eluate to 1–5 mL using centrifugal concentrators.
15. Dialyze the concentrated eluate into Dynamin-buffer D for 8–16 h at 4 °C.
16. Flash freeze the dialyzed protein in 50 μL (single use) aliquots with liquid nitrogen and store the protein at −80 °C.

1.4 MAKING MODEL MEMBRANES

1.4.1 Approximating target membrane lipid species distribution

Membranes that outline different cellular compartments have evolved to be comprised of different lipid compositions (van Meer, Voelker, & Feigenson, 2008). For example, the lipid composition of the plasma membrane differs markedly from that of the mitochondria. When one designs in vitro reactions that involve the use of model membranes, care should be taken to reflect the composition of the relevant target membrane in the cell and its lipid specificities. For example, in the steady state, the mitochondrial membrane has the relatively rare lipid cardiolipin, among other more abundant "structural" lipids such as phosphatidylcholine (PC) and phosphatidylethanolamine (PE). Phosphatidylinositol (PI)-3-phosphate (PI3P) is enriched on the early endosomes, PI(3,5)P2 on late endosomes, PI(4,5)P2 on the plasma membrane, and PI(4)P on the golgi apparatus, among other examples. In most cases,

the molar percentage of cholesterol also varies between various membranes within the cell.

1.4.2 Use of defined biological sources

1.4.2.1 Reagents, equipment, and buffers

- Brain extract from bovine type 1 Folch fraction 1 (Sigma–Aldrich, B1502, St Louis, MO)
- Phosphatidylethanolamine (PE) (Avanti Polar Lipids, 840022, Alabaster, AB)
- Phosphatidylserine (PS) (Avanti Polar Lipids, 840032, Alabaster, AB)
- 1-Palmitoyl-2-oleoyl-*sn*-glycero-3-phospho-L-serine (POPS) (Avanti Polar Lipids, 840034, Alabaster, AB)
- 1,2-Dioleoyl-*sn*-glycero-3-phospho-L-serine (DOPS) (Avanti Polar Lipids, 840035, Alabaster, AB)
- L-α-Phosphatidylinositol (PI) (Avanti Polar Lipids, 840042C, Alabaster, AB)
- L-α-Phosphatidylinositol-4,5-bisphosphate ($PI(4,5)P_2$) (Avanti Polar Lipids, 840046, Alabaster, AB)
- 1,2-Dioctanoyl-*sn*-glycero-3-(phosphoinositol-3-phosphate) (PI3P) (Avanti Polar Lipids, 850187, Alabaster, AB)
- 1,2-Dioleoyl-*sn*-glycero-3-phospho-(1′-myo-inositol-5′-phosphate) (PI5P) (Avanti Polar Lipids 850152P, Alabaster, AB)
- L-α-Phosphatidylcholine (PC) (Avanti Polar Lipids, 840051C, Alabaster, AB)
- Cholesterol (Avanti Polar Lipids, 700000P, Alabaster, AB).

There are multiple sources of lipids used as model membranes in the laboratory. Popular examples include lipid mixtures like the Folch fractions which are extracts from tissues using organic solvent-based procedures (Folch, 1957). These fractions are subsets of the total lipid makeup of membranes from a specific tissue, such as the brain in the case of the bovine brain lipid extract. Other sources include soybean, heart muscle, and semipurified mitochondrial lipid extracts. The major components of these mixtures are phospholipids including PC, PE, and PS.

In other cases, the lipid composition desired may be a simpler mix of defined components. For example, if you are testing whether a protein binds to a specific lipid species you will need to make a defined model membrane that contains or omits this lipid at a given molar ratio. Many individual lipid species are available as pure powders or dissolved in chloroform from commercial vendors. It is convenient to know the molarity of your stocks beforehand so that you can add components in the molar ratios that you desire. Some commonly available lipids that are major structural components of cellular membranes are POPS, DOPS, PI, Cardiolipin, PI(4,5)P2, PI3P, PI4P, PI5P, and PC among others. Cholesterol is also a major structural component in most membranes that should be included between 20 and 30 mol%.

1.4.3 Preparation of vesicles

1.4.3.1 Reagents, equipment, and buffers

- Lipid stocks dissolved in chloroform

- Glass vials (Agilent 5182-0714, Santa Clara CA)
- PFA-Teflon tips (Elemental Scientific, ES-7000-1001, Omaha NE)
- Vortexer
- Gaseous Nitrogen/Argon
- Vacuum source
- N-hexane (Sigma–Aldrich, 139386, St Louis, MO)
- 10 mm filter supports (Avanti Polar Lipid, 610014, Alabaster, AB)
- Whatman nucleopore track-etch membrane (Avanti Polar Lipids, 800319, Alabaster, AB)
- Resuspension buffer—20 mM HEPES pH 7.5, 150 mM KCl
- Bath sonicator
- Avanti liposome mini-extruder setup (Avanti Polar Lipids, 610000, Alabaster, AB)
- Hamilton gastight syringe (Avanti Polar Lipids 610017, Alabaster, AB).

1.4.3.2 Detailed procedure

1. Add the required lipid components in the desired molar ratios to a glass vial. The final volume of each lipid species added to the mix depends upon the molar stock concentration. Long exposure of plastics to organic solvents can result in leaching of plastic and contamination of lipid stocks. Therefore it is essential to use glass micropipettes or PFA-Teflon tips with lipid solutions in chloroform.
2. Take the glass vial to a fume hood. Gently vortex to mix the components. While vortexing, introduce a steady flow of an inert gas such as nitrogen or argon at the mouth of the tube. The purpose of doing this is to create an inert atmosphere to prevent oxidation of lipids while they are dried.
3. Keep vortexing under the steady flow of nitrogen/argon till the liquid dries out and the lipid forms a film all around the sides of the glass vial.
4. Attach the glass tube to a vacuum source such as a lyophilizer to pump out residual chloroform for 1 h.
5. Resuspend the lipid film in 500 μL absolute n-hexane to remove residual chloroform trapped within the lipid film. Repeat the vortexing step under inert gas until you obtain the thin lipid film again.
6. Attach the glass tube to a vacuum source such as a lyophilizer to pump out residual chloroform for 4 h or overnight.
7. Resuspend the lipid film in your resuspension buffer to obtain a final concentration of no more than 2 mg/mL total lipid.
8. Shake lightly to resuspend most of the lipid film in the buffer. If there is some lipid film left on the walls of the tube, use gentle vortexing to remove it from the wall.
9. Incubate overnight at 4 °C with gentle rocking.
10. Membranes can be aliquoted (50–100 μL aliquots) and stored at −80 °C after flash freezing in liquid nitrogen.

In the method described above, liposomes are formed by the hydration of lipid films that detach from the walls of the glass vial on agitation, simultaneously forming

closed spherical vesicles. This generally leads to a majority of the liposomes being multilamellar, meaning that there are vesicles within vesicles ("onions"). For most downstream experiments such as flotation or reverse sedimentation assays (protocol step 1.5.2) or in vitro membrane remodeling reactions with BAR domain-containing proteins or dynamins (protocol step 1.6.2), unilamellar vesicles are essential. There are two major methods available to increase the percentage of unilamellar vesicles in the mixture:

1. Sonication: Sonication disrupts the large multilamellar vesicles formed after rehydration of lipid films and breaks them up into very small and predominantly unilamellar vesicles (SUVs) that are curvature limited (15–50 nm in diameter). Following sonication, repeated freeze/thaw cycles (up to 10) after the formation of SUVs results in spontaneous fusion of these small vesicles and results in larger unilamellar vesicles.
   a. Sonicate membranes for 5 min in a water bath sonicator at maximum power.
   b. Flash freeze the membranes, thaw by keeping in a water bath at room temperature.
   c. Repeat the freeze and thaw cycle 10 times.
   d. Flash freeze membranes and keep at −80 °C until further use.
2. Extrusion: Using the Avanti liposome extruder, a liposome solution can be repeatedly made to pass through polycarbonate membranes of defined pore sizes. This process, like sonication, breaks and reseals vesicles and increases the number of unilamellar vesicles in the solution. This also introduces an upper size limit on the vesicles. In our hands, forcing a liposome suspension through a polycarbonate membrane of pore size 1 μm ~20 times yields a unilamellar vesicle population with a mean diameter of ~200 nm.
   a. Set up the extruder as per the instructions of the manufacturer. Use a 1 μm pore size membrane (refer to http://www.avantilipids.com/index.php?option=com_content&view=article&id=185&Itemid=193 for details of usage for the Avanti mini extruder). To minimize sample loss, prewet the membrane and membrane supports.
   b. Fill up the gastight syringe (syringe 1) with the liposome solution, attach it to one end of the mini-extruder. Attach an unfilled syringe (syringe 2) on the other available side.
   c. Gently push the liquid through the extruder setup, into the syringe on the other side. Push it back to the syringe 1.
   d. Repeat the process 20 times.
   e. Collect the liposomes from syringe 2.
   f. Aliquot into 100 μL aliquots, flash freeze and store at −80 °C.

1.5 MEASURING MEMBRANE BINDING

Once liposomes having the desired lipid composition have been prepared, protein binding to these membranes can be tested qualitatively by two major methods.

Each method has strengths and weaknesses and we will discuss these in Section 1.5.3 after describing the protocols (Figure 3).

1.5.1 Flotation or reverse sedimentation (Figure 3(A))

1.5.1.1 Reagents, equipment, and buffers

- Purified protein
- Liposomes
- 1 mL ultracentrifuge tubes (Beckman Coulter, 343778, Indianapolis, IN)
- Ultracentrifuge with TLS-55 rotor (Beckman Coulter, 346936, Indianapolis, IN)
- Methanol (Sigma–Aldrich, 179337, St Louis, MO)
- 2X Laemmli buffer (Bio-Rad, 161-0737, Hercules, CA)
- Chloroform (Sigma–Aldrich, 319988, St Louis, MO)
- Balance
- SDS PAGE supplies
- Sucrose-buffer A: 2 M sucrose, 20 mM HEPES pH 7.5, 100 mM KCl
- Sucrose-buffer B: 1 M sucrose, 20 mM HEPES pH 7.5, 100 mM KCl
- Sucrose-buffer C: 0.5 M sucrose, 20 mM HEPES pH 7.5, 100 mM KCl
- Buffer-D: 20 mM HEPES pH 7.5, 100 mM KCl.

1.5.1.2 Detailed procedure

1. Mix protein and liposomes with a molar ratio of 1000:1 lipid:protein.
2. Incubate at 4 °C for 1 h. In the case of Drp1 and MiD49, we noticed turbidity upon incubating Drp1 with liposomes at room temperature. Thus, to rule out any aggregation that may have caused the turbidity, the mixture was incubated at 4 °C for an hour to ensure optimal binding. The solution remained clear at 4 °C.
3. Transfer the mixture into an ultracentrifuge tube.
4. Homogenize the mixture with 300 μL of Sucrose-buffer A.
5. Mark the upper boundary of the layer on the outside of the tube with a marker. Carefully pipetting, add 150–300 μL Sucrose-buffer B followed by 300 μL Sucrose-buffer C. Mark the upper boundary of each layer.
6. Balance the tubes using buffer D.
7. Spin the tubes in a prechilled TLS-55 rotor at 175000× g for 45 min at 4 °C.
8. Without disturbing other layers, carefully collect each sucrose layer separately and pipette into a microcentrifuge tube.
9. Methanol chloroform precipitation to estimate protein from sucrose layers (steps 9–16): To the sucrose layer that was collected (volume 150–300 μL), add 400 μL methanol, 100 μL chloroform followed by 300 μL water. Vortex and keep on ice for 5 min.
10. Spin at 12,000× g for 5 min in a benchtop centrifuge at room temperature.
11. Carefully remove the upper layer without disturbing the interface.
12. Add 300 μL methanol, vortex.

13. Spin at 12,000× g for 10 min at room temperature. Carefully remove the liquid phase without disturbing the protein pellet.
14. Add 30 μL 2X Laemmli sample buffer and mix well.
15. Analyze the amount of protein in each layer by SDS PAGE followed by Coomassie blue staining.
16. Analysis of the resulting SDS PAGE gel will identify if the protein bound the liposome membrane. Membrane bound protein will be detected in the 0.5 M sucrose layer and unbound proteins will be detected in the 2 and 1 M sucrose layer. Comparison with positive controls (robust membrane binding proteins, e.g. EndophilinA1) and negative controls such as purified GST is essential.

1.5.2 Sedimentation (Figure 3(B))

1.5.2.1 Reagents, equipment, and buffers

- Liposomes
- Purified protein
- Benchtop centrifuge
- 2X Laemmli buffer (Bio-Rad, 161-0737, Hercules, CA)
- Sedimentation-buffer A: 20 mM HEPES pH 7.5, 75 mM KCl.

1.5.2.2 Detailed procedure

1. Mix the liposomes and protein with a molar ratio of 1000:1 lipid:protein.
2. Incubate the mixture for 1 h at 4 °C.
3. Spin the mixture at 12,000× g for 5 min at room temperature to pellet liposomes.
4. Remove the supernatant and mix 1:1 with 2X Laemmli sample buffer. This is the unbound fraction.
5. Wash the pellet with the sedimentation-buffer A.
6. Spin again at 12,000× g for 5 min at room temperature. Collect the supernatant and mix 1:1 with 2X Laemmli sample buffer. This is the wash fraction.
7. Resuspend the pellet in Laemmli sample buffer. This is the bound fraction.
8. Analyze the amount of protein in each fraction by SDS-PAGE followed by Coomassie blue staining.
9. For a positive control like EndophilinA1, at a molar ratio of 1000:1 lipid to protein, >90% protein should pellet in the liposome fraction.

1.5.3 Special considerations and common problems

The solution conditions and lipid to protein ratios for the experiments described above may have to be determined empirically for each protein. For example, at a low lipid to protein ratio (40:1 molar ratio, which is approximately 1:1 by mass) and at low ionic strength (100 mM KCl), most of the vesicles in the reaction will be remodeled by EndophilinA1 and will be densely coated with protein (see Figure 5, for example). These dense structures will not "float" in a reverse sedimentation assay. However, using a vast excess of lipid reduces the number of densely decorated tubules and the more sparsely-bound liposomes will remain buoyant.

In general, the sedimentation assay should be avoided for proteins that have a tendency to oligomerize or aggregate under the buffer conditions of the assay. These proteins will pellet on spinning and can give false positive results for liposome binding. For this reason, aggregated or assembled fractions of these proteins should be removed prior to the experiment. This can be done by either preclearing the protein with a 20,000× g spin for 20 min prior to incubating it with liposomes, or using fresh protein off the size exclusion chromatography column.

The reverse sedimentation assay is a more stringent test for liposome-binding proteins. For a protein to show positive binding in this assay, the strength of interaction between the lipid membrane and protein should be high enough to survive a high speed ultracentrifugation spin for 45 min and migration through protein-free layers of the gradient. For well-characterized lipid-binding proteins such as EndophilinA1, we have observed >90% binding at concentrations of ~2 μM. By contrast, proteins with a high rate of dissociation from the lipid are likely to dissociate during the centrifugation step. Such proteins will be observed in the intermediate layers or the bottom layer and this can lead to a false negative result. For this reason, binding conditions such as buffers, pH, and salt conditions for optimal binding may have to be determined empirically for these proteins.

1.6 RECONSTITUTING MEMBRANE REMODELING MACHINES

Once purified protein and lipid substrates have been generated the next step is to reconstitute in vitro the assembly of these membrane remodeling factors. With these protocols, we describe the (1) membrane-free copolymer formation for Drp1 and MiD49 and (2) membrane-bound assembly of Dynamin1 and EndophilinA1.

1.6.1 Copolymer formation for Drp1 and MiD49

Drp1 localizes to the mitochondrial surface via adaptor proteins. We previously found that Drp1 not only interacts, but also coassembles with the adaptor protein MiD49 in conditions of low ionic strength and in the presence of a nonhydrolyzable analog of GTP (Koirala et al., 2013). Coassembly was characterized using electron microscopy. The following protocol is generalized for the coassembly of Drp1 with a soluble truncation of MiD49.

1.6.1.1 Reagents, equipment, and buffers

- Purified Drp1 and MiD49 protein
- Assembly buffer: 20 mM HEPES pH 7.5, 25 mM KCl, 200 mM GMP-PCP, 2 mM $MgCl_2$, and 1 mM DTT
- Slide-A-Lyzer mini dialysis units (Thermo Fisher 69570, Waltham MA)
- Dilution buffer: 20 mM HEPES pH 7.5, 150 mM KCl.

1.6.1.2 Detailed procedures

1. Thaw protein stocks on ice.

2. Preclear the protein by spinning at 12,000× g to remove any aggregate that may have formed upon thawing.
3. Measure the concentration of the protein.
4. In a microcentrifuge tube, add the proteins in 1:1 molar ratio. Dilute proteins as required using the dilution buffer.
5. Prepare the assembly buffer. Gently place the protein mixture into the dialysis unit and place the dialysis unit into the assembly buffer.
6. Dialyze overnight at room temperature.
7. Collect the solution from the dialysis unit with gentle pipetting for further analysis.

1.6.2 Coassembly of Dynamin1 with EndophilinA1 around membrane tubules

We have made recent progress in reconstituting the assembly of a heteropolymer composed of Dynamin1 and EndophilinA1 that assembles around narrow endocytic tubules but whose function is largely unknown (Figure 5, Boucrot et al., 2014; Farsad et al., 2001; Meinecke et al., 2013). To our surprise and by contrast with dynamin alone, this cocomplex cannot mediate fission in vitro. Our initial studies hint at the mechanism underlying tubule elongation and fission inhibition: adjacent turns of the Dynamin1 helix are spaced widely apart in comparison with the Dynamin1 homopolymer (Figure 5). This expanded spacing appears to be due to the interleaving EndophilinA1 molecules which prevent adjacent turns of the Dynamin spiral from interacting and thereby block mechanochemical constriction caused by GTP hydrolysis (Figure 5).

1.6.2.1 Reagents, equipment, and buffers

- Purified Dynamin1 and EndophilinA1 protein
- DOPS: Cholesterol (9:1 molar ratio) liposomes with 10 freeze/thaw cycles
- GTP (Jena Bioscience, NU-1012, Jena, Germany)
- GDP (Jena Bioscience, NU-1172, Jena, Germany)
- GMP-PCP (Sigma–Aldrich, M3509, St Louis, MO)
- GTPγS (Jena Bioscience, NU-412, Jena, Germany).

1.6.2.2 Detailed procedures

1. Thaw the protein and liposome stocks on ice.
2. Preclear protein stocks by spinning at 12,000× g to remove any aggregates.
3. Add liposomes, Dynamin1 and EndophilinA1 in the molar ratio 2:1:1. In general most reactions are conducted between 1 and 5 μM final protein concentrations in a final volume of 10–50 μL for TEM grid preparation. Remarkably, the Dynamin1 and EndophilinA1 copolymer forms on lipid templates regardless of the order of addition to the reaction.
4. Add desired Dynamin1 guanine nucleotide derivative (GDP, GTP, GMP-PCP, or GTPγS) to tubulation reaction. Final guanine nucleotide concentration of 0.5–5 mM.

5. Incubate for 20 min at room temperature. Longer incubations (>1 h) at 4 °C will also generate membrane remodeled protein tubules. The tubulation reaction reaches equilibrium after 20 min at room temperature.
6. Collect the membrane-bound Dynamin1 and EndophilinA1 complex for further functional or structural characterizations by gentle pipetting.

1.7 VISUALIZING MEMBRANE REMODELING

1.7.1 Preparation of samples for negative stain electron microscopy

The described protocol below is our preferred method for preparing negative stain grids. There are many variations in the preparation of negative stain TEM grids. These variations include the type of stain, timing of each step, addition or deletion of wash steps, and the type of filter paper utilized. Successfully stained TEM grids may be achieved with alternative methodologies (Booth, Avila-Sakar, & Cheng, 2011). Figures 4(A,B) and 5(A–C) are examples of negative stain grids prepared according to this procedure.

1.7.1.1 Reagents, equipment, and buffers

- Membrane bound protein sample
- Forceps
- Formvar carbon film on 200 mesh copper grids (Electron Microscopy Sciences, FCF-200-Cu, Hatfield, PA)
- 2% w/v uranyl acetate (Structure Probe Inc., 02624-AB, West Chester, PA)
- Pelco easiGlow glow discharge cleaning system (Ted Pella, 91000, Redding, CA)
- #1 Whatman filter paper (GE, 1001-055, Little Chalfont, UK)
- Storage grid box
- Glass slide
- Parafilm
- Sample wash buffer.

1.7.1.2 Detailed procedure

1. Prepare glow-discharged carbon-coated grids.
2. Using forceps, place the carbon-coated grids onto a glass slide with their carbon side up.
3. Set glow discharge settings to the following conditions: Negative polarity, 30 s hold time, 30 s glow time, 15 mA current, and 0.39 mBar vacuum pressure.
4. Capture a grid with reverse force forceps by gripping the outermost edge of the grid.
5. Prepare sample washes and stain by pipetting 5–40 μL droplets onto the wax surface of a piece of Parafilm. Two sample wash droplets and two 2% uranyl acetate droplets should be prepared. Sample wash buffer can be deionized water but we prefer to use the sample buffer.
6. Apply 2.5–5.0 μL of the membrane bound protein sample onto the carbon side of the grid and let it absorb for 30–60 s.

7. Wick away all moisture by blotting the edge of the grid against the surface of a piece of filter paper at a 90° angle.
8. Immediately immerse the carbon side of the grid onto the surface of the first wash droplet for 5 s while maintaining a hold of the grid with the forceps.
9. Move to the second wash droplet and hold for 5 s.
10. Move to the first stain droplet and hold for 5 s.
11. Wick away all excess stain by blotting the edge of the grid against the surface of a piece of filter paper at a 90° angle.
12. Immerse the carbon side of the grid onto the surface of the second stain droplet and hold for 30 s.
13. Wick away all excess stain by blotting the edge of the grid against the surface of a piece of filter paper at a 90° angle.
14. Allow the grid to air dry for 2 min and then place in a grid storage holder. The stained grid will usually remain stable for months in low humidity environments. To ensure stability of the negative stain grids use a vacuum desiccation chamber to store the grids.

1.7.2 Vitrification of samples for electron cryomicroscopy

1.7.2.1 Reagents, equipment, and buffers

- Copolymer protein assembly
- Liquid nitrogen
- Compressed ethane gas
- FEI Vitrobot Mark III (FEI, Hillsboro, OR)
- Pelco easiGlow glow discharge cleaning system (Ted Pella, 91000, Redding, CA) or equivalent
- Vitrobot prepunched filter paper (Ted Pella, 47000-100, Redding, CA)
- Tweezer assembly for Vitrobot Mark III (Ted Pella, 47000-500, Redding, CA)
- Cryo storage grid box (Ted Pella, 160-40, Redding, CA)
- Quantifoil R2/2 holey carbon on 200 mesh copper grids (Structure Probe Inc., 4420C-XA, West Chester, PA) or equivalent
- Liquid nitrogen storage dewar
- Forceps
- Screwdriver.

1.7.2.2 Detailed procedure

The verification protocol described below is the generic protocol that should be utilized when vitrifying your sample for the first time. There is a large amount of variation in generating thin (100–50 μm) vitreous ice. Check with your electron microscopy facility to determine successful blotting settings used for the particular Vitrobot that will be used to generate your samples. Figures 4(C) and 5(D)–(F) were generated using these detailed procedures.

1. Using forceps, place the grids to be vitrified onto a glass slide with their carbon side up.

2. Set glow discharge settings to the following conditions: negative polarity, 30 s hold time, 30 s glow time, 15 mA current, and 0.39 mBar vacuum pressure. There is a wide host of grid treatments that can be utilized to optimize protein adsorption onto the cryo-EM grid.
3. Prepare the Vitrobot apparatus by turning on the power to the machine, opening the FEI software on the computer, and ensuring that air is being supplied to the Vitrobot at >90 psi.
4. Chill the blotting chamber to the desired temperature (4−25 °C) using the temperature settings on the FEI software.
5. Fill the water cylinder with deionized water and set the humidity to 100% on the FEI software.
6. Load prepunched filter paper onto the blotting pads in the blotting chamber.
7. Chill the Vitrobot cup and cryo storage box with liquid nitrogen.
8. Condense liquid ethane in the presence of liquid nitrogen.
9. Load a Quantifoil R2/2 holey carbon on 200 mesh grid onto the forceps by gripping the outermost edge of the grid ensuring that it is well centered. For protein samples that assemble into helical or filamentous polymers we prefer to utilize 2 μm holes with 2 μm spacing. This allows for longer filaments to sit across large areas of the vitreous ice contained within the holes. This is done so that straight segments of the polymers can be imaged for data collection.
10. Lock the forceps together with the forceps clamp.
11. Enter the desired vitrification settings into the software. Blot time: 4 s, blot offset: 0 mm, wait time: 30 s. These settings will need to be optimized upon visualization of the grid to obtain thin vitreous ice. Thick impenetrable ice over the majority of the grid indicates that the sample was underblotted. For this case, increase the blot time or decrease the blot offset to achieve thinner ice. If the cryo-EM grid upon visualization lacks ice in the holes it indicates that the sample was overblotted. Decrease the blot time or increase the blot offset to amend this issue.
12. Load 2.5−5 μL of your sample onto the grid ensuring that the droplet is completely covering the grid surface. Go through the vitrification process that was set on the software.
13. Transfer the vitrified cryo-EM grid into the cryo storage box and secure the lid with a liquid nitrogen chilled screwdriver.
14. Store grids in a liquid nitrogen dewar. Vitrified grids must be stored at liquid nitrogen temperatures (−195 °C) at all times.

1.7.3 Low-dose imaging

Imaging cryo-EM samples requires great care to prevent radiation damage to your biological sample. This protocol will go through the required microscope settings to image a vitrified protein sample and minimize exposure to a dose of ~20 electrons/Å^2. For sample grid transfer and loading the holder in the microscope refer to the following cryo-EM resources (Cabra & Samsó, 2015; Grassucci, Taylor, & Frank, 2007).

1.7.3.1 Reagents, equipment, and buffers

- Liquid Nitrogen
- Vitrified protein sample on holey carbon cryo-EM grid
- Transmission electron microscope (FEI, Tecnai Polara, Hillsboro, OR) or equivalent
- Cryo-transfer holder (Gatan, 626, Pleasanton, CA).

1.7.3.2 Detailed procedure

This procedure begins after you have transferred your cryo-EM grid from storage into a cryo-EM grid holder and have loaded the holder into the microscope.

1. Open the cryo holder shutter and the microscope column valves.
2. Activate low dose and select search mode.
3. Switch to a high spot size (6–10) at ~5000X magnification and lower the beam intensity.
4. Set the eucentric height by activating the alpha-wobbler and adjust the z-height buttons to minimize image movement while looking at the phosphor screen.
5. Move the stage with the right track ball to an unwanted area of the grid with ripped or empty carbon.
6. Select the focus mode and switch to a spot size of 2 at 100 kX magnification or a magnification greater than your setting in the exposure mode. Switch the focus 2 setting to 0 μm offset at 0° and set the focus 1 setting to 1.5 μm offset at 180°. These two settings allow you to have one focus spot directly centered over the exposure spot and the second focus spot a specified distance away from the image collection area to limit beam exposure to your sample. The focus 2 setting then will primarily be utilized to verify your image shift settings as in detailed procedure step 1.7.3.2.9.
7. Ensure that the beam is properly aligned by performing all the direct alignments.
8. Select the exposure mode and switch to a beam spot size of 2 at the magnification at which you would like to collect your data.
9. Switch through all the low-dose modes and ensure that the beam is properly aligned and centered.
10. Check the image alignment between search and exposure modes. To accomplish this, find a discernible feature on the carbon surface in exposure mode and center your field of view over this feature. Switch to search mode and center your field of view over the same identifiable feature using image shift. It is best to use a feature on the surface with high contrast that is unique in the area of the grid in which you are imaging.
11. In search mode, find an area of the grid in which there is thin vitreous ice. Move the center of view to the middle of a hole.
12. Set your beam intensity so that you are detecting 20 electrons/physical pixel/second over your entire exposure time. For example if you collect your images with a 5-s exposure you will want 4.0 electron/physical pixel to hit one pixel of the detector every second.

13. Switch to search mode and center over a hole with thin vitreous ice that contains your protein sample.
14. Switch to focus mode and find eucentric focus using the FFT in digital micrograph by adjusting the z-height. Once focus is found reset the defocus on the microscope.
15. Set defocus to 0.5–4 μm under focus using the focus knob.
16. Switch to exposure mode and acquire the image.
17. Repeat steps 1.7.3.2.12 to 1.7.3.2.15 until no unexposed holes are left. Ensure that the imaging field of view has not been exposed in focus or exposure mode previously when moving to a new area to acquire an image. This is a crucial point that needs to be employed to prevent imaging radiation damaged protein sample.
18. Move to a new grid square when all the holes have been imaged and exposed to the beam. Continue in this manner until you have acquired the desired number of micrographs of your sample.

PERSPECTIVE

This chapter has focused on biochemical methods for purifying and reconstituting membrane remodeling factors for visualization by electron microscopy, rather than on subsequent image analysis and structure determination methods. In many ways, the rate-determining step in studying membrane remodeling phenomena is the biochemical reconstitution of the activity being investigated. Once purification and reconstitution are accomplished, modern electron microscopy and image analysis will almost certainly lead to new molecular and even atomic-resolution insights. The future of this approach is particularly bright. Beam-induced motion was discovered to be the most significant factor limiting the resolution of cryo-EM images and 3D reconstructions, and the invention of direct electron detectors with individual electron detection and subsecond image acquisition has led to innovative software solutions for quantifying and correcting beam-induced motion and for restoring high resolution information (Bai, Fernandez, McMullan, & Scheres, 2013; Campbell et al., 2012; Li et al., 2013). The use of direct electron detectors and modern image analysis algorithms is already revealing the mechanisms of protein–protein and protein–membrane interactions that underlie membrane remodeling phenomena.

ACKNOWLEDGMENTS

Electron microscopy was performed at the University of Utah and the University of California. We thank David Belnap (Utah) and Michael Braunfeld (UCSF) for supervision of the electron microscopes. We thank Anita Orendt and the Utah Center for High Performance Computing and the NSF XSEDE consortium for computational support. We thank Aurelien Roux (University of Geneva), Pietro De Camilli (Yale University), and Janet Shaw (University of Utah) for sharing reagents and for critical discussions. The protocols described here were

developed in part with support from the Searle Scholars Program, NIH/NIGMS grant 1DP2GM110772-01, the United States–Israel Binational Science Foundation BSF2013310, and the Herbert Boyer Junior Faculty Endowed Chair at UCSF. The authors declare no competing financial interests.

REFERENCES

Bai, X. C., Fernandez, I. S., McMullan, G., & Scheres, S. H. W. (2013). Ribosome structures to near-atomic resolution from thirty thousand cryo-EM particles. *Elife, 2013*, e00461.

Booth, D. S., Avila-Sakar, A., & Cheng, Y. (2011). Visualizing proteins and macromolecular complexes by negative stain EM: from grid preparation to image acquisition. *Journal of Visualized Experiments*, (58). http://dx.doi.org/10.3791/3227.

Boucrot, E., et al. (2014). Endophilin marks and controls a clathrin-independent endocytic pathway. *Nature, 517*, 460–465.

Cabra, V., & Samsó, M. (2015). Do's and don'ts of cryo-electron microscopy: a primer on sample preparation and high quality data collection for macromolecular 3D reconstruction. *Journal of Visualized Experiments*, 1–11.

Campbell, M. G., et al. (2012). Movies of ice-embedded particles enhance resolution in electron cryo-microscopy. *Structure, 20*, 1823–1828.

Chappie, J. S., et al. (2011). A pseudoatomic model of the dynamin polymer identifies a hydrolysis-dependent powerstroke. *Cell, 147*, 209–222.

Cossart, P., & Roy, C. R. (2010). Manipulation of host membrane machinery by bacterial pathogens. *Current Opinion in Cell Biology, 22*, 547–554.

Daumke, O., Roux, A., & Haucke, V. (2014). BAR domain scaffolds in dynamin-mediated membrane fission. *Cell, 156*, 882–892.

Doherty, G. J., & McMahon, H. T. (2009). Mechanisms of endocytosis. *Annual Review of Biochemistry, 78*, 857–902.

Elde, N. C., Morgan, G., Winey, M., Sperling, L., & Turkewitz, A. P. (2005). Elucidation of clathrin-mediated endocytosis in tetrahymena reveals an evolutionarily convergent recruitment of dynamin. *PLoS Genetics, 1*. http://dx.doi.org/10.1371/journal.pgen.0010052.

Faelber, K., et al. (2011). Crystal structure of nucleotide-free dynamin. *Nature, 477*, 556–560.

Farsad, K., et al. (2001). Generation of high curvature membranes mediated by direct endophilin bilayer interactions. *The Journal of Cell Biology, 155*, 193–200.

Ferguson, S. M., & De Camilli, P. (2012). Dynamin, a membrane-remodelling GTPase. *Nature Reviews Molecular Cell Biology, 13*(2), 75–88. http://dx.doi.org/10.1038/nrm3266.

Folch, J., Lees, M., & Stanley, G. H. S. (1957). *J. Biol. Chem., 226*, 497–509.

Ford, M. G. J., Jenni, S., & Nunnari, J. (2011). The crystal structure of dynamin. *Nature, 477*, 561–566.

Fröhlich, C., et al. (2013). Structural insights into oligomerization and mitochondrial remodelling of dynamin 1-like protein. *EMBO Journal, 32*, 1280–1292.

Frost, A., et al. (2008). Structural basis of membrane invagination by F-BAR domains. *Cell, 132*, 807–817.

Frost, A., Unger, V. M., & De Camilli, P. (2009a). The BAR domain superfamily: membrane-molding macromolecules. *Cell, 137*, 191–196.

Frost, A., Unger, V. M., & De Camilli, P. (2009b). Boomerangs, bananas and blimps: structure and function of F-{BAR} domains in the context of the {BAR} domain superfamily. *Landes*. http://www.ncbi.nlm.nih.gov/books/NBK7021/.

Gallop, J. L., et al. (2006). Mechanism of endophilin N-BAR domain-mediated membrane curvature. *EMBO Journal, 25*, 2898–2910.

Grassucci, R. A., Taylor, D. J., & Frank, J. (2007). Preparation of macromolecular complexes for cryo-electron microscopy. *Nature Protocols, 2*, 3239–3246.

Henderson, R. (2013). Structural biology: ion channel seen by electron microscopy. *Nature, 504*, 93–94.

Hooke, R. (1665). *Micrographia: Or some physiological descriptions of minute bodies made by magnifying glasses with observations and inquiries thereupon*. http://archive.nlm.nih.gov/proj/ttp/flash/hooke/hooke.html.

Kim, J., et al. (2014). Subnanometre-resolution electron cryomicroscopy structure of a heterodimeric ABC exporter. *Nature, 517*, 396–400.

Koirala, S., et al. (2013). Interchangeable adaptors regulate mitochondrial dynamin assembly for membrane scission. *Proceedings of the National Academy of Sciences USA, 110*, 1300855110.

Kozlov, M. M., McMahon, H. T., & Chernomordik, L. V. (2010). Protein-driven membrane stresses in fusion and fission. *Trends in Biochemical Sciences, 35*, 699–706.

Lackner, L. L., & Nunnari, J. M. (2009). The molecular mechanism and cellular functions of mitochondrial division. *Biochimica et Biophysica Acta – Molecular Basis of Disease, 1792*, 1138–1144.

Laliberté, J.-F., & Sanfaçon, H. (2010). Cellular remodeling during plant virus infection. *Annual Review of Phytopathology, 48*, 69–91.

Liao, M., Cao, E., Julius, D., & Cheng, Y. (2013). Structure of the TRPV1 ion channel determined by electron cryo-microscopy. *Nature, 504*, 107–112.

Li, X., et al. (2013). Electron counting and beam-induced motion correction enable near-atomic-resolution single-particle cryo-EM. *Nature Methods, 10*, 584–590.

Losón, O. C., et al. (2014). The mitochondrial fission receptor MiD51 requires ADP as a cofactor. *Structure, 22*, 367–377.

Low, H. H., Sachse, C., Amos, L. A., & Löwe, J. (2009). Structure of a bacterial dynamin-like protein lipid tube provides a mechanism for assembly and membrane curving. *Cell, 139*, 1342–1352.

Lu, P., et al. (2014). Three-dimensional structure of human γ-secretase. *Nature, 512*(7513), 166–170. http://dx.doi.org/10.1038/nature13567.

Masuda, M., et al. (2006). Endophilin BAR domain drives membrane curvature by two newly identified structure-based mechanisms. *EMBO Journal, 25*, 2889–2897.

McMahon, H. T., & Gallop, J. L. (2005). Membrane curvature and mechanisms of dynamic cell membrane remodelling. *Nature, 438*, 590–596.

McMahon, H. T., Kozlov, M. M., & Martens, S. (2010). Membrane curvature in synaptic vesicle fusion and beyond. *Cell, 140*, 601–605.

van Meer, G., Voelker, D. R., & Feigenson, G. W. (2008). Membrane lipids: where they are and how they behave. *Nature Reviews Molecular Cell Biology, 9*, 112–124.

Meinecke, M., et al. (2013). Cooperative recruitment of dynamin and BAR domain-containing proteins leads to GTP-dependent membrane scission. *The Journal of Biological Chemistry*. M112.444869.

Milosevic, I., et al. (2011). Recruitment of endophilin to clathrin-coated pit necks is required for efficient vesicle uncoating after fission. *Neuron, 72*, 587–601.

Mim, C., et al. (2012). Structural basis of membrane bending by the n-BAR protein endophilin. *Cell, 149*, 137–145.

Morlot, S., et al. (2012). Membrane shape at the edge of the dynamin helix sets location and duration of the fission reaction. *Cell, 151*, 619–629.

Moyer, C. L., & Nemerow, G. R. (2011). Viral weapons of membrane destruction: Variable modes of membrane penetration by non-enveloped viruses. *Current Opinion in Virology, 1*, 44–49.

Osteryoung, K. W., & Nunnari, J. (2003). The division of endosymbiotic organelles. *Science, 302*, 1698–1704.

Owen, D. J., et al. (1998). Crystal structure of the amphiphysin-2 SH3 domain and its role in the prevention of dynamin ring formation. *EMBO Journal, 17*, 5273–5285.

Rahaman, A., Elde, N. C., & Turkewitz, A. P. (2008). A dynamin-related protein required for nuclear remodeling in Tetrahymena. *Current Biology, 18*, 1227–1233.

Richter, V., et al. (2014). Structural and functional analysis of MiD51, a dynamin receptor required for mitochondrial fission. *The Journal of Cell Biology, 204*. jcb.201311014.

Schuske, K. R., et al. (2003). Endophilin is required for synaptic vesicle endocytosis by localizing synaptojanin. *Neuron, 40*, 749–762.

Studier, F. W. (2005). Protein production by auto-induction in high density shaking cultures. *Protein Expr Purif, 41*(1), 207–234.

Szwedziak, P., Wang, Q., Bharat, T. A. M., Tsim, M., & Löwe, J. (2014). Architecture of the ring formed by the tubulin homologue FtsZ in bacterial cell division. *Elife, 3*, e04601.

Verstreken, P., et al. (2002). Endophilin mutations block clathrin-mediated endocytosis but not neurotransmitter release. *Cell, 109*, 101–112.

Warnock, D. E., Terlecky, L. J., & Schmid, S. L. (1995). Dynamin GTPase is stimulated by crosslinking through the C-terminal proline-rich domain. *EMBO Journal, 14*, 1322–1328.

CHAPTER 3

INTERCHANGEABLE ADAPTORS REGULATE MITOCHONDRIAL DYNAMIN ASSEMBLY FOR MEMBRANE SCISSION

Sajjan Koirala, Qian Guo*, Raghav Kalia*, Debra Eckert, Adam Frost and Janet M. Shaw
*- Equal contribution

Interchangeable adaptors regulate mitochondrial dynamin assembly for membrane scission

Sajjan Koirala, Qian Guo[1], Raghav Kalia[1], Huyen T. Bui, Debra M. Eckert, Adam Frost[2], and Janet M. Shaw[2]

Department of Biochemistry, University of Utah School of Medicine, Salt Lake City, UT 84112

Edited* by William T. Wickner, Dartmouth Medical School, Hanover, NH, and approved February 27, 2013 (received for review January 15, 2013)

Mitochondrial fission is mediated by the dynamin-related GTPases Dnm1/Drp1 (yeast/mammals), which form spirals around constricted sites on mitochondria. Additional membrane-associated adaptor proteins (Fis1, Mdv1, Mff, and MiDs) are required to recruit these GTPases from the cytoplasm to the mitochondrial surface. Whether these adaptors participate in both GTPase recruitment and membrane scission is not known. Here we use a yeast strain lacking all fission proteins to identify the minimal combinations of GTPases and adaptors sufficient for mitochondrial fission. Although Fis1 is dispensable for fission, membrane-anchored Mdv1, Mff, or MiDs paired individually with their respective GTPases are sufficient to divide mitochondria. In addition to their role in Drp1 membrane recruitment, MiDs coassemble with Drp1 in vitro. The resulting heteropolymer adopts a dramatically different structure with a narrower diameter than Drp1 homopolymers assembled in isolation. This result demonstrates that an adaptor protein alters the architecture of a mitochondrial dynamin GTPase polymer in a manner that could facilitate membrane constriction and severing activity.

Drp1/Dnm1 | Fis1/Mdv1 | Mff/MiD49/MiD51 | mitochondrial fission dynamin

Dynamin-related proteins (DRPs) are self-assembling GTPases that regulate lipid-remodeling events at different cellular membranes (1). Two of these DRPs, Dnm1 (yeast) and Drp1 (human), play conserved roles in mitochondrial fission, which is important for biological processes including mitochondrial inheritance during cell division (2, 3), clearance of defective mitochondria via mitophagy (4–7), and mammalian development (8, 9).

In vivo, both the Dnm1 and Drp1 GTPases assemble from the cytoplasm into structures that encircle mitochondria at sites of future fission (10–13). In vitro, addition of GTP to Dnm1-lipid tubules is sufficient to constrict synthetic liposomes (14, 15). However, a recent study revealed that mitochondrial constriction in yeast and mammals occurs at sites where endoplasmic reticulum (ER) tubules circumscribe mitochondria (16). This ER-mediated mitochondrial constriction occurs before Dnm1 or Drp1 recruitment, suggesting that DRPs act after the initial constriction event to complete membrane fission. Neither Dnm1 nor Drp1 has been shown to catalyze membrane scission independently in vivo or in vitro.

A variety of adaptor proteins localized to the outer mitochondrial membrane (OMM) play important but poorly understood roles in Dnm1/Drp1 recruitment and function. The membrane recruitment step is understood best in yeast, where Dnm1 binds to the fungal-specific adaptor mitochondrial division protein 1 (Mdv1) (17, 18), which in turn binds to the tail-anchored fission protein 1 (Fis1) protein (19). Fluorescence microscopy studies show that Mdv1 colocalizes with Dnm1 at sites of mitochondrial fission (20). In vitro, Mdv1 interacts with the GTP-bound form of Dnm1 and stimulates Dnm1 self-assembly (21).

Fis1 is conserved in humans (hFis1) but does not appear to recruit Drp1 to mitochondria. Instead, Drp1 recruitment is mediated by mitochondrial fission factor (Mff), another tail-anchored protein (22, 23). Two additional human proteins, the orthologs mitochondrial dynamics proteins 49 and 51 (MiD49 and MiD51), are N-terminally anchored in the OMM and also play a role in Drp1 recruitment (24, 25). Neither Mff nor the MiD proteins is related by sequence or predicted secondary structure to Mdv1. The Mff and MiD49/51 proteins form rings surrounding mitochondria, suggesting that they coassemble with Drp1 (24), but their specific roles in Drp1 assembly and membrane scission are not well understood. Thus, major questions—whether adaptor proteins participate in lipid remodeling and membrane scission and whether they act independently or in concert in vivo—remain unanswered.

Here we use a yeast strain devoid of fission proteins to identify the minimal combination of DRPs and adaptors sufficient for mitochondrial fission. We provide evidence that Fis1 is dispensable for mitochondrial membrane scission. We also demonstrate that Mdv1, Mff, and MiDs paired individually with their respective DRPs are interchangeable, in that each is sufficient to catalyze fission. Importantly, coassembly of an MiD protein with Drp1 dramatically decreases the diameter of the Drp1 structures formed. This result provides a direct demonstration that an adaptor protein can alter the architecture of a DRP assembly in a manner that could facilitate their membrane constriction and severing ability.

Results

Requirements of Individual Yeast Proteins for Mitochondrial Fission. In WT yeast, opposing fission and fusion events maintain branched mitochondrial tubules positioned at the cell cortex (Fig. S1*A*, WT). When fission is disrupted, fusion continues unopposed, and cells contain mitochondrial nets or a single, interconnected mitochondrion, which often collapses to one side of the cell (Fig. S1*A*, mutant) (10, 12). To determine the minimal protein requirements for fission, we generated a yeast "tester" strain lacking Dnm1, the

Significance

Mitochondrial fission is critical for mammalian cell division, mitophagy, and development. Fission initiates via recruitment of dynamin-related GTPases to the mitochondrial surface. In yeast and human, the recruitment utilizes adaptors that differ in sequence and predicted structure. Key unresolved issues are whether these adaptors function independently in membrane recruitment and whether a single adaptor and GTPase are sufficient to catalyze scission. We show that three human adaptors work interchangeably with a single mitochondrial dynamin to accomplish fission. We also show that an adaptor alters the architecture of the dynamin polymer in a manner that could facilitate membrane constriction and severing.

Author contributions: S.K., Q.G., R.K., H.T.B., A.F., and J.M.S. designed research; S.K., Q.G., R.K., H.T.B., and D.M.E. performed research; D.M.E. contributed new reagents/analytic tools; S.K., Q.G., R.K., H.T.B., D.M.E., A.F., and J.M.S. analyzed data; and S.K., Q.G., R.K., H.T.B., A.F., and J.M.S. wrote the paper.

The authors declare no conflict of interest.

*This Direct Submission article had a prearranged editor.

[1]Q.G. and R.K. contributed equally to this work.

[2]To whom correspondence may be addressed. E-mail: frost@biochem.utah.edu or shaw@biochem.utah.edu.

This article contains supporting information online at www.pnas.org/lookup/suppl/doi:10.1073/pnas.1300855110/-/DCSupplemental.

Mdv1 adaptor, and Fis1. This strain also lacked a paralog of the Mdv1 adaptor, carbon catabolite repression associated factor 4 (Caf4), which was shown previously to be dispensable for fission in vivo (26). This tester strain was viable but exhibited severe mitochondrial fission defects (Table S1 and Fig. S1*A*). Expression of WT Dnm1 or of Dnm1 tethered to the outer mitochondrial membrane by its N or C terminus was unable to rescue mitochondrial fission defects in the tester strain (Table S1). Previous studies showed that pairwise combinations of cytoplasmic Dnm1 expressed with either WT Fis1 or Mdv1 also failed to rescue mitochondrial morphology (18, 19).

To determine whether Fis1 was necessary for post–Dnm1-recruitment steps in fission, we expressed combinations of WT Dnm1 together with WT or mitochondrial membrane-tethered Mdv1 in the tester strain. Mdv1 contains three domains, an N-terminal extension (NTE) that binds Fis1 (27), a middle domain that dimerizes Mdv1 via an antiparallel coiled-coil (CC) (28), and a predicted β-propeller domain (β) that interacts with Dnm1 (27, 29) (Fig. 1*A*). Full-length and truncated forms of Mdv1 were tethered to the outer mitochondrial membrane by the translocase of outer membrane (Tom20) anchor (labeled T20, Fig. 1*A*). Immunoblotting of whole-cell extracts confirmed that all proteins were expressed stably in vivo (Fig. S1 *B* and *C*). Mitochondrial morphology then was quantified to assess the ability of different protein combinations to restore WT mitochondrial fission and morphology. Normal mitochondrial morphology was restored in 80% of the cells by expressing cytoplasmic Dnm1 together with WT Mdv1 and Fis1 (Fig. 1*B*). Surprisingly, although WT mitochondrial morphology was restored in strains expressing Dnm1 plus all three tethered forms of Mdv1, the full-length construct was not the most efficient. The lack of an Fis1-binding partner for the NTE domain in the full-length Mdv1 construct may affect the conformation of the protein and be responsible for this effect. Consistent with this idea, the most efficient rescue occurred upon expression of the tethered Mdv1 CC plus β-propeller domain (lacking the NTE domain) (Fig. 1*B*). The mitochondrial morphology rescue observed in these studies suggests that soluble Dnm1 and tethered forms of Mdv1 are sufficient to catalyze fission in the absence of Fis1.

Fis1 Is Not Essential for Dnm1 Assembly into Fission Complexes or Membrane Scission. When cells lack Mdv1 and Fis1, GFP-Dnm1 cannot be recruited to mitochondria and instead remains in the cytoplasm (Fig. 2 *A* and *B*). When WT Mdv1 and Fis1 are present, GFP-Dnm1 assembles into punctate fission complexes distributed evenly along mitochondrial tubules (Fig. 2 *A* and *B*). Consistent with their ability to rescue fission defects, all three forms of tethered Mdv1 were able to recruit GFP-Dnm1 to mitochondria in the absence of Fis1 (Fig. 2 *A* and *B*). The percentage of cells in the population containing GFP-Dnm1 complexes (Fig. 2*B*) and the number of complexes per cell (Fig. 2*C*) were similar to that observed in WT although fission complexes formed by two of the tethered Mdv1 proteins (T20-Mdv1 and T20-β) were less functional than Mdv1 T20-CC-β (Fig. 1*B*).

In vivo, yeast mitochondrial fission and fusion are coordinated, each process occurring approximately once every 2 min (30). Although the molecular basis of this coordination is unknown, the balance is critical for robust mitochondrial function (31). Quantification of fission and fusion events in time-lapse imaging studies confirmed that these processes were balanced in our WT yeast strain (Fig. 3*A*). We next determined whether the balance of fission and fusion was altered when fission occurred without Fis1 in the tester strain. When cells expressed only cytoplasmic Dnm1, unopposed fusion formed interconnected mitochondria

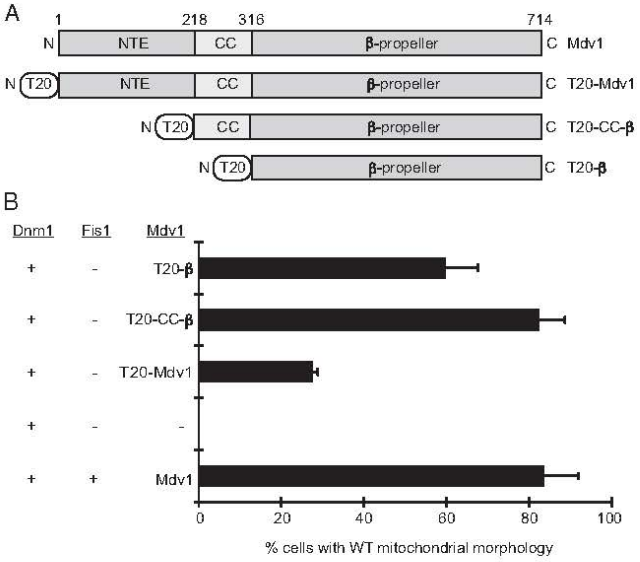

Fig. 1. Fis1 is dispensable for mitochondrial fission. (*A*) Domain structure of WT Mdv1 and Mdv1 constructs fused to the N-terminal transmembrane anchor of yeast T20. NTE, CC, and predicted β domains are shown. (*B*) Quantification of mitochondrial morphology in cells expressing the indicated fission proteins. All values are mean ± SEM; $n > 300$. Representative images of WT and fission mutant mitochondria scored are shown in Fig. S1. JSY strains 8614, 9234, 9801, 9802, and 9803 were used.

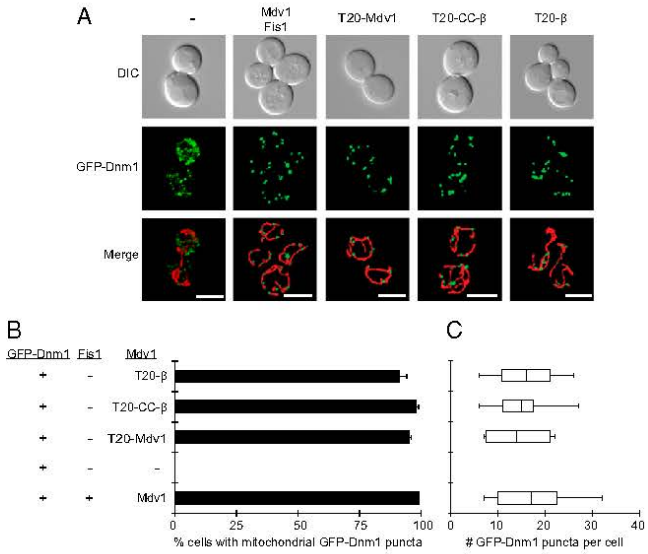

Fig. 2. Dnm1 fission complexes assemble on mitochondria in the absence of Fis1. (*A*) Representative images of GFP-Dnm1 puncta on mitochondria. Differential interference contrast (DIC), GFP-Dnm1, and merged mito-RFP (mitochondrial matrix-targeted dsRed) images are shown. (Scale bar, 5 μm.) (*B*) Quantification of the number of cells in a population containing punctate GFP-Dnm1 fission complexes on mitochondria. All values are mean ± SEM; $n > 300$. (*C*) Box-and-whisker plots showing the number of mitochondrial GFP-Dnm1 puncta per cell in the indicated strains. $n > 10$ cells. The *y* axes for B and C are the same. JSY strains 9493, 9548, 9804, 9805, and 9806 were used.

with few or no free tips. As a consequence, once the system achieved steady state, neither fission nor fusion was observed (Fig. 3*A*). Similar results were obtained for the strain expressing WT Dnm1 and Mdv1 in the absence of Fis1. In contrast, when cells expressed cytoplasmic Dnm1 and tethered forms of Mdv1, fission and fusion events again were balanced, although the number of fission and fusion events was reduced (Fig. 3*A*), most likely because the tethered proteins were less functional than WT (Fig. 1*B*). Representative images of fission and fusion events in these cells are shown in Fig. 3*B*. Together, our results demonstrate that after Mdv1 and Dnm1 are recruited to the mitochondrial surface, Fis1 is not essential for the assembly of functional fission complexes and the subsequent membrane scission event. Moreover, a balance between fission and fusion is achieved in these strains.

Mff or MiDs Are Sufficient to Recruit Human Drp1 to Mitochondria and Catalyze Fission. The hFis1, Mff, and MiD49/51 adaptors are all expressed in mammalian cells. As a consequence, it has been difficult to determine definitively whether these adaptors work individually or in concert to influence fission complex assembly or mitochondrial division after Drp1 membrane recruitment. To address this issue, we individually expressed OMM-tethered forms of each adaptor protein with soluble Drp1 (variant 3, NCBI reference sequence number NP_005681.2) in the yeast tester strain. To maintain their appropriate membrane topologies, the cytoplasmic domains of hFis1 and Mff were targeted using the yeast C-terminal Fis1 anchor (yTM), and the MiD proteins were targeted using the yeast N-terminal T20 anchor (Fig. 4*A*). These mammalian proteins were expressed stably in yeast (Fig. S1 *D–H*).

In the absence of Drp1, expression of any of the three tethered forms shown in Fig. 4*A* did not rescue fission defects (Table S1). In addition, mitochondrial fission was not rescued by expression of Drp1 alone (Table S1) or by Drp1 with tethered hFis1 (Fig. 4*B*). The latter result is consistent with a previous report that hFis1 is not essential for Drp1 recruitment in mammalian cells (23). In contrast, expression of soluble Drp1 with tethered Mff was sufficient for partial rescue of mitochondrial fission and WT mitochondrial morphology in vivo (Fig. 4*B*). Expressing tethered hFis1 in addition to Mff had little effect on this rescue. Thus, hFis1 does not appear to impact fission mediated by Drp1 and tethered Mff in this system.

We also examined mitochondrial fission rescue in a tester strain expressing Drp1 and MiD51 from the repressible methionine requiring (*MET25*) promoter. Before induction (Fig. 4*C*, 0 h), ~79% of the cells in the population contained collapsed mitochondria and interconnected nets characteristic of a fission defect (Fig. 4*C*, black). The remaining 21% contained WT tubular mitochondria (Fig. 4*C*, gray) because the *MET25* promoter is repressed inefficiently under these conditions and produces low levels of both Drp1 and MiD51 proteins. WT mitochondrial morphology increased to 61 and 69% after 1.5 or 3.0 h of MiD51 induction, respectively, suggesting that cytoplasmic Drp1 and tethered MiD51 are sufficient to catalyze fission in the yeast tester strain. Upon further induction (4.5–9 h), the percentage of cells containing tubular mitochondrial morphology was reduced, and the percentage of the population containing fragmented and aggregated mitochondrial membranes increased steadily from 27 to 83% (Fig. 4*C*, white). This aggregated mitochondrial phenotype also was observed when MiD49 and MiD51 were overexpressed in mammalian cells (24). Similar results were obtained when the experiment was performed with MiD49 in place of MiD51 (Fig. S1*I*).

Time-lapse imaging studies confirmed that the changes in mitochondrial morphology observed upon expression of Drp1 with Mff, MiD49, or MiD51 were caused by mitochondrial fission. In

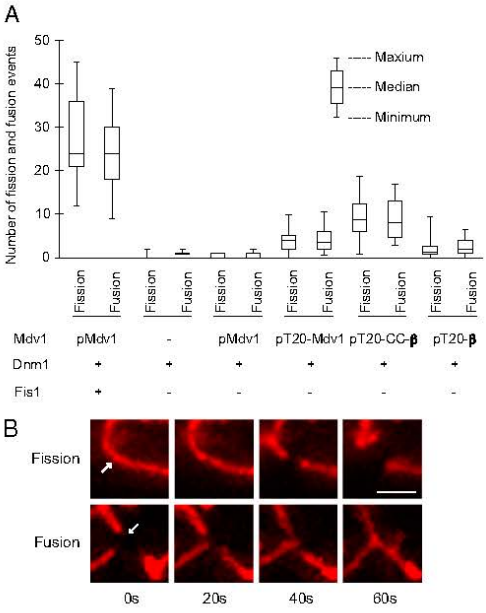

Fig. 3. Mitochondrial fission and fusion events in cells lacking Fis1. (*A*) Box-and-whisker plot showing the distribution of fission ($n > 20$ cells) and fusion ($n > 20$ cells) events in WT and strains expressing the indicated fission proteins. Total fission or fusion events per cell for a 15-min interval are indicated. (*B*) Representative mito-RFP–labeled mitochondria are shown undergoing fission (*Upper*, arrow) and fusion (*Lower*, arrow) in cells expressing Dnm1 and tethered Mdv1 (T20-β). (Scale bar, 1 μm.)

our tester strain expressing functional GFP-Drp1 and Mff, MiD49 or MiD51, green Drp1 puncta were observed on RFP-labeled mitochondrial tubules at sites where fission occurred (Fig. 4*D*). In control studies, hFis1 was not able to recruit GFP-Drp1 to mitochondria (Fig. S1*J*), as is consistent with our observation that these two proteins do not support fission (Fig. 4*B*). Together, these results establish that Drp1 is able to function with multiple adaptors to catalyze mitochondrial membrane fission.

Effect of Mff and MiD Adaptors on GTP Hydrolysis by Drp1. To determine whether mammalian adaptor proteins altered the kinetic properties of Drp1, we purified untagged versions of all three proteins (full-length Drp1 and the Mff and MiD49 cytoplasmic domains). Analytical ultracentrifugation studies are consistent with Drp1 and Mff forming homodimers, whereas MiD49 behaves as a monomer in solution (Fig. S2). As is characteristic of self-assembling GTPases in the dynamin family, Drp1 pelleted in low, but not high, ionic strength buffer in a standard sedimentation assay (Fig. 5*C*). GTP-hydrolysis by Drp1 also increased up to 15-fold in low ionic strength buffer, indicating that self-assembly stimulated GTP hydrolysis (Fig. 5*A*). Under assembly-stimulated conditions (low ionic strength, Fig. 5 *B* and *D*), the catalytic activity of Drp1 (k_{cat} = 6.5/min) was similar to that reported for the yeast mitochondrial dynamin Dnm1 (21). However, the Drp1 catalytic activity shown here is 7.6 times greater than that reported previously for a calmodulin-binding peptide (CBP)-Drp1 fusion protein (32). It is possible that the N-terminal CBP tag on Drp1 or the bacterial expression system used to purify the CBP-Drp1 fusion protein contributed to the lower activity observed in the study by Chang et al. (32). Importantly, the addition of Mff or MiD49 only modestly increased the assembly-driven GTP hydrolysis activity of Drp1 (Fig. 5 *E* and *F*). Thus, in this minimal in vitro system, these adaptors do not act as classical GTPase effectors to enhance nucleotide hydrolysis by Drp1.

MiD49 Coassembles with Drp1 and Reduces Polymer Diameter. We used negative staining transmission electron microscopy (TEM) to analyze the structures formed by Drp1 in vitro. At low temperature, apo-Drp1 (without nucleotide) did not assemble into well-ordered structures (Fig. 6*A*). When the nonhydrolyzable analog β,γ-methyleneguanosine 5′-triphosphate (GMP-PCP) was added, Drp1 assembled into rings with an average external diameter of 33.5 ± 4.1 nm (Fig. 6 *B* and *G*). Raising the temperature to 25 °C in the presence of GMP-PCP produced Drp1 spirals (34.4 ± 6.4 nm). Intrinsically, Drp1 did not bind to liposomes containing moderate concentrations of anionic lipids (e.g., 37% phosphatidyl-serine; asterisk in Fig. 6*C*). Drp1 was able to deform nonphysiological liposomes made from purely anionic lipids (e.g., 100% 1,2-dioleoyl-*sn*-glycero-3-phospho-L-serine, DOPS) in the presence of GMP-PCP at 25 °C, forming tubes with ordered striations along their length (Fig. 6*D*). Interestingly, the diameter of these Drp1 tubes was significantly smaller (64.7 ± 7.2 nm) than that reported previously for Dnm1 assembled on lipids (109–121 nm) (14, 15). Constriction of these structures occurred upon exposure to GTP (Fig. 6 *E* and *F*), generating polymers with an average diameter of 30.7 ± 4.9 nm (Fig. 6*G*).

We also analyzed the interaction of Drp1 with MiD49. In the presence of GMP-PCP, Drp1 self-assembles and pellets in a sedimentation assay (Fig. 7*A*). Although the cytoplasmic domain of MiD49 alone (MiD49$^{\Delta TM}$) remains in the supernatant fraction, the adaptor sediments in the presence of Drp1, consistent with the idea that the two proteins bind to each other and may coassemble (Fig. 7*A*). These findings were confirmed using a flotation assay (in the presence of GMP-PCP). His-tagged MiD49$^{\Delta TM}$ alone (His-MiD49$^{\Delta TM}$) was able to bind and float with liposomes containing nickel-modified lipids after centrifugation in a sucrose step gradient (Fig. 7*B*, *Upper*, lane 1). This fractionation pattern was dependent upon the presence of nickel (nickel-nitrilotriacetic acid, Ni-NTA) lipids and did not occur when membranes lacking the Ni-NTA moiety were substituted in the experiment (Fig. 7*B*, *Lower*, lane 1). Although Drp1 has a weak affinity for the Ni-NTA liposomes on its own (Fig. 7*B*, *Upper*, lane 4), the fraction of Drp1 bound to these liposomes increased visibly in the presence of the MiD49 adaptor (Fig. 7*B*, *Upper*, lane 7). In control experiments, MiD49 and Drp1 (alone or in combination) did not float with electrostatically neutral lipids (Fig. 7*B*, *Lower*, lanes 6 and 9).

Negative transmission electron microscopy staining revealed a dramatic effect of MiD49 on Drp1 polymer formation. At 25 °C in the presence of GMP-PCP, Drp1 plus MiD49 formed extended, uniform polymers with distinct striations (Fig. 7*C*, *Upper*). These polymers had an average external diameter of 14.9 ± 1.5 nm, which is less than half the diameter of ring stacks formed by Drp1 alone (34.4 ± 6.4 nm) (Fig. 6*G*). Measurement of pixel intensity along the length of these structures revealed a highly regular periodicity of ~5 nm (Fig. 7*C*, *Lower*). In control studies, MiD49 did not assemble reproducibly into similar polymers in the presence or absence of GTP or GTP analogs.

To investigate further the nature of these narrower polymers, we examined assembly in the presence of different Drp1:MiD49 (molar:molar) ratios. Incubation of Drp1 and MiD49 at a 1:1 ratio in the presence of GMP-PCP produced mainly polymers with the smaller average diameter (Fig. 7*D*, white arrowheads,14.9 ± 1.5 nm). These polymers often associated laterally into bundles. When a Drp1:MiD49 ratio of 5:1 or 10:1 was examined, fewer narrow polymers were observed (Fig. 7*D*, white

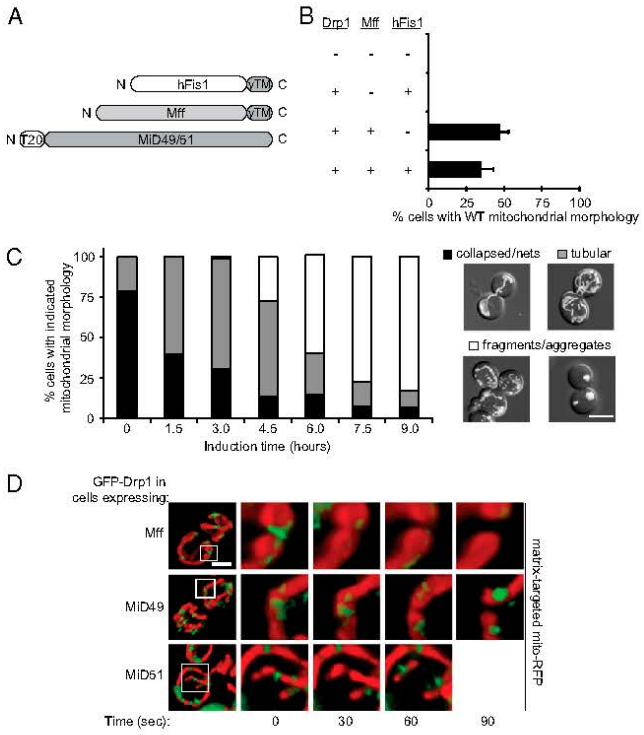

Fig. 4. Mammalian Drp1 and mitochondrial-tethered adaptor proteins rescue mitochondrial fission defects in yeast. (*A*) Domain structures of hFis1 and Mff fused to the C-terminal outer membrane anchor of yeast Fis1 (yTM). Human MiD49 or MiD51 were targeted to the mitochondrial outer membrane via fusion to the N-terminal transmembrane anchor of yeast T20. (*B*) Quantification of mitochondrial morphology in cells expressing Mff plus the indicated fission proteins and mito-OMGFP. All values are mean ± SEM; $n > 300$. (*C*) Quantification of mitochondrial morphologies observed in cells during induction of Drp1 and MiD51 from the *MET25* promoter. The merged DIC and mito-OMGFP images to the right of the graph are representative of the mitochondrial morphology categories scored. (Scale bar, 5 μm.) (*D*) Time-lapse images of GFP-Drp1 at fission sites in cells expressing Mff (*Top*), MiD49 (*Middle*), or MiD51 (*Bottom*). Boxed regions mark fission sites imaged at 30-s intervals in each row. (Scale bar, 2 μm.)

arrowheads), with a concomitant increase in polymers of larger diameter (black arrowheads). Both the appearance and the diameter of the latter spirals were similar to those formed by Drp1 alone (Fig. 6*C*). These data are consistent with the idea that coassembly of MiD49 with Drp1 is stoichiometric and suggest that MiD49 copolymerizes with Drp1 rather than simply nucleating assembly of a Drp1 homopolymer.

Discussion

The adaptor proteins studied here were shown originally to mediate the recruitment of the Dnm1 or Drp1 GTPases to mitochondria, but their postrecruitment roles in mitochondrial fission were not clear. In this study, we demonstrate that individual adaptor-GTPase pairs act after recruitment to catalyze membrane division in vivo. In the case of Drp1, coassembly with one of these adaptors increases the order and dramatically decreases the diameter of the polymers formed.

The identification of Fis1 and Dnm1/Drp1 in yeast and mammals initially suggested that the basic molecular machinery for mitochondrial fission was conserved during evolution. Although the role of yeast Fis1 in Mdv1-Dnm1 recruitment to mitochondria has never been questioned, data supporting a function for mammalian Fis1 in Drp1 recruitment was contradictory. This issue was resolved recently by the demonstration that it is human Mff, rather than Fis1, that acts as the mitochondrial receptor for Drp1 (23). Soon after, MiD49 and MiD51 also were reported to mediate Drp1 mitochondrial recruitment (24, 25). We show here that yeast Fis1 is dispensable for fission when the Mdv1 adaptor is membrane-tethered, allowing Dnm1 recruitment to mitochondria. Moreover, expression of human Fis1 and Drp1 in yeast was not sufficient to rescue defects in mitochondrial fission. Thus, Fis1 has not been conserved throughout evolution because of an essential role in Dnm1/Drp1-mediated membrane scission. What, then, is the conserved function of Fis1? Although mitochondrial fission proteins also have been implicated in peroxisome division and mitophagy in yeast and mammals (33–35), Fis1 appears to be dispensable for peroxisome fission in human cells (23) and for mitophagy in yeast (36, 37). In addition, it was suggested recently that mammalian Fis1 interacts directly with MiD51 (also called mitochondrial elongation factor 1, or MIEF1) to regulate fission negatively (25). Further studies clearly are necessary to determine whether Fis1 has a conserved function(s) in organelle division.

Our findings show unambiguously that a single type of adaptor protein is sufficient for mitochondrial membrane scission by hu-

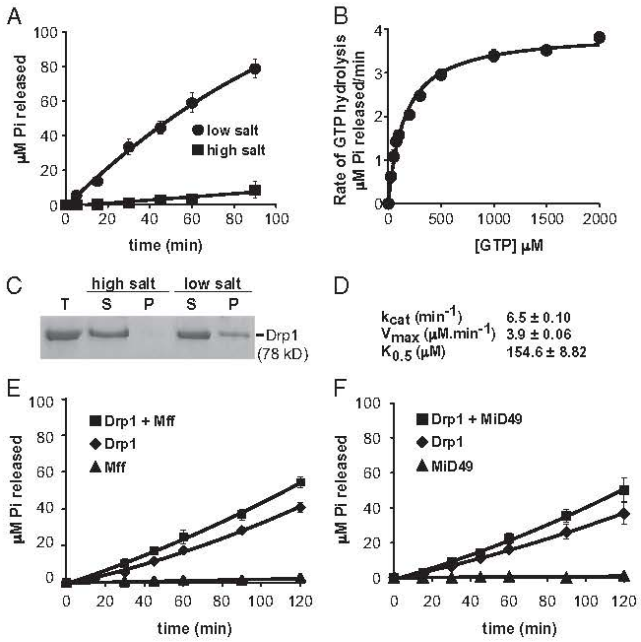

Fig. 5. Effects of Mff and MiD49 on Drp1 GTPase activity. (*A*) Time course of GTP hydrolysis by Drp1 (0.6 μM) measured in 100 μM GTP, 37 °C at high (500 mM KCl) and low (50 mM KCl) ionic strength. (*B*) Steady-state kinetics of Drp1 (0.6 μM) GTP hydrolysis measured at low ionic strength (50 mM KCl), 37 °C. (*C*) A Coomasie blue-stained gel showing velocity sedimentation of Drp1 at high and low ionic strength. P, pellet; S, supernatant; T, total. (*D*) Drp1 kinetic parameters determined as described in *B* and *Materials and Methods*. K_{cat}, turnover number; V_{max}, maximal rate of hydrolysis; $K_{0.5}$, substrate concentration at which velocity is one-half maximal. (*E* and *F*) GTP hydrolysis by Drp1 (0.1 μM) measured in 200 μM GTP and 50 mM KCl at 37 °C in the presence and absence of the indicated adaptor proteins. Cytoplasmic domains of Mff (*E*) or MiD49 (*F*) purified from yeast were included at 0.5 μM.

man Drp1. Why, then, do mammalian cells simultaneously express Mff, MiD49, and MiD51? Studies to date have not identified significant differences in the mitochondrial fission events mediated by these different adaptors (23–25). However, the assays used in these studies (morphological quantification and fixed time-point analysis) would fail to detect significant temporal, spatial, or mechanistic differences in Drp1 recruitment, assembly, and/or membrane scission that are specific to each adaptor. In addition, the physiological circumstances (i.e., apoptosis, mitophagy) in which each adaptor is activated might differ. Documented post-translational modifications of Drp1 including phosphorylation (3, 38–42), sumoylation (43–46), nitrosylation (47), and ubiquitination (48–52) also could influence the identity of the adaptor used for fission, as could posttranslational modifications of the adaptors themselves. Finally, it is possible that multiple adaptors work together with Drp1 at a single division site. Such cooperation has been documented for the paralogous adaptors Mdv1 and Caf4 in yeast (53), and it seems likely that the MiD49 and MiD51 paralogs also will prove to have the capacity to function with Drp1 at the same fission site in mammals.

Distances of ≤1 nm between opposing lipid bilayers are thought to be necessary for initiation of inner leaflet hemifusion and subsequent membrane scission (54, 55). Taking into account the diameter of a lipid bilayer (~5 nm) (56, 57) and mitochondria's double membrane, the average external diameter we measured for Drp1-lipid tubules (30.7 nm) (Fig. 6*G*) would not produce a luminal distance small enough to initiate fission of both the inner and outer mitochondrial membranes. This problem could be overcome by coassembling MiD49 with Drp1, because the ~15-nm average external diameter of the Drp1:MiD49 copolymer is sufficiently narrow to drive fission. Like the copolymers formed by coincubation of dynamin-1 with endophilin (58) or amphiphysin (59), the MiD49:Drp1 copolymers shown here also change the structural properties of a dynamin GTPase polymer. In the case of N-BAR (Bin–Amphiphysin–Rvs domain with an additional predicted N-terminal amphipathic helix) proteins and dynamin-1, the hybrid coat has a different diameter and different pitch. A detailed understanding of how MiD49 alters structural features of the Drp1 polymer and the functional consequences of the hybrid assembly for the fission process requires further study.

Our findings clarify the individual functions of mitochondrial adaptors and challenge the notion that these proteins act solely to recruit and stimulate assembly of the DRPs Dnm1 and Drp1 on the correct cellular membrane. Instead, coassembly of adaptors with DRPs may work generally to change the physical properties of the resulting polymers in a manner that promotes or regulates membrane scission. For example, coassembly could prevent promiscuous fission by altering contacts between adjacent turns of the DRP helix, thereby inhibiting mechano-chemical conformational changes that lead to constriction and fission. Such an inhibited state may be regulatory, delaying constriction until a signaling event or another factor is recruited. Alternatively, as shown here, the copolymer may have different geometric properties and be able to form a more compact state that promotes membrane

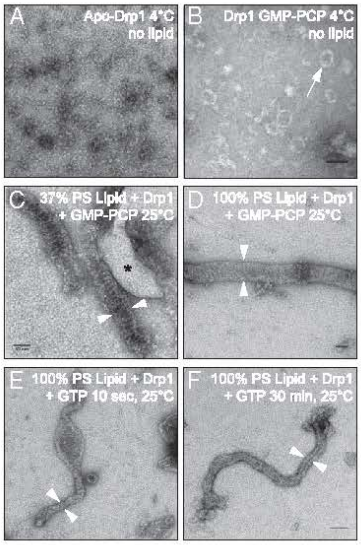

G

Structure	External diameter (nm)
Drp1 rings	33.5 +/- 4.1
Drp1 ring stacks	34.4 +/- 6.4
DOPS + Drp1 + GMP-PCP	64.7 +/- 7.2
DOPS + Drp1 + GTP	30.7 +/- 4.9

Fig. 6. Drp1 self-assembly induces lipid tubulation and constriction in vitro. (*A–F*) Transmission electron micrographs of negatively stained Drp1 assemblies. (*A*) Drp1 protomers do not assemble in the absence of nucleotide at 4 °C. (*B*) Drp1 assembles into limited rings in the presence of GMP-PCP at low temperature (white arrow). (*C*) At 25 °C, Drp1 forms spirals or stacks of rings in the presence of GMP-PCP that exclude liposomes containing molar 37% PS (asterisk). (*D*) Drp1 assembles around liposomes containing molar 100% PS in the presence of GMP-PCP at 25 °C. (*E* and *F*) Drp1-decorated lipid tubes assembled in the presence of GMP-PCP were imaged after treatment with 1 mM GTP for 10 s (*E*) or 30 min (*F*). (*G*) Average external diameters of Drp1 structures as indicated by white arrowheads in *C–F*. For all measurements, $n = 50$. (Scale bars, 50 nm.)

constriction and fission. Regardless of the mechanism, we suggest that the ability to modulate polymer geometry will prove to be a common function of mitochondrial dynamin adaptors.

Materials and Methods

Strains and Plasmids. Yeast strains and plasmids used in this study are listed in Tables S2 and S3. Standard yeast and bacterial techniques were used for construction and growth of strains (60, 61). Details of plasmid construction can be found in *SI Materials and Methods*.

Fluorescence Microscopy. Mitochondrial morphologies were quantified as described previously (28, 62, 63) in the indicated strains expressing mitochondrial-matrix–targeted fast-folding RFP (mito-ffRFP also referred to as "mito-RFP") or OMM-targeted GFP (mito-OMGFP; Fig. 4). Unless noted in the text, Mdv1, Mff, and MiD49/51 proteins were expressed from the *MET25* promoter and integrated at the *MDV1* locus. Dnm1 and GFP-Dnm1 were expressed from the native promoter and locus. Drp1 (variant 3) and GFP-Drp1 were expressed from the *MET25* and copper homeostasis 1 (*CUP1*) promoters, respectively, on pRS416.

Overnight cultures were grown at 30 °C in the appropriate selective synthetic dextrose medium containing 100 μg/mL methionine, were diluted to 0.2 OD_{600} in medium containing 10 μg/mL methionine, and were grown for 3–5 h. For Fig. 4*C*, cells were grown as described above but were diluted continually into synthetic dextrose medium lacking methionine (to maintain an OD_{600} between 0.2 and 1.0) and were scored at the indicated times. Mitochondrial phenotypes and formation of GFP-Dnm1 puncta were scored in 100 cells, and the data shown represent the average ± SEM of at least three independent experiments. Images were acquired and processed as described (28).

Time-Lapse Imaging. For single-color time-lapse imaging (Fig. 3), cells expressing mito-RFP were grown in selective synthetic dextrose medium were applied to Lab-Tek II Chamber wells (Thermo Scientific) treated with Concavalin A (2 mg/mL; Sigma) and were maintained at 30 °C. Z stacks (0.2-μm optical sections) of fields of cells were acquired every 7 s over a 20-min time course using a 3i Marianas Live Cell Imaging microscope workstation (Intelligent Imaging Innovations) equipped with dual ultra-sensitive Cascade II 512B EMCCD cameras (Roper Scientific) configured with a Roper Dual-cam and Sutter DG-4 Illuminator (Sutter Instruments) with a 100×, 1.45 NA Plan-Apochromat objective (Zeiss). Data were deconvolved and analyzed using SlideBook 4.2 software (Intelligent Imaging Innovations). Substacks containing fission events were isolated from the entire stack to minimize signal background and were assembled in Photoshop CS3 (Adobe). Brightness and contrast were adjusted using only linear operations applied to the entire image. For quantification, only cells that underwent one or more fission or fusion events during the time course were selected for analysis. The results were expressed as the number of fission or fusion events per cell during a 15-min interval.

For two-color time-lapse imaging (Fig. 4*D*), cells expressing GFP-Drp1, mito-RFP, and the indicated mammalian adaptor (MiD49, MiD51, or Mff) were grown in selective synthetic dextrose medium and applied to a Y04c microfluidic chamber (CellASIC Corp.). Injection of cells and medium was controlled by an ONIX Microfluidic Perfusion System and ONIX FG version 2.6 software (CellASIC Corp.). Z stacks of cells (0.3-μm optical sections) were imaged every 30 s over a 30-min time course using an Observer Z1 microscope (Zeiss) equipped with HE GFP (set 38) and mRFP (set 63) shift-free filter sets, an Axiocam MRm Rev.3 camera, and a 100×, 1.4 NA Plan-Apochromat objective (Zeiss). GFP and DsRed channels were acquired sequentially using AxioVision 4.8 software (Zeiss), and data were deconvolved and analyzed using AxioVision 4.6 software (Zeiss). Substacks containing fission events were isolated and assembled as described above.

Protein Production. Human Drp1 (isoform 3; NP_005681.2), MiD49 (accession number Q96C03), and Mff (accession number Q9GZY8) constructs, each containing an N-terminal PreScission protease cleavage site and a FLAG-One-STrEP tag (IBA), were expressed in JSY9612. Overnight cultures were diluted into selective synthetic dextrose medium containing 1 mM $CuSO_4$ to induce expression (final OD_{600} of 0.2) and were grown in a Belco fermentor at 30 °C for 24 h. After harvesting, cell pellets were snap frozen in liquid nitrogen as small droplets and were pulverized in a freezer mill (3 min × 15 cycles). All subsequent purification steps were performed at 4 °C. Cell powders were dissolved in either high ionic strength lysis buffer for hDrp1 [100 mM Tris-Cl (pH 8.0), 500 mM NaCl, 1 mM DTT, 1 mM EDTA] or low ionic strength buffer for MiD49 or Mff [100 mM Tris-Cl (pH 8.0), 150 mM NaCl, 1 mM DTT, 1 mM EDTA] containing Protease Inhibitor Mixture III (Calbiochem). The lysates were clarified by centrifugation at 30,000 × *g* for 1 h, filtered (0.45 μm), loaded onto a 5-mL StrepTrap HP column (GE Healthcare), washed with 1 L lysis buffer, and cleaved in the column with PreScission protease (GE Healthcare) for 16 h. Drp1 was dialyzed against 20 mM Hepes (pH 7.4), 150 mM KCl, 2 mM $MgCl_2$, 1 mM DTT, and 0.5 mM EDTA, snap frozen in liquid nitrogen, and stored at −80 °C. Mff and MiD49 were purified further by size-exclusion chromatography (Sepharose 200; GE Healthcare), dialyzed against 20 mM Hepes (pH 7.4), 150 mM KCl, 2 mM $MgCl_2$, 1 mM DTT, and 0.5 mM EDTA, and stored at 4 °C. Equilibrium sedimentation analysis performed on purified protein indicated that Drp1 variant 3 is a dimer in high ionic strength buffer [observed molecular weight (MW_{obs})/calculated molecular weight (MW_{cal}) = 2.17], the cytoplasmic domain of Mff is a dimer (MW_{obs}/MW_{cal} = 2.25), and the cytoplasmic domain of MiD49 is a monomer (MW_{obs}/MW_{cal} = 0.99) (Fig. S2).

GTPase Assay. Inorganic phosphate release was measured using the malachite green phosphate assay (POMG-25H; BioAssay Systems) as described by the manufacturer and by Leonard et al. (64). For the time-course analysis, Drp1 (0.6 μM) was assayed at 37 °C in high (500 mM KCl) or low (50 mM KCl) ionic strength buffer containing 20 mM Hepes (pH 7.4), 2 mM $MgCl_2$, 1 mM DTT, and 100 μM GTP. Reactions were halted at the indicated times by diluting 20 μL in 25 mM EDTA (final concentration) in a microtiter plate. Although 25 mM EDTA was sufficient to halt the reaction, we found that higher EDTA

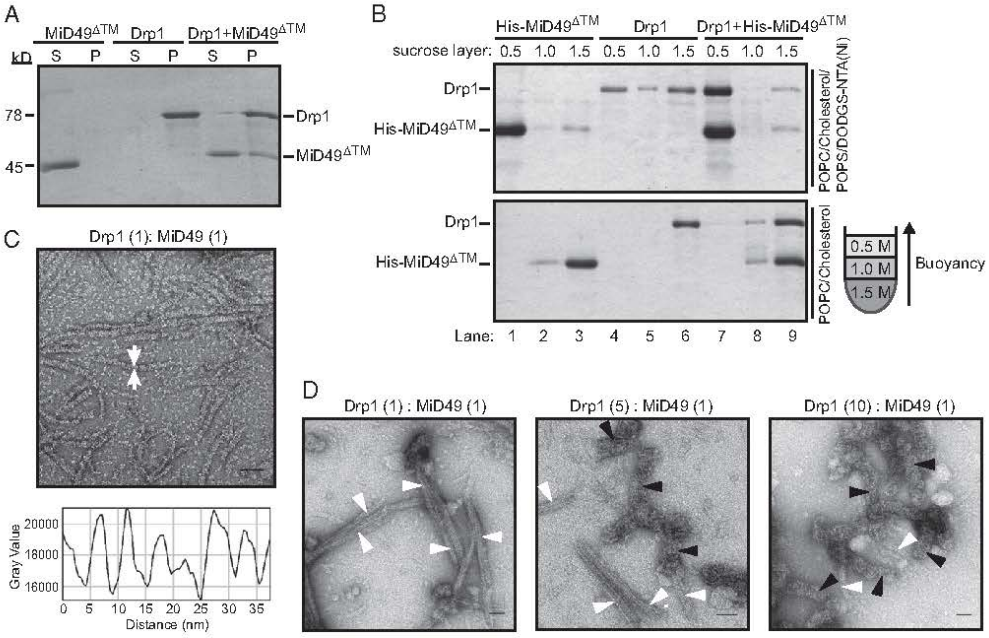

Fig. 7. MiD49 copolymerizes with Drp1 and decreases polymer diameter. (*A*) MiD49$^{\Delta TM}$ (lacking the transmembrane domain) cosediments with Drp1. (*B*) liposomes containing DO DGS-NTA(Ni) (*Upper*) decorated with His-tagged MiD49$^{\Delta TM}$ promote flotation of Drp1 in a sucrose step gradient. Charge-neutral POPC/cholesterol liposomes (*Lower*) bind His-tagged MiD49$^{\Delta TM}$ poorly and do not promote Drp1 flotation. As depicted in the cartoon gradient at the right, protein-bound liposomes float to the top of the 0.5 M sucrose layer. (*C*) (*Upper*) In the presence of MiD49$^{\Delta TM}$, Drp1 forms ordered polymers (arrows) with a diameter of 14.9 ± 1.5 nm. (*Lower*) Periodicity (~5 nm) measured along the length of the Drp1:MiD49 polymers. (*D*) Effect of Drp1:MiD49 (molar:molar) ratios on polymer assembly. Decreasing MiD49 concentration reduces the formation of narrow (14.9-nm) polymers (white arrowheads) and increases the diameter of larger (34.4-nm) polymers (black arrowheads).

concentrations lowered the signal generated by the malachite reagent during the development step. Samples were incubated at room temperature with 20 μL Malachite Reagent (BioAssay Systems) and 60 μL water for 30 min, and the absorbance at 600 nm was measured using a Modulus Microplate Reader (Turner BioSystems). For the steady-state kinetic analysis, GTP assays were performed at 37 °C in reactions containing 0.6 μM Drp1, 20 mM Hepes (pH 7.4), 50 mM KCl, 2 mM $MgCl_2$, and 1 mM DTT containing variable GTP concentrations (0, 25, 50, 75, 100, 200, 300, 500, 1,000, 1,500, and 2,000 μM). Fixed volumes were removed every 5 min for 70 min, quenched by EDTA, and developed as described above. The k_{cat} and the substrate concentration at which velocity is one-half maximal ($k_{0.5}$) were calculated in GraphPad Prism using nonlinear regression curve fitting. For time-course analyses with adaptor proteins, GTPase assays were performed in reactions containing Drp1 (0.1 μM) plus or minus Mff (0.5 μM) or MiD49 (0.5 μM) at 37 °C in 50 μM KCl, 20 mM Hepes (pH 7.4), 2 mM $MgCl_2$, 1 mM DTT, and 200 μM GTP. In all experiments, data shown are the average ± SEM values obtained from triplicate samples analyzed at the same time. Each experiment was repeated three times.

Velocity Sedimentation and Flotation Assays. For the velocity sedimentation assay (Fig. 5*C*), 1.25 μM Drp1 was incubated in either low ionic strength buffer [20 mM Hepes (pH 7.4), 50 mM KCl, 2 mM $MgCl_2$, 1 mM DTT] or high ionic strength buffer [20 mM Hepes (pH 7.4), 500 mM KCl, 2 mM $MgCl_2$, 1 mM DTT] for 1 h at 37 °C. The reactions were spun down at 40,000 rpm (TLA 100 rotor) in a Beckman Optima MAX Ultracentrifuge for 1 h at 25 °C. Supernatants were removed, and pellet fractions were resuspended in an equal volume of buffer. Then 25 μL of total, supernatant, and pellet fractions were separated on 10% SDS/PAGE gels and stained with Coomassie Brilliant Blue dye. For the velocity sedimentation in Fig. 7*A*, 1.25 μM MiD49$^{\Delta TM}$, 1.25 μM Drp1, or 1.25 μM of both proteins was dialyzed at 25 °C into 20 mM Hepes (pH 7.4), 25 mM KCl, 2 mM $MgCl_2$, 1 mM DTT, and 200 μM GMP-PCP for 6 h. Samples were pelleted and processed for SDS/PAGE as described above.

Liposome Preparation. 1-Palmitoyl-2-oleoyl-*sn*-glycero-3-phosphocholine (POPC), 1-palmitoyl-2-oleoyl-*sn*-glycero-3-phospho-L-serine (POPS), cholesterol, 1,2-dipalmitoyl-*sn*-glycero-3-phosphoethanolamine-N-(lissamine rhodamine B sulfonyl) (Rhodamine-PE; ammonium salt), 1,2-dioleoyl-*sn*-glycero-3-[(*N*-(5-amino-1-carboxypentyl)iminodiacetic acid)succinyl] (nickel salt; Ni^{2+}-NTA-DOGS), and DOPS were purchased from Avanti Polar Lipids in chloroform. Four types of mixtures were prepared: (*i*) POPC, POPS, cholesterol, Rhodamine-PE were mixed in a molar ratio 44.4:37:18.5:0.007 [37% phosphatidylserine (PS) liposomes; Fig. 6*C*]; (*ii*) POPC, POPS, cholesterol, and Ni^{2+}-NTA-DOGS were mixed in a molar ratio 44.4:31:18.5:6 (nickel liposomes); (*iii*) 100% DOPS (100% PS liposomes; Fig. 6 *D–F*); and (*iv*) POPC:cholesterol were mixed in a molar ratio 80:20 (neutral liposomes). For formulation 3 (100% PS), we used the dioleoyl form of phosphatidyl-serine to preserve fluidity and solubility of the liposomes.

Chloroform was evaporated by gentle vortexing under a steady stream of nitrogen gas to make a thin lipid film around the walls of glass vials. These films were dried under vacuum for 1 h at room temperature. Dried lipid films then were resolubilized in absolute hexane. The hexane also was evaporated under streaming nitrogen while vortexing, followed by a second round of desiccation for 3–4 h at room temperature. Lipid films were suspended in aqueous buffer [20 mM Hepes (pH 7.5), 100 mM KCl] by vortexing at room temperature. Aliquots from the liposome preparation were stored at −80 °C.

Flotation Assays. Liposomes and proteins were mixed in a molar ratio of 1,000:1 (lipid:protein) in Beckman polycarbonate centrifuge tubes. After 1-h

incubation at 4 °C, the mixtures were homogenized with 300 μL 2 M sucrose in 20 mM Hepes (pH7.5), 100 mM KCl, 1 mM GMP-PCP (~1.5-M final sucrose concentration). Two additional layers of 1 M (150 μL) and 0.5 M (300 μL) sucrose in the same buffer were overlaid carefully (in that order) on top of the homogenized mixture. The mixtures were spun using a TLS-55 rotor in a Beckman centrifuge for 1 h at 54,000 rpm (4 °C). After the spin, the liposomes migrated to interfaces between individual sucrose layers and could be seen as turbid bands. The interfaces between individual sucrose layers were collected by pipetting and analyzed by 10% SDS/PAGE and Coomassie Brilliant Blue staining.

In Vitro Membrane Binding and Tubulation Reactions. For Drp1 tubulation reactions, DOPS liposomes were mixed with protein (1:1, mass:mass). After 1 h, GMP-PCP was added, and the sample was incubated for 4 h at room temperature. The effects of GTP hydrolysis were analyzed in two ways. First, after adsorption of the lipid and protein mixtures to EM grids, the sample was washed in 1 mM GTP followed immediately by blotting and staining. Second, a stock of 10 mM GTP was added to lipid-protein mixtures to a final concentration of 1 mM GTP for 30 min before the mixtures were applied to EM grids for staining.

For Drp1-MiD49 copolymerization, proteins were mixed 1:1 (mass:mass) with or without liposomes and were dialyzed overnight against 20 mM Hepes, 25 mM KCl, 200 mM GMP-PCP, 2 mM $MgCl_2$, and 1 mM DTT.

EM. For negative-stain EM, carbon-coated copper grids were glow discharged for 15 s. Then 5 μL of the sample was added to the surface, blotted, and stained with 1% uranyl acetate. Images were acquired using an FEI Tecnai T12 electron microscope equipped with a LaB_6 filament and operated at 120 kV. Magnifications of 21,000–42,000× were recorded on a Gatan CCD.

ACKNOWLEDGMENTS. We thank J. Macfarlane and S. Safran for cloning expertise and assistance with GTPase assays; M. Ryan and A. van der Bliek for providing MiD and Mff plasmids; J. M. McCaffery for use of the John Hopkins University Integrated Imaging Facility; and M. Kay, T. Formosa, and members of the J.M.S. and A.F. laboratories for stimulating discussions. This work was supported by National Institutes of Health (NIH) Grants GM53466 and GM84970 (to J.M.S.). D.M.E. and the University of Utah Protein Interaction Core Facility are supported by NIH Grant GM82545.

1. Praefcke GJ, McMahon HT (2004) The dynamin superfamily: Universal membrane tubulation and fission molecules? *Nat Rev Mol Cell Biol* 5(2):133–147.
2. Gorsich SW, Shaw JM (2004) Importance of mitochondrial dynamics during meiosis and sporulation. *Mol Biol Cell* 15(10):4369–4381.
3. Taguchi N, Ishihara N, Jofuku A, Oka T, Mihara K (2007) Mitotic phosphorylation of dynamin-related GTPase Drp1 participates in mitochondrial fission. *J Biol Chem* 282(15):11521–11529.
4. Parone PA, et al. (2008) Preventing mitochondrial fission impairs mitochondrial function and leads to loss of mitochondrial DNA. *PLoS ONE* 3(9):e3257.
5. Twig G, et al. (2008) Fission and selective fusion govern mitochondrial segregation and elimination by autophagy. *EMBO J* 27(2):433–446.
6. Gomes LC, Di Benedetto G, Scorrano L (2011) During autophagy mitochondria elongate, are spared from degradation and sustain cell viability. *Nat Cell Biol* 13(5):589–598.
7. Rambold AS, Kostelecky B, Elia N, Lippincott-Schwartz J (2011) Tubular network formation protects mitochondria from autophagosomal degradation during nutrient starvation. *Proc Natl Acad Sci USA* 108(25):10190–10195.
8. Ishihara N, et al. (2009) Mitochondrial fission factor Drp1 is essential for embryonic development and synapse formation in mice. *Nat Cell Biol* 11(8):958–966.
9. Wakabayashi J, et al. (2009) The dynamin-related GTPase Drp1 is required for embryonic and brain development in mice. *J Cell Biol* 186(6):805–816.
10. Bleazard W, et al. (1999) The dynamin-related GTPase Dnm1 regulates mitochondrial fission in yeast. *Nat Cell Biol* 1(5):298–304.
11. Labrousse AM, Zappaterra MD, Rube DA, van der Bliek AM (1999) C. elegans dynamin-related protein DRP-1 controls severing of the mitochondrial outer membrane. *Mol Cell* 4(5):815–826.
12. Otsuga D, et al. (1998) The dynamin-related GTPase, Dnm1p, controls mitochondrial morphology in yeast. *J Cell Biol* 143(2):333–349.
13. Sesaki H, Jensen RE (1999) Division versus fusion: Dnm1p and Fzo1p antagonistically regulate mitochondrial shape. *J Cell Biol* 147(4):699–706.
14. Ingerman E, et al. (2005) Dnm1 forms spirals that are structurally tailored to fit mitochondria. *J Cell Biol* 170(7):1021–1027.
15. Mears JA, et al. (2011) Conformational changes in Dnm1 support a contractile mechanism for mitochondrial fission. *Nat Struct Mol Biol* 18(1):20–26.
16. Friedman JR, et al. (2011) ER tubules mark sites of mitochondrial division. *Science* 334(6054):358–362.
17. Cerveny KL, McCaffery JM, Jensen RE (2001) Division of mitochondria requires a novel DMN1-interacting protein, Net2p. *Mol Biol Cell* 12(2):309–321.
18. Tieu Q, Nunnari J (2000) Mdv1p is a WD repeat protein that interacts with the dynamin-related GTPase, Dnm1p, to trigger mitochondrial division. *J Cell Biol* 151(2):353–366.
19. Mozdy AD, McCaffery JM, Shaw JM (2000) Dnm1p GTPase-mediated mitochondrial fission is a multi-step process requiring the novel integral membrane component Fis1p. *J Cell Biol* 151(2):367–380.
20. Naylor K, et al. (2006) Mdv1 interacts with assembled dnm1 to promote mitochondrial division. *J Biol Chem* 281(4):2177–2183.
21. Lackner LL, Horner JS, Nunnari J (2009) Mechanistic analysis of a dynamin effector. *Science* 325(5942):874–877.
22. Gandre-Babbe S, van der Bliek AM (2008) The novel tail-anchored membrane protein Mff controls mitochondrial and peroxisomal fission in mammalian cells. *Mol Biol Cell* 19(6):2402–2412.
23. Otera H, et al. (2010) Mff is an essential factor for mitochondrial recruitment of Drp1 during mitochondrial fission in mammalian cells. *J Cell Biol* 191(6):1141–1158.
24. Palmer CS, et al. (2011) MiD49 and MiD51, new components of the mitochondrial fission machinery. *EMBO Rep* 12(6):565–573.
25. Zhao J, et al. (2011) Human MIEF1 recruits Drp1 to mitochondrial outer membranes and promotes mitochondrial fusion rather than fission. *EMBO J* 30(14):2762–2778.
26. Griffin EE, Graumann J, Chan DC (2005) The WD40 protein Caf4p is a component of the mitochondrial fission machinery and recruits Dnm1p to mitochondria. *J Cell Biol* 170(2):237–248.
27. Tieu Q, Okreglak V, Naylor K, Nunnari J (2002) The WD repeat protein, Mdv1p, functions as a molecular adaptor by interacting with Dnm1p and Fis1p during mitochondrial fission. *J Cell Biol* 158(3):445–452.
28. Koirala S, et al. (2010) Molecular architecture of a dynamin adaptor: Implications for assembly of mitochondrial fission complexes. *J Cell Biol* 191(6):1127–1139.
29. Cerveny KL, Jensen RE (2003) The WD-repeats of Net2p interact with Dnm1p and Fis1p to regulate division of mitochondria. *Mol Biol Cell* 14(10):4126–4139.
30. Nunnari J, et al. (1997) Mitochondrial transmission during mating in Saccharomyces cerevisiae is determined by mitochondrial fusion and fission and the intramitochondrial segregation of mitochondrial DNA. *Mol Biol Cell* 8(7):1233–1242.
31. Twig G, Shirihai OS (2011) The interplay between mitochondrial dynamics and mitophagy. *Antioxid Redox Signal* 14(10):1939–1951.
32. Chang CR, et al. (2010) A lethal de novo mutation in the middle domain of the dynamin-related GTPase Drp1 impairs higher order assembly and mitochondrial division. *J Biol Chem* 285(42):32494–32503.
33. Koch A, et al. (2003) Dynamin-like protein 1 is involved in peroxisomal fission. *J Biol Chem* 278(10):8597–8605.
34. Kuravi K, et al. (2006) Dynamin-related proteins Vps1p and Dnm1p control peroxisome abundance in Saccharomyces cerevisiae. *J Cell Sci* 119(Pt 19):3994–4001.
35. Li X, Gould SJ (2003) The dynamin-like GTPase DLP1 is essential for peroxisome division and is recruited to peroxisomes in part by PEX11. *J Biol Chem* 278(19):17012–17020.
36. Mendl N, et al. (2011) Mitophagy in yeast is independent of mitochondrial fission and requires the stress response gene WHI2. *J Cell Sci* 124(Pt 8):1339–1350.
37. Okamoto K, Kondo-Okamoto N, Ohsumi Y (2009) Mitochondria-anchored receptor Atg32 mediates degradation of mitochondria via selective autophagy. *Dev Cell* 17(1):87–97.
38. Cereghetti GM, et al. (2008) Dephosphorylation by calcineurin regulates translocation of Drp1 to mitochondria. *Proc Natl Acad Sci USA* 105(41):15803–15808.
39. Chang CR, Blackstone C (2007) Cyclic AMP-dependent protein kinase phosphorylation of Drp1 regulates its GTPase activity and mitochondrial morphology. *J Biol Chem* 282(30):21583–21587.
40. Cribbs JT, Strack S (2007) Reversible phosphorylation of Drp1 by cyclic AMP-dependent protein kinase and calcineurin regulates mitochondrial fission and cell death. *EMBO Rep* 8(10):939–944.
41. Han XJ, et al. (2008) CaM kinase I alpha-induced phosphorylation of Drp1 regulates mitochondrial morphology. *J Cell Biol* 182(3):573–585.
42. Kim H, et al. (2011) Fine-tuning of Drp1/Fis1 availability by AKAP121/Siah2 regulates mitochondrial adaptation to hypoxia. *Mol Cell* 44(4):532–544.
43. Braschi E, Zunino R, McBride HM (2009) MAPL is a new mitochondrial SUMO E3 ligase that regulates mitochondrial fission. *EMBO Rep* 10(7):748–754.
44. Figueroa-Romero C, et al. (2009) SUMOylation of the mitochondrial fission protein Drp1 occurs at multiple nonconsensus sites within the B domain and is linked to its activity cycle. *FASEB J* 23(11):3917–3927.
45. Wasiak S, Zunino R, McBride HM (2007) Bax/Bak promote sumoylation of DRP1 and its stable association with mitochondria during apoptotic cell death. *J Cell Biol* 177(3):439–450.
46. Zunino R, Braschi E, Xu L, McBride HM (2009) Translocation of SenP5 from the nucleoli to the mitochondria modulates DRP1-dependent fission during mitosis. *J Biol Chem* 284(26):17783–17795.
47. Cho DH, et al. (2009) S-nitrosylation of Drp1 mediates beta-amyloid-related mitochondrial fission and neuronal injury. *Science* 324(5923):102–105.
48. Horn SR, et al. (2011) Regulation of mitochondrial morphology by APC/CCdh1-mediated control of Drp1 stability. *Mol Biol Cell* 22(8):1207–1216.
49. Karbowski M, Neutzner A, Youle RJ (2007) The mitochondrial E3 ubiquitin ligase MARCH5 is required for Drp1 dependent mitochondrial division. *J Cell Biol* 178(1):71–84.
50. Nakamura N, Kimura Y, Tokuda M, Honda S, Hirose S (2006) MARCH-V is a novel mitofusin 2- and Drp1-binding protein able to change mitochondrial morphology. *EMBO Rep* 7(10):1019–1022.

51. Wang H, et al. (2011) Parkin ubiquitinates Drp1 for proteasome-dependent degradation: Implication of dysregulated mitochondrial dynamics in Parkinson disease. *J Biol Chem* 286(13):11649–11658.
52. Yonashiro R, et al. (2006) A novel mitochondrial ubiquitin ligase plays a critical role in mitochondrial dynamics. *EMBO J* 25(15):3618–3626.
53. Guo Q, Koirala S, Perkins EM, McCaffery JM, Shaw JM (2012) The mitochondrial fission adaptors Caf4 and Mdv1 are not functionally equivalent. *PLoS ONE* 7(12):e53523.
54. Bashkirov PV, et al. (2008) GTPase cycle of dynamin is coupled to membrane squeeze and release, leading to spontaneous fission. *Cell* 135(7):1276–1286.
55. Hernandez JM, et al. (2012) Membrane fusion intermediates via directional and full assembly of the SNARE complex. *Science* 336(6088):1581–1584.
56. Wang L, Bose PS, Sigworth FJ (2006) Using cryo-EM to measure the dipole potential of a lipid membrane. *Proc Natl Acad Sci USA* 103(49):18528–18533.
57. Leforestier A, Lemercier N, Livolant F (2012) Contribution of cryoelectron microscopy of vitreous sections to the understanding of biological membrane structure. *Proc Natl Acad Sci USA* 109(23):8959–8964.
58. Sundborger A, et al. (2011) An endophilin-dynamin complex promotes budding of clathrin-coated vesicles during synaptic vesicle recycling. *J Cell Sci* 124(Pt 1):133–143.
59. Takei K, Slepnev VI, Haucke V, De Camilli P (1999) Functional partnership between amphiphysin and dynamin in clathrin-mediated endocytosis. *Nat Cell Biol* 1(1): 33–39.
60. Green M, Sambrook J (2012) *Molecular Cloning: A Laboratory Manual* (Cold Spring Harbor Lab Press, Cold Spring Harbor, NY), 4th Ed.
61. Guthrie C, Fink G (2002) *Guide to Yeast Genetics and Molecular Biology. Methods in Enzymology* (Academic, Inc., San Diego), Vol 350.
62. Amiott EA, Cohen MM, Saint-Georges Y, Weissman AM, Shaw JM (2009) A mutation associated with CMT2A neuropathy causes defects in Fzo1 GTP hydrolysis, ubiquitylation, and protein turnover. *Mol Biol Cell* 20(23):5026–5035.
63. Bui HT, Karren MA, Bhar D, Shaw JM (2012) A novel motif in the yeast mitochondrial dynamin Dnm1 is essential for adaptor binding and membrane recruitment. *J Cell Biol* 199(4):613–622.
64. Leonard M, Song BD, Ramachandran R, Schmid SL (2005) Robust colorimetric assays for dynamin's basal and stimulated GTPase activities. *Methods Enzymol* 404:490–503.

Supporting Information

Koirala et al. 10.1073/pnas.1300855110

SI Materials and Methods

Plasmid Construction. Plasmids used in this study are listed in Table S3. Plasmids B1642, B1808, and B2053 were described previously (1). To construct B1607 and B1816, the DNA sequences encoding full-length yeast Fis1 (yFis1) and human dynamin-related protein 1 (hDrp1) isoform 3 were PCR amplified and cloned into BamHI and SalI sites of the *pRS415MET25* and *pRS416MET25* vectors (Stratagene). To create B2729, DNA sequences encoding amino acids 1–51 of yeast translocase of outer membrane (yTom20) (2) were PCR amplified and cloned into the XbaI and BamHI sites of B1808 [in-frame with the existing full-length (FL) mitochondrial division protein 1 (*MDV1*) coding region]. B2731 and B2732 were constructed by replacing BamHI-*MDV1*-SalI in B2729 with the indicated *MDV1* coding sequences. For B3090, a three-way ligation reaction was performed with the *pRS415MET25* vector (Stratagene) and PCR-amplified fragments encoding monomeric GFP^{A207K} yFis1 (amino acids 131–155) to generate the *pRS415MET25-BamHI-mOMGFP-BsiWI-yFIS1-SalI-pRS415* vector. For B3162, the StarGate cloning system (IBA) was used to introduce *PreScission Protease Cleavage Site-BamHI-hDRP1 isoform 3* DNA into the EcoRI and SalI sites of the *pYSG-IBA167* vector. For B3259, B3262, and B3294, the indicated coding sequences were exchanged for human dynamin-related protein 1 (*hDRP1*) using existing BamHI and SalI sites. For B3265, a two-step cloning protocol was used. First, the PCR-amplified copper homeostasis 1 (*CUP1*) promoter sequence was introduced into the SacII and SalI sites of the *pRS416* vector (Stratagene) to create *pRS416CUP1*. This cloning step also introduced EagI and BamHI sites upstream of the SalI site. Second, a three-way ligation reaction was performed with *pRS416CUP1* and PCR-amplified fragments encoding monomeric GFP^{A207K} and hDrp1 using EagI, BamHI, and SalI sites. B3265 contains the following order of genes and restriction sites: *pRS416 vector-SacII-CUP1-EagI-mGFP-BamHI-hDRP1-SalI-pRS416 vector*. B3357 was created by cloning PCR-amplified sequences encoding residues of human Mff (amino acids 1–198) into the EcoRI and HinDIII sites of the pMAL-c2x vector (New England BioLabs). For plasmids B2821, B2925, B2927, B2928, B3237, B3238, B3239, B3244, and B3247, a PCR fragment encoding the indicated inserts in frame with C-terminal or N-terminal 3HA were cloned into *pRS415MET25*. For B2933, a PCR fragment encoding dynamin-related protein 1 (Dnm1) was cloned into the BamHI/SalI sites of *pRS415MET25-T20*. For B2934, a PCR fragment encoding Dnm1 was cloned upstream of a fragment encoding yFis1 (amino acids 131–155) in *pRS415MET25*.

Analysis of Protein Expression. Protein expression was analyzed in whole-cell extracts prepared as described (3). For each blot in Fig. S1 *B–H*, cell equivalents were separated by SDS/PAGE and analyzed by Western blotting using anti-HA (1:1,000), anti-3 phosphoglycerate kinase (1:1,000), and anti-Dnm1 (1:1,000) primary antibodies. After incubation with the appropriate HPR-conjugated or fluorescent secondary antibodies, proteins were detected by ECL (GE Healthcare) or a fluorescent scanner (Odyssey; Li-COR Biosciences).

Analytical Equilibrium Sedimentation. The purified dynamin-related protein 1 (Drp1), mitochondrial dynamics protein 49 (MiD49), and mitochondrial fission factor (Mff) proteins were each centrifuged at a minimum of three concentrations (see the legend of Fig. S2) and two speeds 98,000 and 10,000 rpm for Drp1; 8,000, 10,000, and 12,000 rpm for MiD49; 10,000 and 12,000 rpm for Mff, using the An-50-Ti rotor, Beckman Coulter, Brea, CA) at 4 °C until equilibrium was established. Data were fit globally to an ideal single species model with a floating molecular weight using nonlinear least squares analysis as implemented in HeteroAnalysis (4). Representative data are shown for 10,000 rpm, with the MW fit and oligomeric state indicated. Buffers used for the analysis were Drp1 (20 mM Hepes 7.4, 500 mM KCl, 2 mM $MgCl_2$, 1 mM EDTA, 1 mM DTT); MiD49 (100 mM Tris·Cl 8.0, 150 mM NaCl, 1 mM EDTA, 1 mM TCEP); and Mff (50 mM sodium phosphate 7.4, 150 NaCl). Panels below each graph in Fig. S2 show the residual differences between the data and the fit. Buffer densities and protein partial specific volumes were calculated with SEDNTERP (version 1.09) (5). For Drp1, 11% of the sample was lost during centrifugation (either to self-assembly or aggregation).

1. Karren MA, Coonrod EM, Anderson TK, Shaw JM (2005) The role of Fis1p-Mdv1p interactions in mitochondrial fission complex assembly. *J Cell Biol* 171(2):291–301.
2. Ramage L, Junne T, Hahne K, Lithgow T, Schatz G (1993) Functional cooperation of mitochondrial protein import receptors in yeast. *EMBO J* 12(11):4115–4123.
3. Kushnirov VV (2000) Rapid and reliable protein extraction from yeast. *Yeast* 16(9):857–860.
4. Cole JL (2004) Analysis of heterogeneous interactions. *Methods Enzymol* 384:212–232.
5. Laue T, Shah B, Ridgeway T, Pelletier S (1992) Computer-aided interpretation of analytical sedimentation data for proteins. *Analytical Ultracentrifugation in Biochemistry and Polymer Science* (Royal Society of Chemistry, Cambridge, UK).

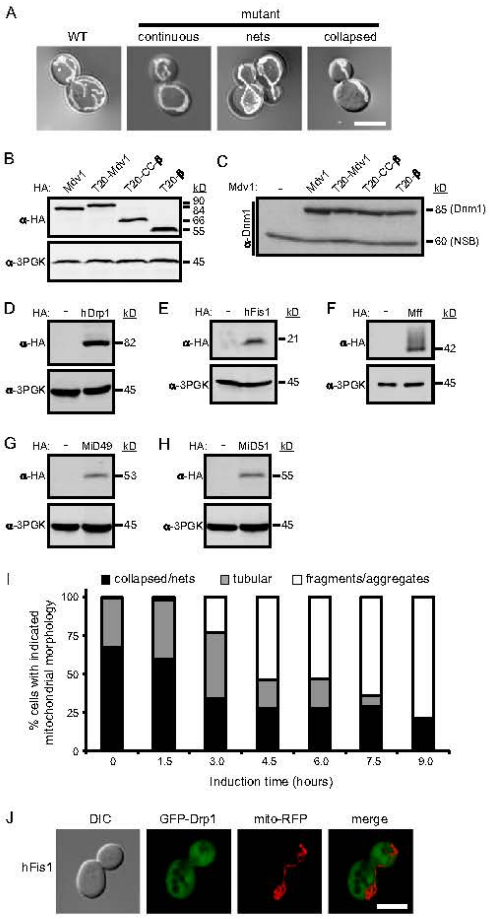

Fig. S1. Mitochondrial morphologies scored and protein expression levels for strains used in this study. (*A*) Representative images of mitochondrial morphologies scored as WT or fission mutant in this study. Superimposed differential interference contrast (DIC) and mito-RFP images are shown. (Scale bar, 5 μm.) (*B*) The steady-state abundance of C-terminal 3HA-tagged WT and tethered Mdv1 proteins was analyzed in whole-cell extracts by immunoblotting with anti-HA or anti-3PGK (loading control). (*C*) Steady-state abundance of WT Dnm1 protein expressed from the endogenous locus in strains shown in *B*. Anti-Dnm1 antibody detects Dnm1 (85 kDa) and a nonspecific band (NSB, 60-kD loading control). (*D–H*) Steady-state abundance of the indicated HA-tagged proteins expressed from the *pRS415MET25* plasmid in strain JSY9307 was analyzed in whole-cell extracts by immunoblotting with anti-HA or anti-3PGK (loading control). (*I*) Quantification of mitochondrial morphologies observed in cells during induction of Drp1 and MiD49 from the *MET25* promoter. (*J*) Representative DIC, GFP-Drp1, mito-RFP, and merged GFP/RFP images showing GFP-Drp1 localization in cells expressing hFis1 (JSY10005). (Scale bar, 5 μm.)

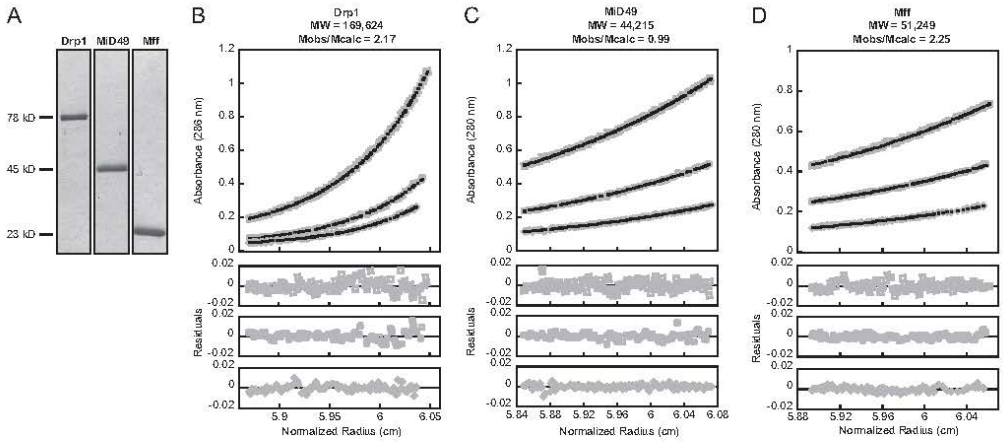

Fig. S2. Purification and analytical equilibrium sedimentation analysis of Drp1, MiD49, and Mff. (*A*) SDS/PAGE of the indicated purified proteins stained with Coomassie Brilliant Blue. (*B–D*) Analytical equilibrium sedimentation analysis of Drp1 (14.8 μM, 7.4 μM, 3.7 μM) (*B*), MiD49 (9.4 μM, 4.7 μM, 2.3 μM) (*C*), and Mff (130.0 μM, 65.1 μM, 32.6 μM) (*D*). In *B–D*, corresponding fits [observed molecular weight (MW_{obs})/calculated molecular weight (M_{calc})] are indicated above each graph, and residuals for the nonlinear least squared fits are shown below. See also *SI Materials and Methods*.

Table S1. Mitochondrial morphology in the JSY9307 tester strain expressing the indicated proteins

Protein expressed	Tubular (%)	Fission mutant (%)
None	0	100
WT Dnm1	0	100
$T20^{1\text{-}51aa}$-Dnm1	0	100
Dnm1-$Fis1^{131\text{-}155aa}$	0	100
$T20^{1\text{-}51aa}$-$Mdv1^{1\text{-}714aa}$ (FL)	0	100
$T20^{1\text{-}51aa}$-$Mdv1^{218\text{-}714aa}$ (CCWD)	0	100
$T20^{1\text{-}51aa}$-$Mdv1^{317\text{-}714aa}$ (WD)	0	100
$hFis1^{1\text{-}119aa}$-$Fis1^{131\text{-}155aa}$	0	100
$hMff^{1\text{-}198}$- $Fis1^{131\text{-}155aa}$	0	100
$T20^{1\text{-}51aa}$-$hMiD49^{48\text{-}454aa}$	0	100
$T20^{1\text{-}51aa}$-$hMiD51^{47\text{-}463aa}$	0	100
WT hDrp1	0	100

Mitochondrial morphology was visualized with mito-RFP expressed from plasmid B1642. T20 is amino acids 1-51 of Tom20 used as an N-terminal mitochondrial outer membrane anchor. Fis1 is amino acids 131-155 of yeast Fis1 used as a C-terminal mitochondrial outer membrane anchor. $n = 300$.

Table S2. Yeast strains used in this study

ID	Genotype
JSY5740	*MATa, leu2Δ1, his3Δ200, trp1Δ63, ura3-52, lys2Δ202*
JSY7459	*MATα, leu2Δ1, his3Δ200, trp1Δ63, ura3-52, fis1::HIS3, mdv1::HIS3*
JSY8614	*MATa, leu2Δ1, his3Δ200, trp1Δ63, ura3-52, caf4::KanMX*
JSY8616	*MATa, leu2Δ1, his3Δ200, trp1Δ63, ura3-52, mdv1::HIS3*
JSY9234	*MATα, leu2Δ1, his3Δ200, lys2Δ202, ura3-52, TRP1, caf4::KanMX, mdv1::URA3, fis1::HIS3*
JSY9307	*MATa, leu2Δ1, his3Δ200, trp1Δ63, ura3-52, lys2Δ202, dnm1::HIS3, fis1::HIS3, caf4::KanMX, mdv1::HIS3*
JSY9493	*MATa, leu2Δ1, his3Δ200, trp1Δ63, ura3-52, lys2Δ202, dnm1::GFP-DNM1, fis1::HIS3, mdv1::HIS3, caf4::KanMX*
JSY9548	*MATa, leu2Δ1, his3Δ200, trp1Δ63, ura3-52, lys2Δ202, dnm1::GFP-DNM1, caf4::KanMX*
JSY9612	*MATa, can1, ade2, trp1, ura3, his3, leu2, pep4::HIS3, prb1::LEU2, bar1::HISG, lys2::GAL1/10-GAL4*
JSY9801	*MATα, leu2Δ1, his3Δ200, ura3-52, lys2Δ202, fis1::HIS3, caf4::KanMX, mdv1::MET25-TOM20(1-51aa)-MDV1(1-714aa)*
JSY9802	*MATa, leu2Δ1, his3Δ200, ura3-52, lys2Δ202, fis1::HIS3, caf4::KanMX, mdv1::MET25-TOM20(1-51aa)-MDV1(218-714aa)*
JSY9803	*MATα, leu2Δ1, his3Δ200, ura3-52, lys2Δ202, fis1::HIS3, caf4::KanMX, mdv1::MET25-TOM20(1-51aa)-MDV1(317-714aa)*
JSY9804	*MATa, leu2Δ1, his3Δ200, trp1Δ63, ura3-52, lys2Δ202, fis1::HIS3, caf4::KanMX, dnm1::GFP-DNM1, mdv1::MET25-TOM20(1-51aa)-MDV1(1-714aa)*
JSY9805	*MATa, leu2Δ1, his3Δ200, trp1Δ63, ura3-52, lys2Δ202, fis1::HIS3, caf4::KanMX, dnm1::GFP-DNM1, mdv1::MET25-TOM20(1-51aa)-MDV1(218-714aa)*
JSY9806	*MATa, leu2Δ1, his3Δ200, trp1Δ63, ura3-52, lys2Δ202, fis1::HIS3, caf4::KanMX, dnm1::GFP-DNM1, mdv1::MET25-TOM20(1-51aa)-MDV1(317-714aa)*
JSY9807	*MATα, leu2Δ1, his3Δ200, trp1Δ63, ura3-52, lys2Δ202, caf4::KanMX, mdv1:: MET25-MDV1*
JSY10005	*MATα, leu2Δ1, his3Δ200, trp1Δ63, ura3-52, lys2Δ202, dnm1::HIS3, fis1::HIS3, caf4::KanMX, mdv1::MET25-hFIS1(1-119aa)-yFIS1(122-155aa)*
JSY10006	*MATα, leu2Δ1, his3Δ200, trp1Δ63, ura3-52, lys2Δ202, dnm1::HIS3, fis1::HIS3, caf4::KanMX, mdv1::MET25-hMff(1-198aa)-yFIS1(127-155aa)*
JSY10007	*MATα, leu2Δ1, his3Δ200, trp1Δ63, ura3-52, lys2Δ202, dnm1::HIS3, fis1::HIS3, caf4::KanMX, mdv1::MET25-TOM20(1-51aa)-hMiD49(48-454aa)*
JSY10009	*MATα, leu2Δ1, his3Δ200, trp1Δ63, ura3-52, lys2Δ202, dnm1::HIS3, fis1::HIS3, caf4::KanMX, mdv1::MET25-TOM20(1-51aa)-hMiD51(47-463aa)*

Table S3. Plasmids used in this study

ID	Plasmid	Protein expressed
B363	*pRS415-DNM1*	Dnm1
B493	*pRS415-MET25*	none
B1607	*pRS415MET25-yFIS1*	yFis1
B1642	*p414GPD-mito-ffRFP*	*N. crassa* ATP9$^{1\text{-}69aa}$ + fast folding DsRed
B1816	*pRS416MET25-hDRP1*	hDrp1 (isoform 3)
B1808	*pRS415MET25-MDV1*	Mdv1
B2053	*pRS416MET25-MDV1*	Mdv1
B2729	*pRS415MET25-T20-MDV1^{FL}*	T20$^{1\text{-}51aa}$-Mdv1$^{1\text{-}714aa}$
B2731	*pRS415MET25-T20-MDV1^{CCWD}*	T20$^{1\text{-}51aa}$-mdv1$^{218\text{-}714aa}$
B2732	*pRS415MET25-T20-MDV1^{WD}*	T20$^{1\text{-}51aa}$-mdv1$^{317\text{-}714aa}$
B2821	*pRS415MET25-MDV1-3HA*	Mdv1-3HA
B2925	*pRS415MET25-T20-MDV1^{FL}-3HA*	T20$^{1\text{-}51aa}$-Mdv1$^{1\text{-}714aa}$-3HA
B2927	*pRS415MET25-T20- MDV1^{CCWD}-3HA*	T20$^{1\text{-}51aa}$-Mdv1$^{218\text{-}714aa}$-3HA
B2928	*pRS415MET25-T20- MDV1^{WD}-3HA*	T20$^{1\text{-}51aa}$-Mdv1$^{317\text{-}714aa}$-3HA
B2933	*pRS415MET25-T20-DNM1*	T20$^{1\text{-}51aa}$-Dnm1
B2934	*pRS415MET25-DNM1-yFIS1*	Dnm1-yFis1$^{131\text{-}155aa}$
B3090	*pRS415MET25-mOMGFP-yFIS1*	mOMGFP-yFis1$^{131\text{-}155aa}$
B3162	*pYSG-IBA167-hDRP1*	Flag-Strep-PP-hDrp1 (isoform 3)
B3237	*pRS415MET25- hDRP1-3HA*	hDrp1-3HA
B3238	*pRS415MET25-T20-hMiD49^{cyto}-3HA*	T20$^{1\text{-}51aa}$-hMiD49$^{48\text{-}454aa}$-3HA
B3239	*pRS415MET25-T20-hMiD51^{cyto}-3HA*	T20$^{1\text{-}51aa}$-hMiD51$^{47\text{-}463aa}$-3HA
B3244	*pRS415MET25-3HA-hMff^{cyto}-yFIS1*	3HA-hMff$^{1\text{-}198aa}$-yFis1$^{131\text{-}155aa}$
B3247	*pRS415MET25-3HA-hFIS1^{cyto}-yFIS1*	3HA-hFis1$^{1\text{-}119aa}$-yFis1$^{131\text{-}155aa}$
B3259	*pYSG-IBA167-hMiD49^{cyto}*	Flag-Strep-PP-hMiD49$^{48\text{-}454aa}$
B3262	*pYSG-IBA167-hMff^{cyto}*	Flag-Strep-PP-hMff $^{1\text{-}198aa}$
B3265	*pRS416CUP1-mGFP-hDRP1*	mGFP-hDrp1 (isoform 3)
B3294	*pYSG-IBA167-10HIS-hMiD49^{cyto}*	Flag-Strep-PP-10His-hMiD49 $^{48\text{-}454aa}$
B3357	*pMAL-c2x-hMff^{cyto}*	MBP-10xHIS-PP-hMff $^{1\text{-}198aa}$

T20 encodes yTom20, amino acids 1–51, N-terminal mitochondrial outer membrane anchor. yFIS1 encodes yFis1, amino acids 131–155, C-terminal mitochondrial outer membrane anchor. CCWD, coiled coil + WD repeat; cyto, cytoplasmic domain; h, human; FL, full length; mOMGFP, monomeric mitochondrial outer membrane GFP; PP, prescission protease cleavage site; T20, Tom20 membrane targeting domain; TM, transmembrane domain; WD, WD repeat; y, yeast.

CHAPTER 4

STRUCTURAL BASIS OF MITOCHONDRIAL RECEPTOR BINDING AND GTP DRIVEN CONFORMATIONAL CONSTRICTION BY DYNAMIN-RELATED PROTEIN 1

Raghav Kalia, Ray Y.-R Wang, Ali Yusuf, Paul V. Thomas, David A. Agard, Janet M. Shaw and Adam Frost

This article was published as a preprint in the preprint server BioRxiv

 doi: 10.1101/172809

Structural Basis of Mitochondrial Receptor Binding and GTP-Driven Conformational Constriction by Dynamin-Related Protein 1

Raghav Kalia[1,2,3,5], Ray Yu-Ruei Wang[1,3,4], Ali Yusuf[1,3], Paul V. Thomas[1,3,5], David A. Agard[1,3,4], Janet M. Shaw[2,4], and Adam Frost[1,2,3,5]

[1]Department of Biochemistry and Biophysics, University of California, San Francisco, San Francisco, CA 94158 USA

[2]Department of Biochemistry, University of Utah, Salt Lake City, UT, 84112 USA

[3]California Institute for Quantitative Biomedical Research, San Francisco, CA 94158 USA

[4]Howard Hughes Medical Institute

[5]Chan Zuckerberg Biohub, San Francisco, CA 94158 USA

Corresponding author. Email: adam.frost@ucsf.edu

Abstract

Mitochondrial inheritance, genome maintenance, and metabolic adaptation all depend on organelle fission by Dynamin-Related Protein 1 (DRP1) and its mitochondrial receptors. DRP1 receptors include the paralogs Mitochondrial Dynamics 49 and 51 (MID49/MID51) and Mitochondrial Fission Factor (MFF), but the mechanisms by which these proteins recruit DRP1 and regulate its activities are unknown. Here we present a cryoEM structure of human, full-length DRP1 bound to MID49 and an analysis of structure- and disease-based mutations. We report that GTP binding allosterically induces a remarkable elongation and rotation of the G-domain, Bundle-Signaling Element (BSE) and connecting hinge loops of DRP1. In this nucleotide-bound conformation, a distributed network of multivalent interactions promotes DRP1 copolymerization into a linear filament with MID49, MID51 or both. Subsequent GTP hydrolysis and exchange within the filament leads to receptor dissociation, shortening through disassembly, and concomitant curling of DRP1 oligomers into closed rings. The dimensions of the closed DRP1 rings are consistent with DRP1-constricted mitochondrial tubules observed in human cells. These structures are the first views of full-length, receptor- and nucleotide-bound dynamin-family GTPases and—in comparison with nucleotide-free crystal structures—teach us how these molecular machines perform mechanical work through nucleotide-driven allostery.

Introduction

Pioneering work in yeast and other model systems revealed that fragmentation of the mitochondrial reticulum disperses units of the organelle during cell division[1-3], coordinates morphological adaptation with metabolic demand[4-7], and quarantines damaged units for turnover[8-10]. Recent work also led to the discovery of the role mitochondrial fission plays in regulated cell death pathways[11-19], brain development and synaptic function[20-23], and how certain pathogens disrupt these processes and hijack mitochondrial resources[24-26]. Finally, there is a growing understanding of how inter-organelle contacts between the ER and mitochondria initiate mitochondrial fission[27,28], and how this process regulates mitochondrial genome duplication and integrity[29,30]. The master regulator that unites these processes across eukaryotic evolution is the membrane-remodeling GTPase DRP1[4,7,31-37].

DRP1 is necessary but not sufficient for mitochondrial fission because receptor proteins must recruit the enzyme to the Outer Mitochondrial Membrane (OMM). In mammals, these include the paralogs MItochondrial Dynamics proteins MID49 and MID51 or the Mitochondrial Fission Factor, MFF [32,35,38-41]. Following receptor-dependent recruitment, DRP1 assembles into polymers that encircle mitochondria and, through still poorly understood mechanisms, channels energy from GTP binding, hydrolysis, and nucleotide exchange into a mechanochemical constriction[13,41-46]. In addition to DRP1 and

its OMM receptors, a recent study revealed that a second member of the dynamin-family of GTPases, dynamin-2, enacts the final fission event downstream of DRP1-driven constriction of a mitochondrial tubule[47]. Thus, mitochondrial division is a stepwise reaction regulated by DRP1 receptor binding, oligomerization and nucleotide-dependent conformational dynamics.

We and others have reported that the OMM receptors MFF or MID49/51 are independently sufficient to recruit DRP1 in order to divide mitochondria[38,39,41,48]. We also reported that MID49/51 can coassemble with DRP1 forming a copolymer with a dramatically different morphology than reported for dynamin-family members[41]. While these results suggest that an adaptor protein could alter the architecture of a dynamin polymer to facilitate a mitochondria-specific activity, the architecture and functions of this coassembly remain unclear.

Here, we report the structural basis of DRP1 coassembly with MID49/MID51. Our cryoEM structure reveals how nucleotide binding to the G-domain induces conformational changes that allosterically propagate through the BSE to open and elongate DRP1 and thereby expose multiple receptor-binding surfaces. MID49/51 binding stabilizes a specific alignment of DRP1 tetramers to nucleate polymerization of a linear co-filament. Then, in a path-dependent reaction, we show how GTP hydrolysis and nucleotide exchange lead to conformational constriction by the polymer. Specifically, when DRP1 subunits within

the cofilament exchange and hydrolyze nucleotide, they dissociate from MID49/51 receptors and the entire polymer dynamically shortens and curls into a closed ring. Analysis of structure-based and disease-causing mutations indicate that allosterically driven rearrangements of the stalk helices—and the critical L1N^{S} loop—support curling from linear strings into constricted rings following receptor dissociation.

Results and Discussion

To date, many structural studies of dynamin-family proteins have relied upon mutated or truncated constructs to facilitate crystallization. We purified wild-type, full-length human DRP1 including the N-terminal GTPase domain (G-domain), Bundle Signaling Element (BSE), and four-helix bundle known as the stalk (Fig. 1a). This construct also contained the lipid binding ~100 amino acid region referred to as the variable domain (VD) that sits between the third and fourth alpha helices of the stalk, analogous to the Pleckstrin Homology (PH) domain found in endocytic dynamin proteins. A crystal structure of a nucleotide-free and truncated DRP1 mutant revealed the organization of these domains and an overall similarity with the structure of nucleotide-free endocytic dynamin[42,49,50]. We also purified soluble truncations of MID49 and MID51 engineered to lack their N-terminal transmembrane anchors but include the cytoplasmic

nucleotidyltransferase-like domain and the "Dynamin Recruitment Region" (DRR) required for DRP1 binding (Fig 1a)[38,51-54].

Incubating equimolar ratios of DRP1 with soluble $MID49_{126-454}$, $MID51_{132-463}$, or both proteins together, in the presence of GTP resulted in cofilament assembly (Extended Data Figs. 1-2). We focused on the filaments formed with $MID49_{126-454}$ in the presence of the non-hydrolyzable analog GMPPCP and determined their structure from cryoEM images (Extended Data Figs. 3-9 and Table 1). 3D reconstruction resolved elongated DRP1 dimers bound stoichiometrically to $MID49_{126-454}$, without assignable density for the variable domain (Fig. 1b, Extended Data Fig. 4). Surprisingly, each chain of DRP1 bound MID49 at four different sites, and each MID49 in turn bound four DRP1 molecules to yield a vast and highly avid interaction network (Figs. 1b-c, Extended Data Figs. 4 and 8). MID49 binding to four separate DRP1 molecules stabilized a linear arrangement of inter-DRP1 interfaces reminiscent of those observed for other dynamin-family proteins by X-ray crystallography (Fig. 1b, Extended Data Figs. 4 and 8)[42,49,50,55-57].

MID49's DRR motif occupied the space between two neighboring G-domains and contacted both via MID-interaction interfaces 1 and 2 (buried surface areas of ~530$Å^2$ and ~200 $Å^2$, respectively, see Fig. 1b-d). The precise spacing required for this bivalent G-domain interaction explains why previous mutagenesis efforts suggested that the size and topology of the β4–α4 loop, rather than its exact sequence (which differs between

MID49 and MID51) are critical determinants of binding. Single point mutations within this loop for MID49 and MID51 did not disrupt binding, while mutations that altered the length, topology or positioning of the loop did[51,52,54]. We found that mutating conserved DRP1 residues involved in interface 1—the energetically most significant interface—did prevent coassembly. Specifically, the D190A mutation should neutralize an interface 1 salt bridge and the D221A mutation should alter the conformation of an interface 1 loop (Fig. 1d). We observed that both mutants prevented assembly with MID49 and altered DRP1's self-assembly properties (Extended Data Figs. 10-12).

Unexpectedly, MID49 also made contact with the stalk loops of a third and fourth DRP1 molecule through MID-interaction interfaces 3 and 4 (buried surface areas of ~450Å^2 and ~230Å^2, respectively, Fig. 1c, e, and f). The loops involved in both interaction interfaces 3 and 4 determine the assembly properties of higher-order dynamin-family oligomers [42,49,50,55-57]. MID-interaction surface 3, in particular, harbors the conserved loop L1N^S and is the site of multiple disease alleles that lead to elongated mitochondrial morphology, including G362D and G363D (Fig. 1e, Extended Data Figs. 10-11 and [58-60]). Prior work has also established that this loop comprises part of the intra-molecular PH domain binding site for the soluble state of endocytic dynamin tetramers (Extended Data Fig. 13)[57], and is a determinant of conformational heterogeneity for these and other dynamin-family proteins[55,57,61]. The presence of disease alleles near this interface

suggests that these mutations may compromise receptor interactions and that defects in the recruitment of DRP1 to mitochondria may contribute to pathogenesis. As discussed below, we found that the G362D mutant (Fig. 1e) failed to coassemble with MID49 and displayed altered assembly and conformational properties (Extended Data Figs. 12-15).

Understanding the allosteric coupling between nucleotide binding, hydrolysis or exchange and the conformational repertoire of dynamin-family GTPases remains an unmet challenge[62,63]. We observed that the GMPPCP-bound G-domains and the BSE of DRP1 adopt strikingly different conformations in the cryoEM density compared to the nucleotide-free crystal structure[42]. In addition to other nucleotide-induced conformational changes within the G-domain, the most salient are the closing of the G2/switch-1 loop to form a closed "lid" over the nucleotide (Figs. 2a-c). The closure of the switch-1 lid propagates through the adjacent beta sheet to push the α-helices of the BSE into an orthogonal position (Extended Data Movie 1). When evaluated in the context of a stalk interface-2 DRP1 dimer, this conformational change is an impressive 90° rotation of the G-domain and a 40Å translation toward the stalk (Fig. 2d, Extended Data Movies 2-3). Two of the three DRP1 surfaces that engage the DRR of MID49 (MID receptor interaction interfaces 1 and 2, Figs. 1-2) are inaccessible in the nucleotide-free state but become available for binding upon nucleotide-driven elongation (Fig. 2d, Extended Data Movies 2-3).

Since DRP1's ability to polymerize into linear filaments with MID49 or MID51 depended on non-hydrolyzable GTP analogs, we next evaluated the dynamics of these filaments in the presence of hydrolyzable GTP. Following copolymerization in the presence of the non-hydrolyzable analog, we exchanged GMPPCP for GTP through dialysis and followed the reaction using negative stain transmission electron microscopy at sequential time points until the GTP was exhausted. We observed that the linear DRP1-MID49 cofilaments disassembled into small oligomers upon complete hydrolysis to GDP and exhibited a fascinating dynamic instability at intermediate time points (Fig. 3). Specifically, the long and linear filaments seen at early time points disassembled into shorter, curling oligomers that—upon reaching a reproducibly narrow range of lengths—spontaneously closed into constricted rings that were remarkably uniform in diameter (Fig. 3).

In a separate but related experiment, we evaluated the assembly properties of the DRP1 mutant G362D with and without $MID49_{126-454}$. As described above, this disease-associated residue sits at the base of the $L1N^S$ loop that forms part of the third interface with MID49 (Figs. 1c, 1e, Extended Data Fig. 13). We found that $DRP1_{G362D}$ purified as a nearly monodisperse and stable dimer, rather than a mix of tetramers and higher order species observed for the wild-type, full-length protein (Extended Data Fig. 12). In addition, $DRP1_{G362D}$ exclusively formed rings, not filaments, with or without $MID49_{126-454}$ and in the

presence of GMPPCP or GTP (Fig. 4a, Extended Data Figs. 14-15). These rings resembled those observed with wild-type DRP1 in all respects except that the wild-type protein only formed closed rings from the pre-formed linear MID49 copolymers through the path-dependent reaction described above (Fig. 3 versus Fig. 4). Using the non-hydrolyzable GTP analog GMPPCP with the $DRP1_{G362D}$ rings also improved structural homogeneity, presumably because the wild-type rings remain dynamic and eventually disassembled in the presence of GTP upon complete hydrolysis to GDP (Fig. 3).

We imaged the $DRP1_{G362D}$ rings using cryoEM and used 2D class averages of the predominant 12-dimer closed ring to model the architectural differences between the linear filaments and the closed rings (Fig. 4, Extended Data Fig. 14-15). To account for the projected ring density, the G-domain and the BSE of DRP1 must move even further down toward the stalks. Moreover, while stalk interface-2 remains constant—as revealed by the X-shaped projected dimer (Fig. 4c)—the curvature of the ring dictates that stalk interfaces 1 and 3 must be extensively remodeled to allow a ~30 degree bending per dimer in comparison with the linear DRP1-MID49 copolymer (Fig. 4d, Extended Data Fig. 15, Movie 4). We did not observe any density for MID49 in the wild-type rings that form by curling of the MID49-DRP1 cofilament in the presence of GTP, nor in our higher-resolution analysis of the $DRP1_{G362D}$ rings that form with or without MID49 present (Fig. 4b-c, Extended Data Fig. 14-15).

We note that even the most constricted form of the closed ring is insufficient to drive complete mitochondrial fission because the inner diameter is only ~16nm. This length suggests that a constricted membrane tubule would be stable and that the structures we have observed in vitro could correspond with the highly-constricted but pre-fission state observed in living cells when another dynamin-family protein, the primarily endocytic dynamin-2, is depleted[47]. Thus, initial constriction by DRP1 may stabilize the high degree of membrane curvature that is suitable, perhaps even tuned, for the recruitment and final fission event catalyzed by additional dynamin-family enzymes.

Together, these findings establish four conceptual advances. First, our cryoEM structure revealed how receptor proteins like MID49/MID51 recruit and stabilize a specific nucleotide-bound conformation of DRP1 and nucleate polymerization of a cofilament. We speculate that the nearly linear properties of this polymer have adapted to encircle low-curvature mitochondrial tubules. The selective stabilization of this open, elongated conformation of DRP1 within the MID receptor cofilament explains why overexpression of the MID receptors inhibits mitochondrial fission[39]. Second, analysis of the MID49-DRP1 copolymer exposed how nucleotide binding induces an impressive conformational rearrangement to expose a network of multi-valent receptor binding sites. We now understand these nucleotide-driven allosteric transformations in detail and in the context of full-length and oligomeric DRP1. Third, a path-dependent constriction reaction revealed

intrinsic GTP-dependent DRP1 properties that are reminiscent of microtubule dynamic instability[64]. In this reaction, nucleotide exchange and hydrolysis led to MID49/51 receptor dissociation, disassembly from the ends of the linear filament, and concomitant curling of the shortened filaments into closed rings. Fourth and finally, analysis of a disease mutant in the $L1N^{S}$ loop, $DRP1_{G362D}$, exposed this loop as a vital determinant of mitochondrial receptor binding and the dynamic inter-stalk interactions that govern oligomer architecture and the ability of dynamin proteins to perform mechanical work.

Acknowledgments

We thank Michael Braunfeld, Cameron Kennedy, David Bulkley, and Alexander Myasnikov and the UCSF Center for Advanced CryoEM, which is supported in part from NIH grants S10OD020054 and 1S10OD021741 and the Howard Hughes Medical Institute. We also thank the QB3 shared cluster and NIH grant 1S10OD021596-01, Jean-Paul Armache, Nathaniel Talledge for microscopy advice, and Charles Greenberg for consulting on structural modeling. This work was further supported by a Faculty Scholar grant from the Howard Hughes Medical Institute (A.F.), the Searle Scholars Program (A.F.), NIH grant 1DP2GM110772-01 (A.F.), NIH grants GM53466 and GM84970 (J.S.), and the Howard Hughes Medical Institute (R.W., J.S., D.A.). A.F. is a Chan Zuckerberg Biohub investigator.

227 **Author Contributions**

228 R.K., J.S. and A.F. conceived of the study. R.K., R.W., A.Y. and P.T. performed all
229 experiments. R.K., R.W. and A.F. performed the computational analyses. All authors
230 evaluated the results and edited the manuscript. R.K. and A.F. wrote the manuscript with
231 input from all of the authors.

232

233 **Data Accessibility:**

234 All of the cryoEM density maps associated with this study have be deposited in the EMDB
235 with accession numbers EMD-8874(PROC). The atomic coordinates have been
236 deposited in the PDB as 5WP9(PROC).

237 **Figures**

Kalia, et al.
Figure 1

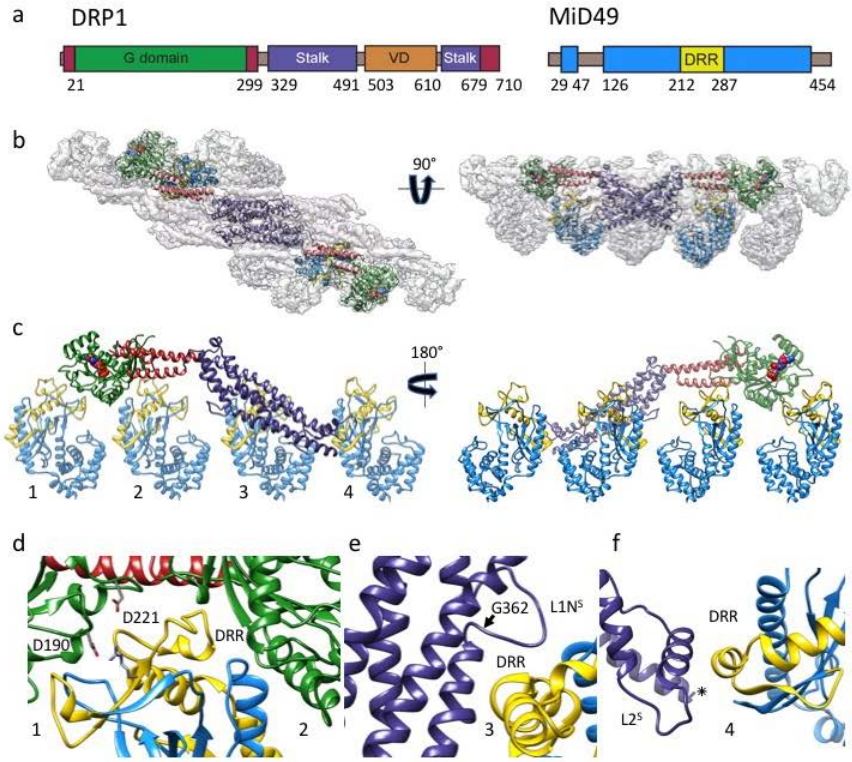

239 **Figure 1: Architecture of the DRP1-MID49 linear filament:** (**a**) DRP1 and MID49
240 domain arrangements. (**b**) Density map and atomic models for DRP1 and $MID49_{126-454}$.
241 Green: G-domain, Red: Bundle Signaling Element (BSE), Purple: Stalk, Blue: MID49,
242 Yellow: Dynamin Recruitment Region (DRR) of MID49. (**c**) Each DRP1 chain contacts
243 four different MID49 molecules, as numbered. (**d**) MID-interaction surfaces 1 and 2.
244 Green ribbons on either side of the DRR come from two separate G-domains, and the
245 residues involved in a key salt bridge for MID-interaction surface 1 are shown as sticks.
246 (**e**) Rotated view of MID-interaction surface 3. Disease-associated DRP1 residue G362
247 (arrow) supports the conformation of the $L1N^S$ loop essential for linear copolymerization
248 with MID receptors. (**f**) Rotated view of MID-interaction surface 4 and the $L2^S$ loop.
249
250
251
252
253
254
255
256
257

Kalia, et al.
Figure 2

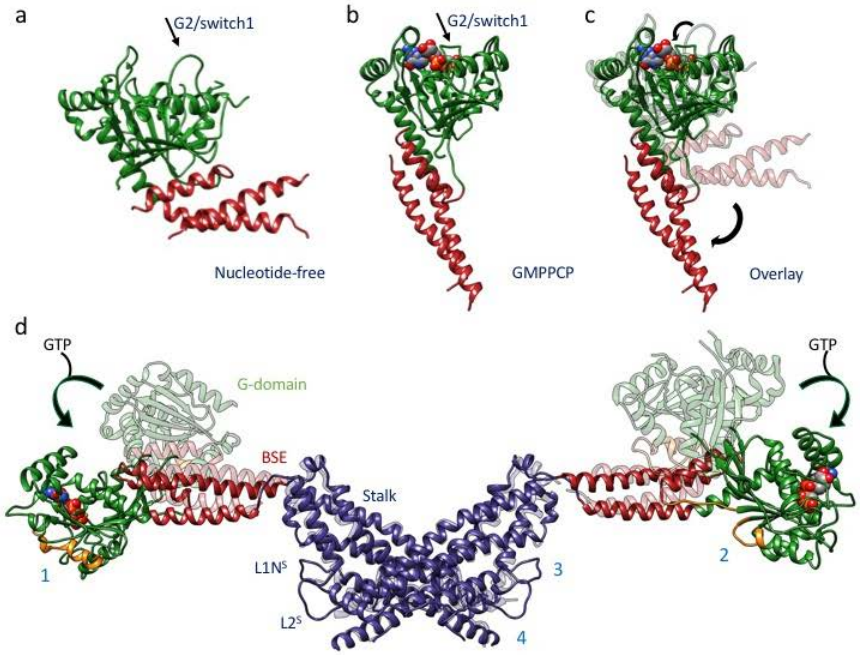

Figure 2: Nucleotide-driven allosteric elongation of DRP1 exposes MID binding sites: **(a)** nucleotide-free state of DRP1 G-domain and BSE as seen in a crystal structure (PDB ID: 4BEJ). Arrow points to the G2/switch1 loop. **(b)** GMPPCP-bound G-domain-BSE conformation determined by cryoEM. **(c)** Overlay of A and B. Curved arrows highlight the closing of G2/switch 1 "lid" and the opening of the BSE "wrist". **(d)** Global conformational change induced by nucleotide binding. Rotation and translation of the G-domain and BSE elongates the dimer and exposes MID-interaction surfaces 1 and 2 (annotated on separate monomers for clarity). The surfaces of the G-domains that engage MID receptors are rendered orange in the nucleotide-bound and elongated conformation.

Kalia, et al.
Figure 3

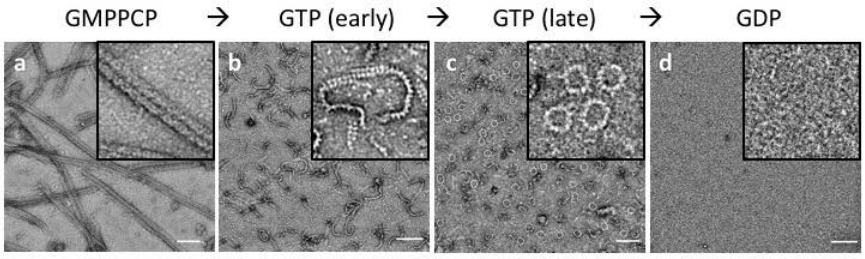

279 **Figure 3: Dynamic instability of the DRP1-MID49 linear assembly and curling into**
280 **closed DRP1 rings**: **(a)** DRP1-MID49$_{126-454}$ linear filaments copolymerized with
281 GMPPCP. **(b-c)** Subsequent exchange into GTP leads to partial disassembly and curling
282 into closed rings. **(d)** GTP exhaustion leads to complete oligomer disassembly.
283 Bars=100nm.
284
285
286
287
288
289
290
291
292
293
294
295
296
297

Kalia, et al.
Figure 4

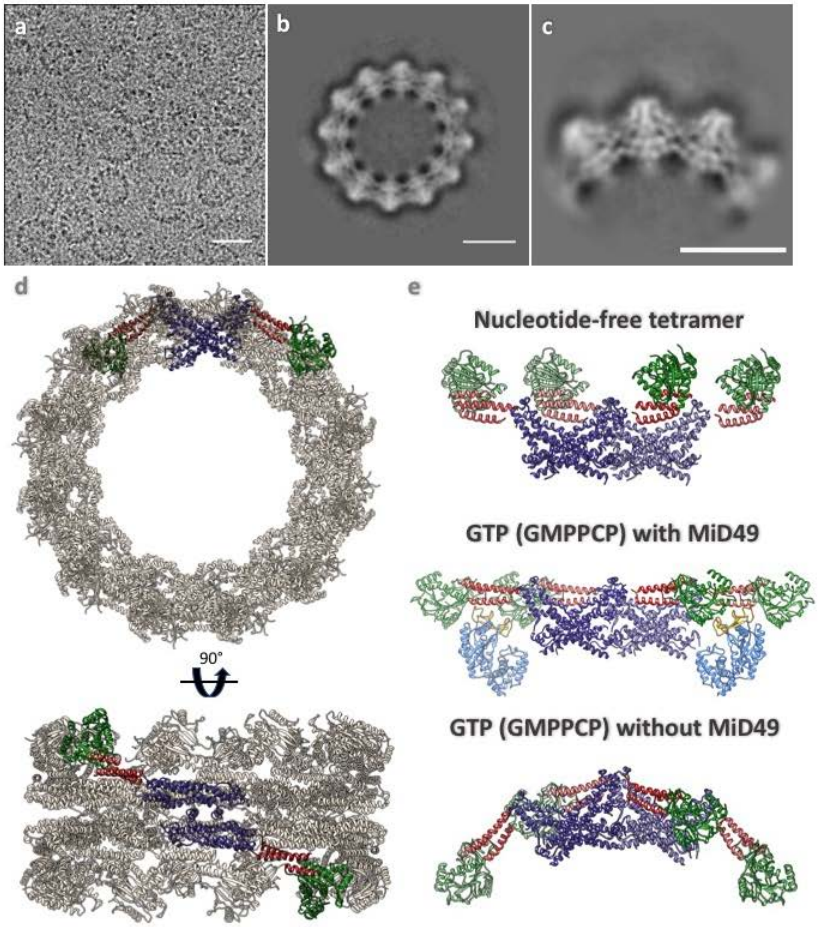

299 **Figure 4: DRP1$_{G362D}$ cannot bind MID49 and forms rings exclusively with GMPPCP**
300 **or GTP. (a)** CryoEM micrograph of DRP1$_{G362D}$ rings. **(b)** 2D class average of the
301 predominant closed ring that comprises 12 DRP1 dimers. **(c)** 2D class average of a
302 quarter of the ring revealing the secondary structure elements of the "X"-shaped DRP1
303 dimer. **(d)** 3D model of the closed ring. **(e)** Comparison between DRP1 tetramers
304 observed in the nucleotide-free state (top, PDB ID: 4BEJ), the GMPPCP and MID49$_{126-}$
305 $_{454}$-bound linear state (middle), and the bent conformation modeled for the rings. Bar for
306 **(a)** = 30nm, for **(b, c)** =100Å.

307 **Extended Data**

308 Methods

309 Figures 1 to 15

310 Movies 1 to 4

311 Table 1

312 Extended Data References

313

References

1 Mishra, P. & Chan, D. C. Mitochondrial dynamics and inheritance during cell division, development and disease. *Nature reviews. Molecular cell biology* **15**, 634-646, doi:10.1038/nrm3877 (2014).

2 Jourdain, I., Gachet, Y. & Hyams, J. S. The dynamin related protein Dnm1 fragments mitochondria in a microtubule-dependent manner during the fission yeast cell cycle. *Cell Motil Cytoskeleton* **66**, 509-523, doi:10.1002/cm.20351 (2009).

3 Kanfer, G. & Kornmann, B. Dynamics of the mitochondrial network during mitosis. *Biochem Soc Trans* **44**, 510-516, doi:10.1042/BST20150274 (2016).

4 Toyama, E. Q. *et al.* Metabolism. AMP-activated protein kinase mediates mitochondrial fission in response to energy stress. *Science (New York, N.Y.)* **351**, 275-281, doi:10.1126/science.aab4138 (2016).

5 Roy, M., Reddy, P. H., Iijima, M. & Sesaki, H. Mitochondrial division and fusion in metabolism. *Current opinion in cell biology* **33**, 111-118, doi:10.1016/j.ceb.2015.02.001 (2015).

6 Picard, M., Juster, R. P. & McEwen, B. S. Mitochondrial allostatic load puts the 'gluc' back in glucocorticoids. *Nat Rev Endocrinol* **10**, 303-310, doi:10.1038/nrendo.2014.22 (2014).

7 Mishra, P. & Chan, D. C. Metabolic regulation of mitochondrial dynamics. *The Journal of cell biology* **212**, 379-387, doi:10.1083/jcb.201511036 (2016).

8 Twig, G. *et al.* Fission and selective fusion govern mitochondrial segregation and elimination by autophagy. *Embo J* **27**, 433-446, doi:10.1038/sj.emboj.7601963 (2008).

9 Frank, M. *et al.* Mitophagy is triggered by mild oxidative stress in a mitochondrial fission dependent manner. *Biochim Biophys Acta* **1823**, 2297-2310, doi:10.1016/j.bbamcr.2012.08.007 (2012).

10 Mao, K. & Klionsky, D. J. Mitochondrial fission facilitates mitophagy in Saccharomyces cerevisiae. *Autophagy* **9**, 1900-1901, doi:10.4161/auto.25804 (2013).

11 Chan, D. C. Fusion and fission: interlinked processes critical for mitochondrial health. *Annu Rev Genet* **46**, 265-287, doi:10.1146/annurev-genet-110410-132529 (2012).

12 Lee, H. & Yoon, Y. Mitochondrial fission: regulation and ER connection. *Mol Cells* **37**, 89-94, doi:10.14348/molcells.2014.2329 (2014).

13 van der Bliek, A. M., Shen, Q. & Kawajiri, S. Mechanisms of mitochondrial fission and fusion. *Cold Spring Harb Perspect Biol* **5**, doi:10.1101/cshperspect.a011072 (2013).

14 Sheridan, C. & Martin, S. J. Mitochondrial fission/fusion dynamics and apoptosis. *Mitochondrion* **10**, 640-648, doi:10.1016/j.mito.2010.08.005 (2010).

15 Parone, P. A. & Martinou, J. C. Mitochondrial fission and apoptosis: an ongoing trial. *Biochim Biophys Acta* **1763**, 522-530, doi:10.1016/j.bbamcr.2006.04.005 (2006).

16 Youle, R. J. & Karbowski, M. Mitochondrial fission in apoptosis. *Nature reviews. Molecular cell biology* **6**, 657-663, doi:10.1038/nrm1697 (2005).

17 Perfettini, J. L., Roumier, T. & Kroemer, G. Mitochondrial fusion and fission in the control of apoptosis. *Trends in cell biology* **15**, 179-183, doi:10.1016/j.tcb.2005.02.005 (2005).

18 Oakes, S. A. & Korsmeyer, S. J. Untangling the web: mitochondrial fission and apoptosis. *Dev Cell* **7**, 460-462, doi:10.1016/j.devcel.2004.09.010 (2004).

19 Frank, S. *et al.* The role of dynamin-related protein 1, a mediator of mitochondrial fission, in apoptosis. *Dev Cell* **1**, 515-525 (2001).

20 Ishihara, N. *et al.* Mitochondrial fission factor Drp1 is essential for embryonic development and synapse formation in mice. *Nature cell biology* **11**, 958-966, doi:10.1038/ncb1907 (2009).

21 Wakabayashi, J. *et al.* The dynamin-related GTPase Drp1 is required for embryonic and brain development in mice. *Journal of Cell Biology* **186**, 805-816, doi:10.1083/jcb.200903065 (2009).

22 Kageyama, Y. *et al.* Parkin-independent mitophagy requires Drp1 and maintains the integrity of mammalian heart and brain. *Embo J* **33**, 2798-2813, doi:10.15252/embj.201488658 (2014).

23 Schwarz, T. L. Mitochondrial trafficking in neurons. *Cold Spring Harb Perspect Biol* **5**, doi:10.1101/cshperspect.a011304 (2013).

24 Chatel-Chaix, L. *et al.* Dengue Virus Perturbs Mitochondrial Morphodynamics to Dampen Innate Immune Responses. *Cell Host Microbe* **20**, 342-356, doi:10.1016/j.chom.2016.07.008 (2016).

25 Welsch, S. *et al.* Composition and three-dimensional architecture of the dengue virus replication and assembly sites. *Cell Host Microbe* **5**, 365-375, doi:10.1016/j.chom.2009.03.007 (2009).

26 Kim, S. J. *et al.* Hepatitis B virus disrupts mitochondrial dynamics: induces fission and mitophagy to attenuate apoptosis. *PLoS Pathog* **9**, e1003722, doi:10.1371/journal.ppat.1003722 (2013).

27 Friedman, J. R. *et al.* ER tubules mark sites of mitochondrial division. *Science (New York, N.Y.)* **334**, 358-362, doi:10.1126/science.1207385 (2011).

28 Murley, A. *et al.* ER-associated mitochondrial division links the distribution of mitochondria and mitochondrial DNA in yeast. *eLife* **2**, e00422, doi:10.7554/eLife.00422 (2013).

29 Lewis, S. C., Uchiyama, L. F. & Nunnari, J. ER-mitochondria contacts couple mtDNA synthesis with mitochondrial division in human cells. *Science (New York, N.Y.)* **353**, aaf5549, doi:10.1126/science.aaf5549 (2016).

30 Osman, C., Noriega, T. R., Okreglak, V., Fung, J. C. & Walter, P. Integrity of the yeast mitochondrial genome, but not its distribution and inheritance, relies on mitochondrial fission and fusion. *Proc Natl Acad Sci U S A* **112**, E947-956, doi:10.1073/pnas.1501737112 (2015).

31 Chang, C. R. & Blackstone, C. Dynamic regulation of mitochondrial fission through modification of the dynamin-related protein Drp1. *Ann N Y Acad Sci* **1201**, 34-39, doi:10.1111/j.1749-6632.2010.05629.x (2010).

32 Elgass, K., Pakay, J., Ryan, M. T. & Palmer, C. S. Recent advances into the understanding of mitochondrial fission. *Biochim Biophys Acta* **1833**, 150-161, doi:10.1016/j.bbamcr.2012.05.002 (2013).

33 Otera, H., Ishihara, N. & Mihara, K. New insights into the function and regulation of mitochondrial fission. *Biochim Biophys Acta* **1833**, 1256-1268, doi:10.1016/j.bbamcr.2013.02.002 (2013).

34 Prudent, J. *et al.* MAPL SUMOylation of Drp1 Stabilizes an ER/Mitochondrial Platform Required for Cell Death. *Molecular cell* **59**, 941-955, doi:10.1016/j.molcel.2015.08.001 (2015).

35 Bui, H. T. & Shaw, J. M. Dynamin assembly strategies and adaptor proteins in mitochondrial fission. *Current biology : CB* **23**, R891-899, doi:10.1016/j.cub.2013.08.040 (2013).

36 Koirala, S. *et al.* Molecular architecture of a dynamin adaptor: implications for assembly of mitochondrial fission complexes. *The Journal of cell biology* **191**, 1127-1139, doi:10.1083/jcb.201005046 (2010).

37 Bleazard, W. *et al.* The dynamin-related GTPase Dnm1 regulates mitochondrial fission in yeast. *Nature cell biology* **1**, 298-304, doi:10.1038/13014 (1999).

38 Osellame, L. D. *et al.* Cooperative and independent roles of the Drp1 adaptors Mff, MiD49 and MiD51 in mitochondrial fission. *Journal of cell science* **129**, 2170-2181, doi:10.1242/jcs.185165 (2016).

39 Palmer, C. S. *et al.* Adaptor proteins MiD49 and MiD51 can act independently of Mff and Fis1 in Drp1 recruitment and are specific for mitochondrial fission. *J Biol Chem* **288**, 27584-27593, doi:10.1074/jbc.M113.479873 (2013).

40 Palmer, C. S. *et al.* MiD49 and MiD51, new components of the mitochondrial fission machinery. *EMBO reports* **12**, 565-573, doi:10.1038/embor.2011.54 (2011).

41 Koirala, S. *et al.* Interchangeable adaptors regulate mitochondrial dynamin assembly for membrane scission. *Proc Natl Acad Sci U S A* **110**, E1342-1351, doi:10.1073/pnas.1300855110 (2013).

42 Frohlich, C. *et al.* Structural insights into oligomerization and mitochondrial remodelling of dynamin 1-like protein. *Embo J* **32**, 1280-1292, doi:10.1038/emboj.2013.74 (2013).

43 Mears, J. A. *et al.* Conformational changes in Dnm1 support a contractile mechanism for mitochondrial fission. *Nat Struct Mol Biol* **18**, 20-26, doi:10.1038/nsmb.1949 (2011).

44 Ingerman, E. *et al.* Dnm1 forms spirals that are structurally tailored to fit mitochondria. *The Journal of cell biology* **170**, 1021-1027, doi:10.1083/jcb.200506078 (2005).

45 Ferguson, S. M. & De Camilli, P. Dynamin, a membrane-remodelling GTPase. *Nature reviews. Molecular cell biology* **13**, 75-88, doi:10.1038/nrm3266 (2012).

46 Daumke, O. & Praefcke, G. J. Invited review: Mechanisms of GTP hydrolysis and conformational transitions in the dynamin superfamily. *Biopolymers* **105**, 580-593, doi:10.1002/bip.22855 (2016).

47 Lee, J. E., Westrate, L. M., Wu, H., Page, C. & Voeltz, G. K. Multiple dynamin family members collaborate to drive mitochondrial division. *Nature* **540**, 139-143, doi:10.1038/nature20555 (2016).

48 Loson, O. C., Song, Z., Chen, H. & Chan, D. C. Fis1, Mff, MiD49, and MiD51 mediate Drp1 recruitment in mitochondrial fission. *Molecular biology of the cell* **24**, 659-667, doi:10.1091/mbc.E12-10-0721 (2013).

49 Faelber, K. *et al.* Crystal structure of nucleotide-free dynamin. *Nature* **477**, 556-560, doi:10.1038/nature10369 (2011).

50 Ford, M. G., Jenni, S. & Nunnari, J. The crystal structure of dynamin. *Nature* **477**, 561-566, doi:10.1038/nature10441 (2011).

51 Richter, V. *et al.* Structural and functional analysis of MiD51, a dynamin receptor required for mitochondrial fission. *The Journal of cell biology* **204**, 477-486, doi:10.1083/jcb.201311014 (2014).

52 Loson, O. C. *et al.* The mitochondrial fission receptor MiD51 requires ADP as a cofactor. *Structure* **22**, 367-377, doi:10.1016/j.str.2014.01.001 (2014).

53 Liu, R. & Chan, D. C. Drp1 recruitment by Mff, MiD51 and MiD49. *Molecular biology of the cell* **26** (2015).

54 Loson, O. C. *et al.* Crystal structure and functional analysis of MiD49, a receptor for the mitochondrial fission protein Drp1. *Protein Sci* **24**, 386-394, doi:10.1002/pro.2629 (2015).

55 Gao, S. *et al.* Structural basis of oligomerization in the stalk region of dynamin-like MxA. *Nature* **465**, 502-506, doi:10.1038/nature08972 (2010).

56 Haller, O., Gao, S., von der Malsburg, A., Daumke, O. & Kochs, G. Dynamin-like MxA GTPase: structural insights into oligomerization and implications for antiviral activity. *J Biol Chem* **285**, 28419-28424, doi:10.1074/jbc.R110.145839 (2010).

57 Reubold, T. F. *et al.* Crystal structure of the dynamin tetramer. *Nature* **525**, 404-408, doi:10.1038/nature14880 (2015).

58 Vanstone, J. R. *et al.* DNM1L-related mitochondrial fission defect presenting as refractory epilepsy. *Eur J Hum Genet* **24**, 1084-1088, doi:10.1038/ejhg.2015.243 (2016).

59 Sheffer, R. *et al.* Postnatal microcephaly and pain insensitivity due to a de novo heterozygous DNM1L mutation causing impaired mitochondrial fission and function. *Am J Med Genet A* **170**, 1603-1607, doi:10.1002/ajmg.a.37624 (2016).

60 Chang, C. R. *et al.* A lethal de novo mutation in the middle domain of the dynamin-related GTPase Drp1 impairs higher order assembly and mitochondrial division. *J Biol Chem* **285**, 32494-32503, doi:10.1074/jbc.M110.142430 (2010).

61 Gao, S., von der Malsburg, A., Haller, O., Kochs, G. & Daumke, O. Structural basis of oligomerization and the mechano-chemical function in dynamin-like MxA. *Faseb Journal* **25** (2011).

62 Antonny, B. *et al.* Membrane fission by dynamin: what we know and what we need to know. *Embo J* **35**, 2270-2284, doi:10.15252/embj.201694613 (2016).

63 Chappie, J. S. *et al.* A pseudoatomic model of the dynamin polymer identifies a hydrolysis-dependent powerstroke. *Cell* **147**, 209-222, doi:10.1016/j.cell.2011.09.003 (2011).

64 Mitchison, T. & Kirschner, M. Dynamic instability of microtubule growth. *Nature* **312**, 237-242 (1984).

Extended Data

Methods

Construct design

Wild type (WT) DRP1 isoform 2 sequence was purchased from DNASU (sequence ID HsCD00043627, UNIPROT identifier: O00429-3 also known as DLP1a) and was cloned into pET16b plasmid (Novagen) between the Nde1 and BamH1 sites. The vector was kindly provided by the laboratory of Wesley I. Sundquist with a 10X-His tag followed by a PreScission protease site (Leu-Glu-Val-Leu-Phe-Gln-Gly-Pro). Wild-type $MID49_{126-454}$ sequence was PCR amplified and cloned into pGEX6p1 vector having an N-terminal GST tag followed by a PreScission protease site. Site directed mutagenesis was performed on pET16b-DRP1 using the Gibson cloning method to introduce mutations[1]. All constructs were verified using Sanger sequencing.

Protein purification

Protein purification was performed as described[2]. Briefly, plasmids containing the WT DRP1 or $MID49_{126-454}$ sequence were transformed in the BL21-DE3 (RIPL) strain of *E. coli*. The colonies were inoculated in LB culture medium and grown overnight. Secondary inoculations were done the next morning in ZY medium for auto-induction[3,4]. The cultures were grown to an OD_{600} of 0.8 at 37°C in baffled flasks and were shifted to 19°C to grow for another 12 hours. The cultures were spun down and the bacterial pellets were used for protein purification immediately or stored at -80°C.

Full length DRP1 WT and mutant variants were purified as described previously for DRP1 WT with modifications[5]. Briefly, the bacterial pellets were resuspended in buffer A (50 mM

HEPES/NaOH (pH 7.5), 400 mM NaCl, 5 mM $MgCl_2$, 40 mM imidazole, 1 mM DTT, 0.5 mg DNase (Roche) and protease inhibitors (10 mM pepstatin, 50 mM PMSF, 0.5 mM aprotinin and 2 mM leupeptin), followed by cell disruption with a probe sonicator. Lysates were cleared by centrifugation at 40,000xg in Beckman JA 25.5 rotors for 60 min at 4°C. The supernatant was filtered using a 0.45 μm filter and applied to Ni-NTA Agarose beads pre- equilibrated with buffer B (50 mM HEPES/NaOH (pH 7.5), 400 mM NaCl, 5 mM $MgCl_2$, 40 mM imidazole, 1 mM DTT). The beads were washed with 20 column volumes each of buffer B and buffer C (50 mM HEPES/NaOH (pH 7.5), 800 mM NaCl, 5 mM $MgCl_2$, 40 mM imidazole, 1 mM DTT, 1 mM ATP, 10 mM KCl) followed by buffer D (50 mM HEPES/NaOH (pH 7.5), 400 mM NaCl, 5 mM $MgCl_2$, 80 mM imidazole, 1 mM DTT, 0.5% (w/v) CHAPS). A final pre-elution wash was done with 20 column volumes of buffer B. Bound DRP1 was eluted with buffer E (50 mM HEPES/NaOH (pH 7.5), 400 mM NaCl, 5 mM $MgCl_2$, 300 mM imidazole, 1 mM DTT) and dialyzed overnight at 4°C against buffer B without imidazole in the presence of PreScission protease to cleave the N-terminal 10X-His tag. The protein was re-applied to a Ni-NTA column pre-equilibrated with dialysis buffer and was observed to bind the column without the 10X-His tag as well. Subsequently, the protein was eluted with buffer B containing 80 mM imidazole.

Pure protein was concentrated with a 30kDa molecular weight cutoff (MWCO) centrifugal concentration device (Millipore). In a final step, DRP1 was purified by size-exclusion chromatography (SEC) on a Superdex-200 column (GE) in buffer F containing 20 mM HEPES/ NaOH (pH 7.5), 300 mM NaCl, 2.5 mM $MgCl_2$ and 1 mM DTT. Fractions containing DRP1 were pooled, concentrated, flash frozen as single use aliquots in liquid nitrogen and stored at -80°C. Exact masses for purified DRP1 proteins were validated by MALDI-TOF mass spectrometry.

$MID49_{126-454}$ was purified as described with modifications[6]. pGEX6p1-$MID49_{126-454}$ plasmid DNA (human, UNIPROT identifier: Isoform 1 Q96C03-1, also known as MIEF2) was transformed in BL21 (DE3) RIPL cells. The colonies were grown overnight in LB medium and secondary cultures were grown in ZY medium. Cells were grown to an OD_{600} of 0.8-1, collected by centrifugation and processed immediately or stored at -80°C as described above. The bacterial pellets were lysed as described above in MID-buffer A (50 mM Tris pH 8.0, 500 mM NaCl, 5% glycerol, 1 mM DTT and 0.1% (v/v) Triton X-100). The lysates were pre-cleared at 40,000xg and filtered using a 0.45 μm filter before applying to 3 ml glutathione sepharose beads (GE). After overnight binding to beads, the unbound protein was removed and the beads were washed using 20 column volumes each of MID-buffer A and MID-buffer B (50 mM Tris pH 8.0, 500 mM NaCl, 5% glycerol, 1 mM DTT). The protein was eluted with MID-buffer C (50 mM Tris pH 8.0, 500 mM NaCl, 5% glycerol, 1 mM DTT and 20 mM reduced glutathione). The eluate was cleaved overnight with PreScission protease while dialyzing against MID-buffer D (20 mM Tris pH 8.0, 100 mM NaCl, 5% glycerol, 1 mM DTT). Cleaved protein was further purified using ion-exchange chromatography using a Q sepharose (GE) column. The low salt buffer for ion-exchange was the same as MID-buffer D and the high salt buffer was MID-buffer E (20 mM Tris pH 8.0, 1 M NaCl, 5% glycerol, 1 mM DTT). The relevant $MID49_{126-454}$ fractions were pooled, concentrated and further purified using an SEC column pre-equilibrated with MID-buffer F (20 mM Tris pH 8.0, 200 mM NaCl, 5% glycerol, 1 mM DTT). The fractions containing $MID49_{126-454}$ were pooled, concentrated, flash frozen in liquid nitrogen and stored as single use aliquots at -80°C.

Filament assembly, EM sample preparation, data acquisition and processing

To assemble DRP1-$MID49_{126-454}$ filaments, the proteins were mixed to a final concentration of 2 μM each and kept for an hour at room temperature. The mixture was dialyzed against assembly

buffer (20 mM HEPES pH 7.5, 50 mM KCl, 3 mM $MgCl_2$, 1 mM DTT, 200 μM GMPPCP and the detergent octyl-glucopyranoside (Anatrace) at 0.2% final concentration). The filaments were observed by screening in negative stain or vitrified for cryo-EM. For vitrification, the sample was applied to Quantifoil holey carbon grids (R2/2) using a Vitrobot Mark III with 3.5 μl sample, 5 seconds blotting time and a 0 mm offset at 19°C and 100% humidity. Images were collected on an FEI T30 Polara operating at 300kV at a magnification of 31000X. Images were recorded on a Gatan K2 summit camera in super resolution mode that had a binned pixel size of 1.22 Å/pixel. The images were dose fractionated, containing 30-40 frames with a total exposure time of 6-8 seconds, 0.2 seconds per frame and a per frame dose of 1.42 electrons/$Å^2$. SerialEM was used to automate data collection[7]. The defocus range was 0.8-3 μm under focus. The data was motion corrected and dose-weighted using UCSF Motioncorr2[8]. CTF parameter estimation on the non-dose-weighted but motion-corrected stacks was done using CTFFIND4 and GCTF[9,10].

Filaments were boxed using the program e2helixboxer.py from the EMAN2 suite[11]. Particle coordinates were used to extract discrete particles using RELION 1.3-1.4[12] and all further processing was done within the RELION suite. Multiple rounds of 2D classification identified the most well-ordered segments, and 3D autorefine was run using a Relion1.2 version with the IHRSR algorithm implemented[13,14]. The consensus helical structure was used to classify the particles without refining helical symmetry (using RELION 1.4), resulting in 2 major classes that differed slightly in rise and twist (Extended data figure 4). Particles from each class were selected and independently refined again with helical RELION 1.2 and IHRSR. Analysis of these reconstructions revealed that each structure was comprised of three linear filaments that bundle together to form a structure that resembled a triangle in cross-section (Extended data figures 3-4). The vertices of the triangle are formed through asymmetric interactions between the G-domains in adjacent filaments. The significance of these asymmetric G domain interactions has

not been evaluated. The triangular arrangement of the bundled helices is unlikely to correspond to a biologically meaningful architecture, and this structure cannot form if the MID49 receptor is embedded in the outer mitochondrial membrane.

To further improve signal-to-noise, each of the three filaments in each independent half-map was segmented, extracted, resampled on a common grid and summed using UCSF Chimera[15-19]. The respective symmetrized but unfiltered half maps from each class were again aligned to a common grid, summed, averaged along the C2 symmetry axis of the DRP1 dimer. In a last step, relion_postprocess was used to add the resulting and fully symmetrized half maps (Extended data figure 4). These half maps and the final summed map, with differential B-factor sharpening per region (Extended data figures 4-9), were used for atomic modeling using Rosetta as described below.

For the projection structure of the $DRP1_{G362D}$ rings, 2 μM protein was mixed 1:1 molar ratio with $MID49_{126-454}$ and was allowed to sit at room temperature for an hour. The mixture was dialyzed against the assembly buffer (without detergent) overnight. The sample was collected after 12 hours and vitrified using ultra-thin 3 nm carbon support films (Ted Pella). For vitrification, a Mark III vitrobot was used with 3.5 μl sample, 0 mm offset, 100% humidity and 3.5 seconds blot time. The images were collected using an FEI TF20 microscope and SerialEM for automated data collection. The data were recorded with a Gatan K2 camera operating in super resolution mode to collect dose fractionated movie stacks using a binned pixel size of 1.234 Å/pixel. 40 frames were collected per stack (0.2 seconds per frame and 1.42 electrons/$Å^2$). The movie stacks were motion corrected and the parameters of the transfer function were estimated as described above. Approximately 2000 particles were picked manually for initial 2D classification in RELION 1.4 and these averages were used as templates for further particle picking by

Gautomatch (http://www.mrc-lmb.cam.ac.uk/kzhang/). Final 2D averaging of the entire rings versus quarter segments of the rings were computed using Relion1.4.

Model building

The general procedure for atomic model interpretation and validation using Rosetta were performed as described[20]. To obtain an initial model for DRP1, the crystal structure of nucleotide-free DRP1 (PDB ID: 4BEJ)[5] was used for the stalk region and DRP1 G domain-BSE structures bound to GMPPCP (PDB ID: 3W6O) were used for the G-domain and BSE regions. Density-guided model completion for DRP1 was carried out with RosettaCM[21] using this hybridization of DRP1 crystal structures. A converged solution appeared from the low-energy ensemble of the complete models generated by RosettaCM. However, among the low-energy ensemble, residues 503-612 were found to be extremely flexible without cryoEM density constraints and therefore were omitted for further coordinate refinement. For MID49, the highly homologous mouse MID49 crystal structure (81.3% identity, PDB ID: 4WOY, Extended Data Fig. 7)[6] was used to generate a homology model using RosettaCM and used as the starting model.

To enable fragment-based, density-guided model refinement with missing residues (503-612, DRP1), Rosetta iterative local rebuilding tool was customized to disallow backbone rebuilding at breaks within a single chain. Multiple rounds of refinement were done for each component against one half map (training map), and the other half map (validation map) was used to monitor overfitting according to the detailed procedure described in Wang et al.[20].

With the refined model of DRP1 and MID49, we further refined the model in the context of a full assembly that included 8 identical copies of each protein, Mg^{2+} and nucleotide which included all possible inter-domain molecular interactions in the filament (Extended data figure 8).

Pseudo-symmetry was used[22] to enable and facilitate the energy evaluations of all neighboring interactions around the asymmetric unit (Green model, shown in Extended data figure 8) for final model refinement of the full assembly. To this end, refinement was done against the training map. Finally, the half maps were used to determine a weight for the density map that did not introduce overfitting. Using the weight and with the symmetry imposed, the whole assembly of DRP1 and MID49 was refined in the full map, followed by B-factors refinement[23]. Finally, quantification of buried surface area and the number and nature of the bonds involved for each DRP1-MID49 interaction interface modeled by Rosetta were performed with the PISA server (http://www.ebi.ac.uk/pdbe/pisa/).

To design a molecular model for the closed 12-dimer DRP1 rings, we used the diameter, thickness, and angles revealed by the 2D cryoEM class averages of the $DRP1_{G362D}$ rings stabilized with GMPPCP. The atomic coordinates determined above using RosettaCM were used to build the ring in sections, first with repeating dimers of the interface-2 "X-shaped" stalk, then the BSE and finally the G-domains and the angles between these sections were iteratively adjusted until calculated projections of the molecular model corresponded with the features of the experimental projection densities. Both the top (Fig 4b-c) and the side view (Extended data Figure 15) were used as constraints. The complete atomic model of ring was finally refined in Phenix[24] to minimize clashes.

Extended data Table 1

Data Collection	Filaments	Ring
Particles	412684	61574
Pixel Size (Å)	1.22	1.234
Defocus Range (microns)	0.3-4.0	0.3-5.0
Defocus Mean (microns)	1.3	2.1
Defocus Median (microns)	1.3	2.08
Voltage (kV)	300	200
Per frame electron dose ($e^{-}/Å^2$)	1.42	1.42
Refinement		
Resolution	4.2 Å ($FSC_{average}$)	6.1 Å (FRC)
Map sharpening B-factor	-225 (average)	
DRP1 stalk only	-300 to -400	
MID49 only	-150 to -200	
G-domain & BSE	-200	
Validation		
Molprobity score	1.41	1.84
Clashscore, all atoms	2.13	4.94
Favored rotamers (%)	99.25	99.44
RMS (bonds)	0.0107	0.011
RMS (angles)	0.97	1.62
Ramachandran Statistics		
Favored (%)	93.6	88.9
Outliers (%)	1.32	0.37

Kalia, et al.
Extended Data Fig. 1

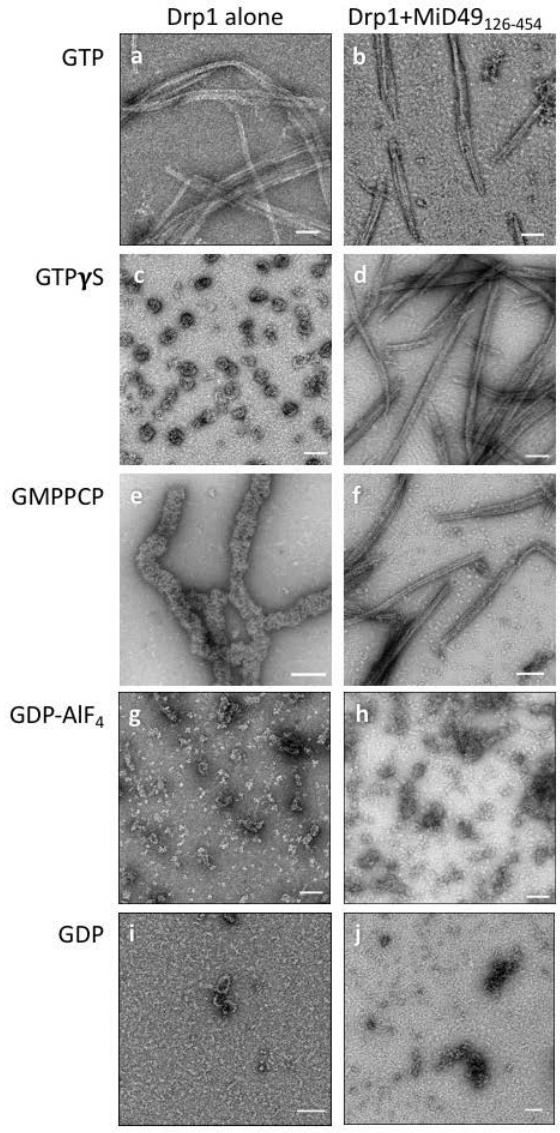

Extended data figure 1: DRP1 assembly states visualized with negative stain electron microscopy in the presence of different guanine nucleotides and stoichiometric $MID49_{126-454}$ ([2μM] for both proteins). Bars = 100nm.

Kalia, et al.
Extended Data Fig. 2

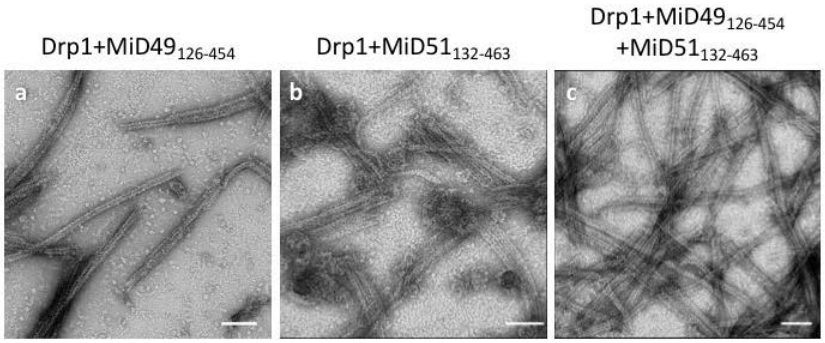

Extended data figure 2: MID49$_{126-454}$ and MID51$_{132-463}$ form indistinguishable assemblies with DRP1 by negative stain electron microscopy. **(a)** DRP1 plus MID49$_{126-454}$ and GMPPCP; **(b)** DRP1 plus MID51$_{132-463}$ and GMPPCP, **(c)** DRP1 plus both MID49 and MID51. Bars = 100nm.

Kalia, et al.
Extended Data Fig. 3

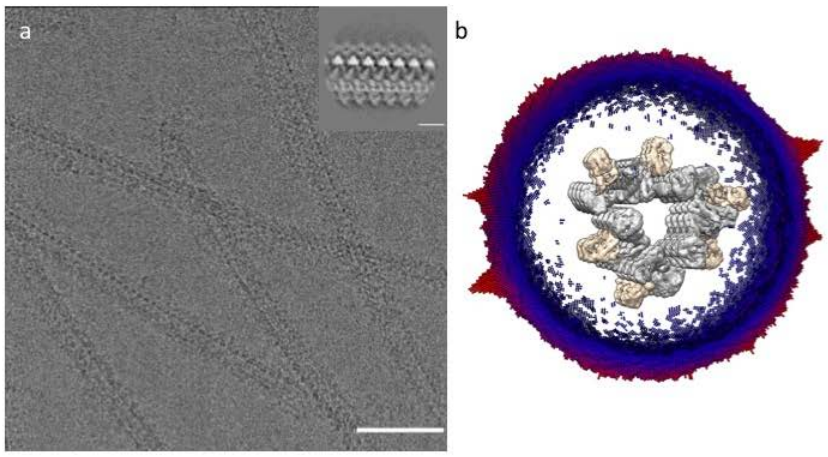

Extended data figure 3: CryoEM imaging and reconstruction. **(a)** An electron cryo-micrograph of DRP1-MID49$_{126-454}$ filaments formed with GMPPCP. Inset shows a representative 2D class average. Bar =100nm, Inset bar =10nm. **(b)** Oblique cross-section of the 3D reconstruction and the distribution of views determined during helical reconstruction. DRP1 density is rendered in grey, MID49 in golden yellow.

Kalia, et al.
Extended Data Fig. 4

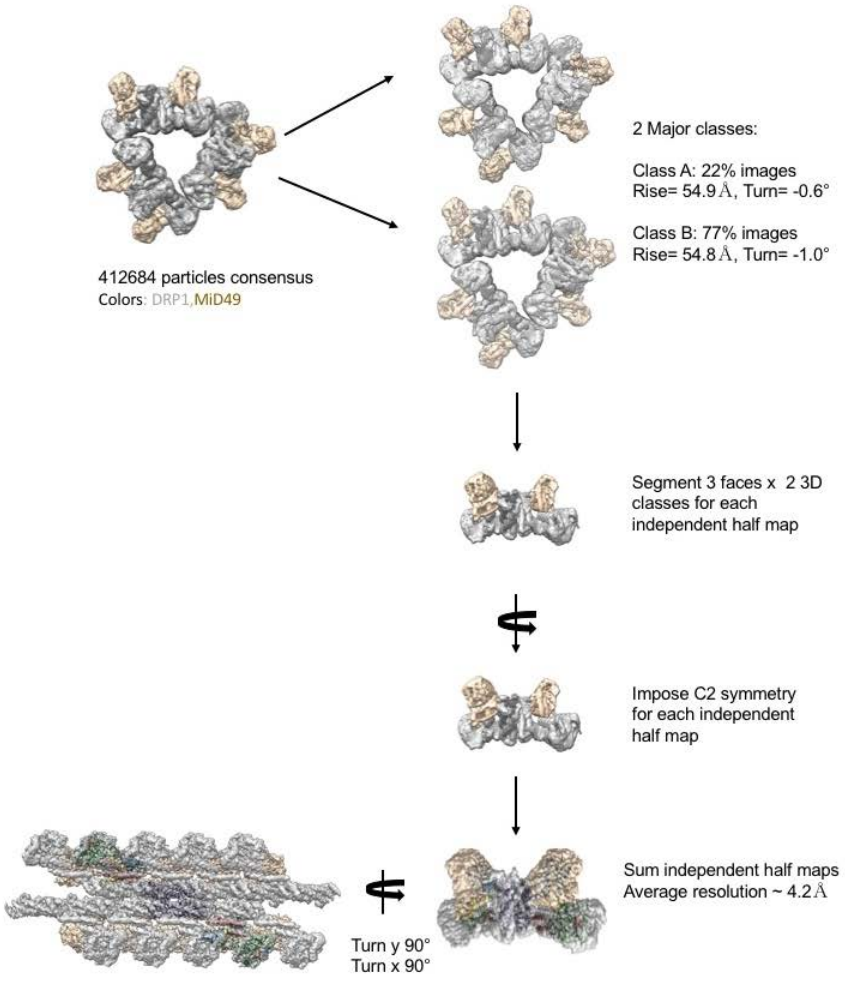

Extended data figure 4: Raw particle numbers and workflow for the reconstruction protocol and imposition of symmetries. DRP1 density is rendered in grey, MID49 in golden yellow.

Kalia, et al.
Extended Data Fig. 5

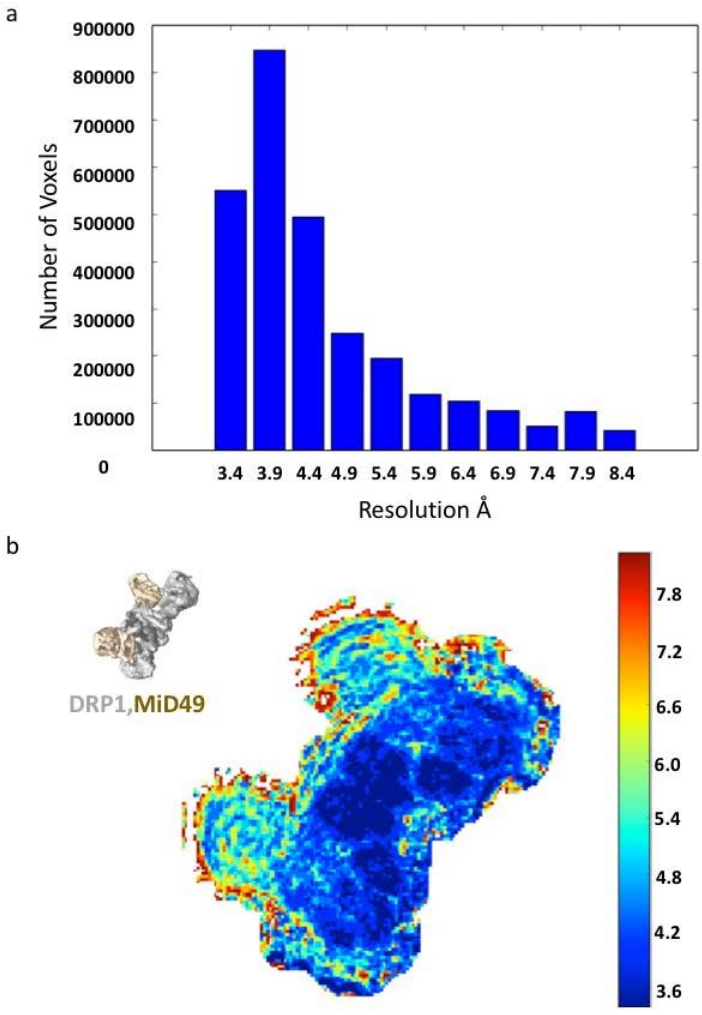

Extended data figure 5: Local resolution estimates computed by Resmap[25]. **(a)** Histogram of voxels values, and **(b)** Heat map of local resolution estimates displayed for a cross-section through the reconstruction.

Kalia, et al.
Extended Data Fig. 6

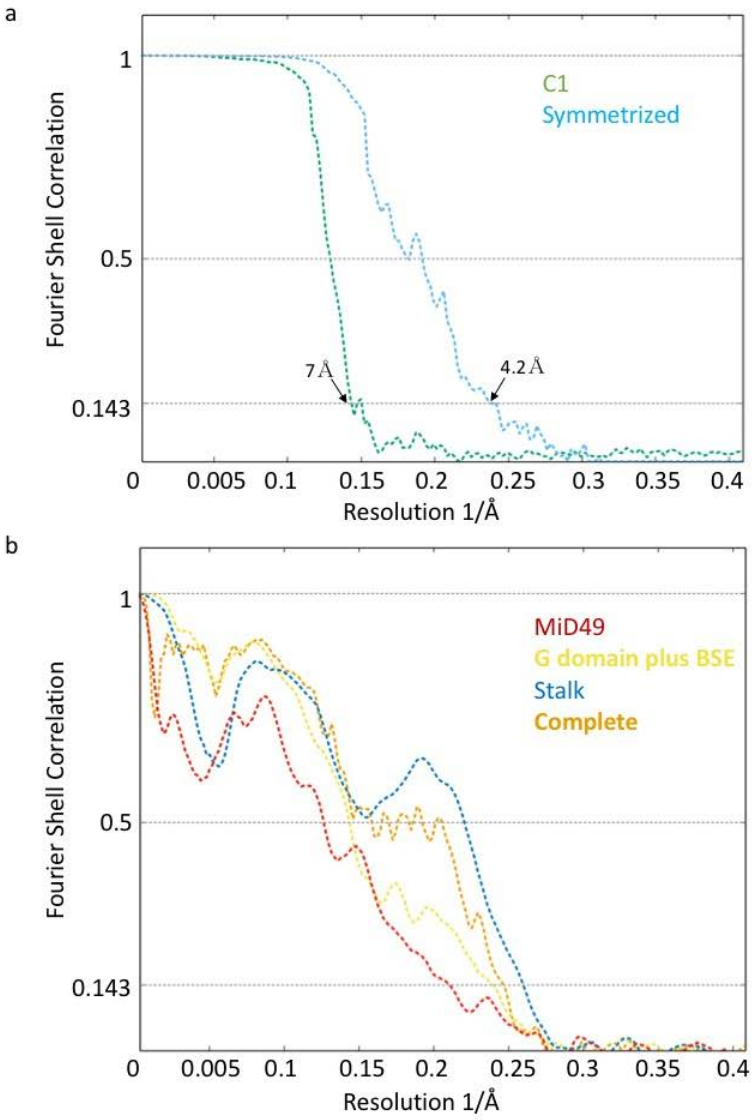

Extended data figure 6: Fourier Shell Correlation plots for **(a)** the half-maps with and without imposed symmetry; and **(b)** model-to-map correlations for the averaged as well as each sub-region of the structure using the atomic coordinates and B-factors determined using Rosetta.

Kalia, et al.
Extended Data Fig. 7

a

```
                1       10        20        30        40        50        60
MiD49_Mouse     MAEFSQKQRKQSGSEGLGSVVDFLLANARLVLGVGGAAVLGIATLAVKRLIDRATSPPDE
MiD49_Human     MAEFSQKRGKRRSDEGLGSMVDFLLANARLVLGVGGAAVLGIATLAVKRFIDRATSPRDE

                       70        80        90       100       110       120
MiD49_Mouse     DDTKGDSWKELSLLRATSPQKPQPPPAAFSQPLATGSPSPSVPVEPTPIHSPTTPKFSTI
MiD49_Human     DDTKADSWKELSLLRATPHLQPRPPPAALSQPVLPLAPSSSAPEGPAETDPEVTPQLSSP

                      130       140       150       160       170       180
MiD49_Mouse     APLCLTFQERLLAFERKHVITPEAHVTLAKQLAGDIALELQAYLRSKFPELPFGALVPGG
MiD49_Human     APLCLTLQERLLAFERDRVTIPAAQVALAKQLAGDIALELQAYFRSKFPELPFGAFVPGG

                      190       200       210       220       230       240
MiD49_Mouse     PLYDGLQAGTAEHVRLLAPLELEPGLWSLVPGVDTVAREPRCWAVRRTQLEFHPRGCSPW
MiD49_Human     PLYDGLQAGAADHVRLLVPLVLEPGLWSLVPGVDTVARDPRCWAVRRTQLEFCPRGSSPW

                      250       260       270       280       290       300
MiD49_Mouse     DRFLVGGYLSSRVLLELLRKALSASVNWPAIGSLLGCLIWPDVASEELLLKVQHECLEFT
MiD49_Human     DRFLVGGYLSSRVLLELLRKALAASVNWPAIGSLLGCLIRPSMASEELLLEVQHERLELT

                      310       320       330       340       350       360
MiD49_Mouse     LAVLMVVPGASTDDRLLLAWPLEGLASNLWLQDLYPVETARLRALDDQDAGTRRRLLLLL
MiD49_Human     VAVLVAVPGVDADDRLLLAWPLEGLACNLWLQDLYPVEAARLRALDDHDAGTRRRLLLLL

                      370       380       390       400       410       420
MiD49_Mouse     CGICRGHPALVRLGWSHLTQVVLHLGEEEVANTEEALGERFLQALEFLVGSLEQASLPCH
MiD49_Human     CAVCRGCSALGQLGRGHLTQVVLRLGEDNVDNTEEALGERFLQALELLHGSLEQASLPCH

                      430       440       450
MiD49_Mouse     FNPSVNLLGNFREEEIDDIGYVLYSGLQVPESLF
MiD49_Human     FNPSVNLFSSLREEEIDDIGYALYSGLQEPEGLL
```

b

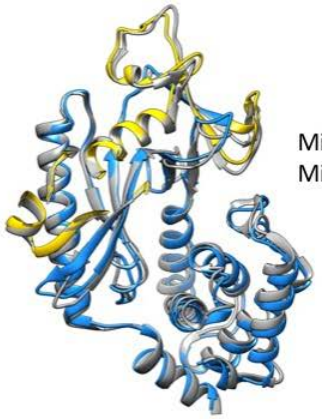

MiD49 human (this study)
MiD49 mouse (PDB:4WOY)

Extended data figure 7: Modeling of human MID49. **(a)** Sequence alignment between human and mouse MID49 sequences. **(b)** Overlay of the homology model of human $MID49_{126-454}$ (blue, with yellow DRR, ribbon) modeled within the cryoEM density versus the mouse MID49 crystal structure (PDB ID: 4WOY, grey ribbon)[6].

Kalia, et al.
Extended Data Fig. 8

a

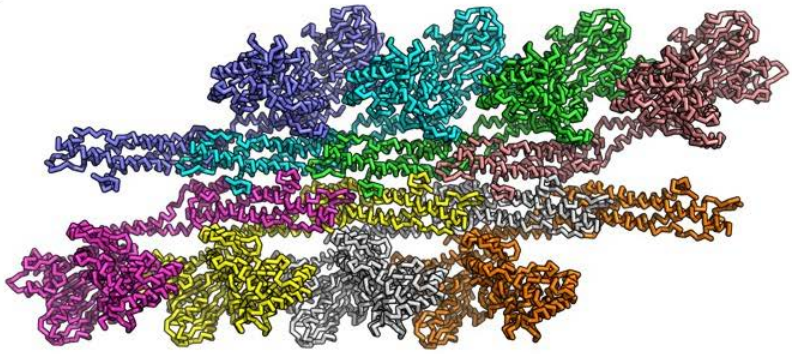

b

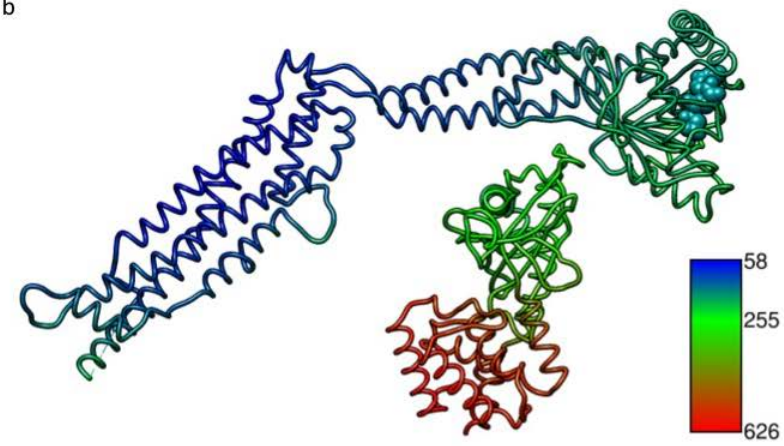

Extended data figure 8: Rosetta refinement. **(a)** Symmetric unit of the filament with 8 chains of DRP1 and 8 chains of MID49 refined using Rosetta to enforce symmetry and account for all possible inter-molecular interfaces. **(b)** Atomic B-factors for the DRP1 and MID49 models (ribbon) and bound GMPPCP (space filling).

Kalia, et al.
Extended Data Fig. 9

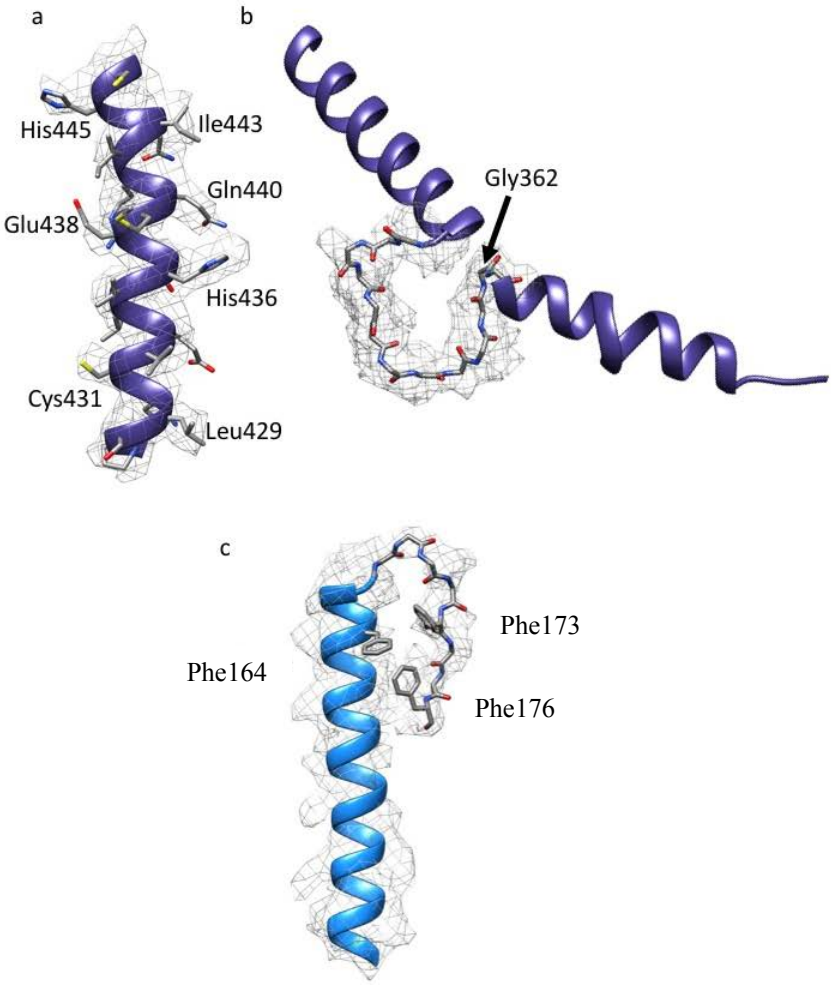

Extended data figure 9: Examples of model fitting to B-factor sharpened density for **(a)** a helix from the DRP1 stalk, **(b)** the backbone of the L1N^{S} loop, and **(c)** a helix and loop from MID49.

Kalia, et al.
Extended Data Fig. 10

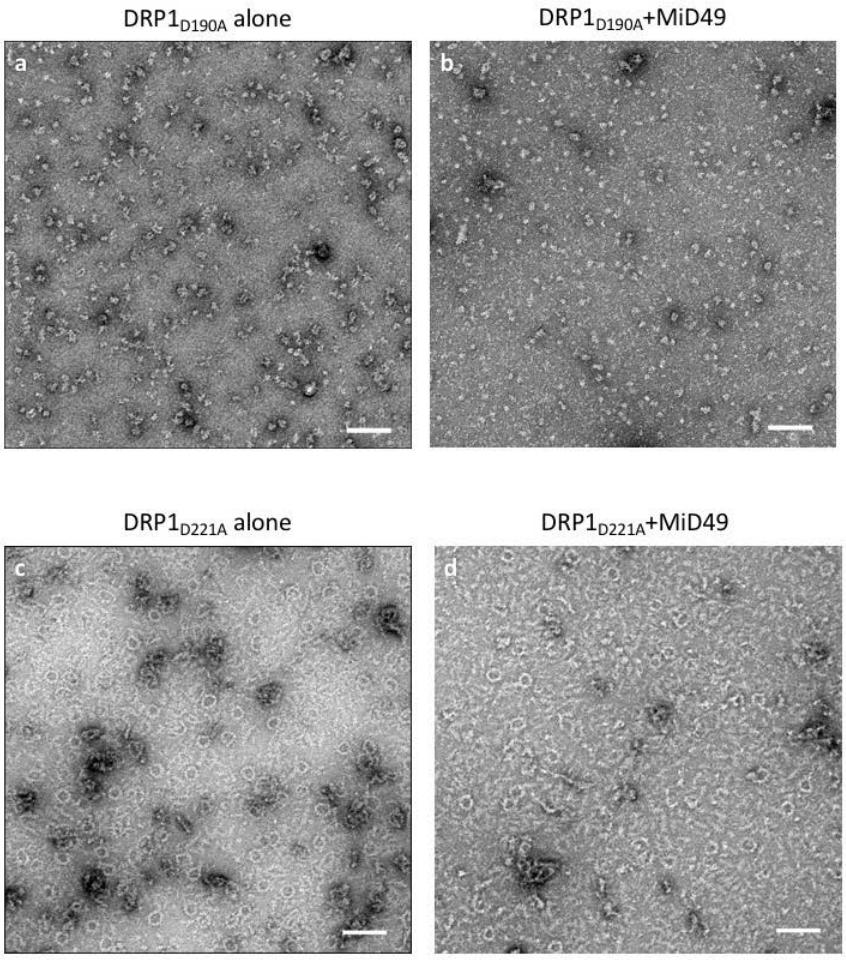

Extended data figure 10: DRP1 assembly and coassembly reactions with GMPPCP for **(a)** $DRP1_{D190A}$ alone, **(b)** $DRP1_{D190A}$+MID49, **(c)** $DRP1_{D221A}$ alone, and **(d)** $DRP1_{D221A}$+MID49. Bars = 100nm.

Kalia, et al.
Extended Data Fig. 11

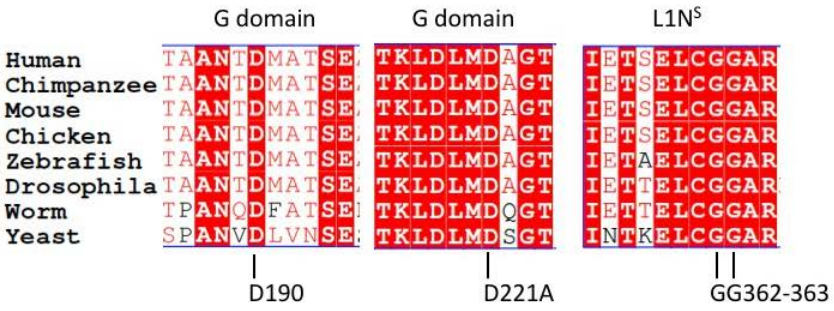

Extended data figure 11: Multiple sequence alignment of the regions near and including the DRP1 residues mutated in this study: D190, D221 and G362. The residue numbers apply to human DRP1, isoform 2 (UNIPROT identifier: O00429-3 also known as DLP1a).

Kalia, et al.
Extended Data Fig. 12

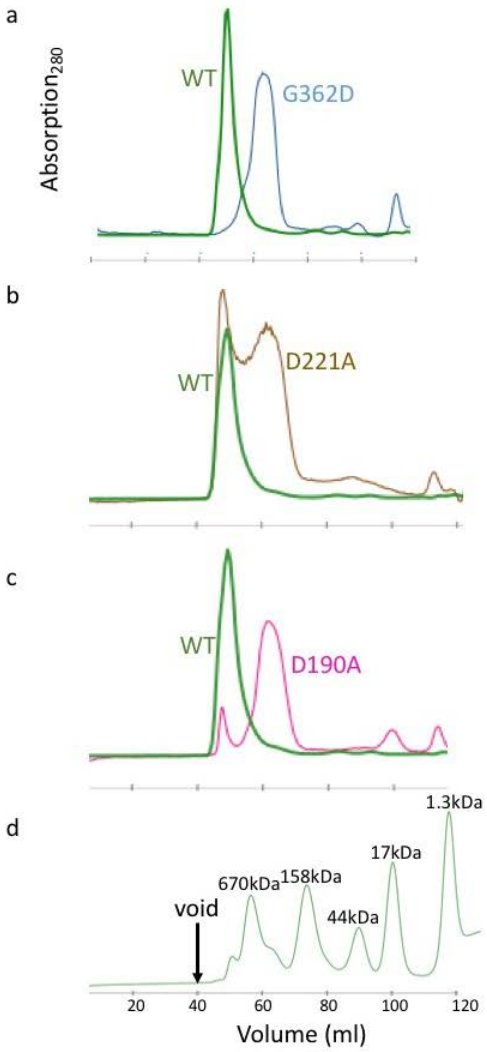

Extended data figure 12: Size exclusion chromatography traces for DRP1 wild-type and mutants used in the study. **(a)** Comparison between wild type (WT) versus $DRP1_{G362D}$, **(b)** WT versus $DRP1_{D221A}$, and **(c)** WT versus $DRP1_{D190A}$. **(d)** Standards for molecular weight comparison.

Kalia, et al.
Extended Data Fig. 13

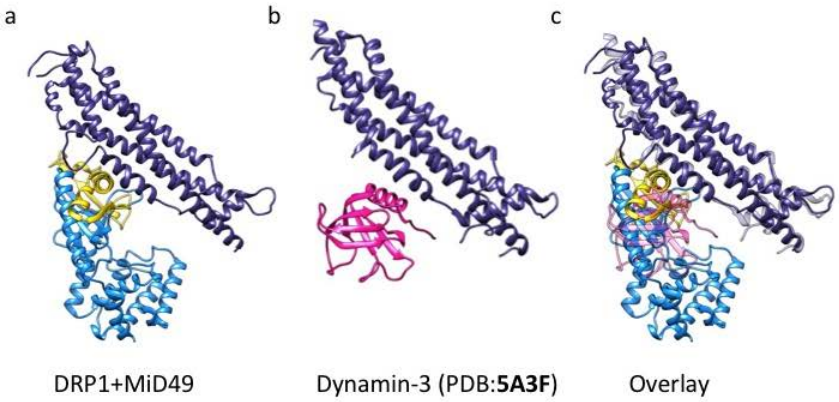

Extended data figure 13: Structural similarities between the third DRP1-MID49 interaction interface that includes the L1N^{S} loop and the interaction between the Pleckstrin Homology (PH) domain and the stalk of Dynamin-3 (PDB ID:5A3F)[26]. **(a)** DRP1-MID49 interaction at MID-interaction interface 3, **(b)** the PH domain bound to the stalk of Dynamin-3, and **(c)** Overlay of a and b.

Kalia, et al.
Extended Data Fig. 14

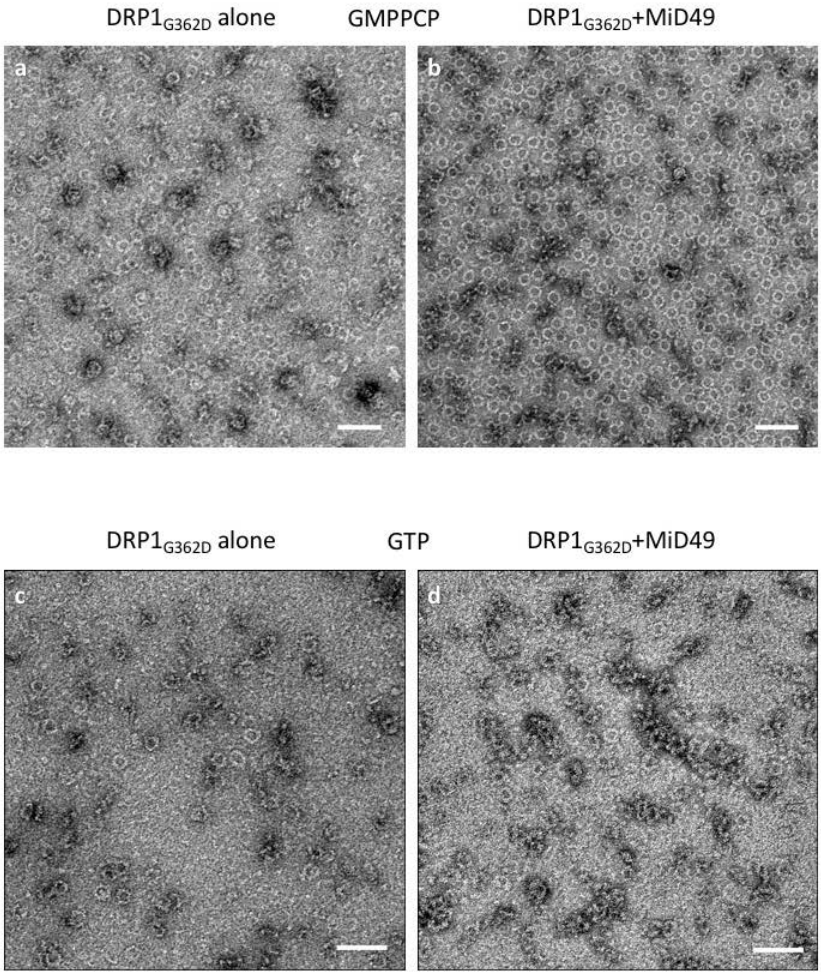

Extended data figure 14: $DRP1_{G362D}$ assembly and coassembly reactions with GMPPCP or GTP. $DRP1_{G362D}$ forms rings but not linear filaments without MID49 **(a,c)**; and with MID49 present **(b,d)**; with GMPPCP **(a-b)**; or with GTP **(c-d)**. Bars = 100 nm.

Kalia, et al.
Extended Data Fig. 15

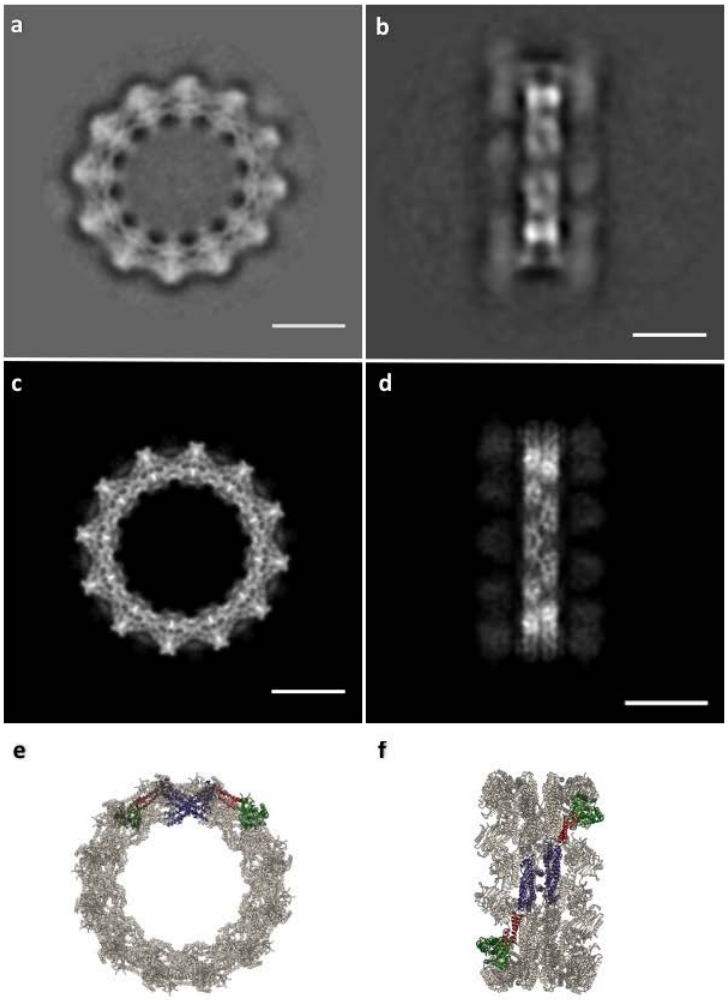

Extended data figure 15: $DRP1_{G362D}$ forms 12-dimer closed rings. **(a)** 2D class average of the rings; **(b)** 2D class average of infrequent, orthogonal or "side" views used as a constraint during model building; **(c)** "top" and **(d)** "side" projections of the model; **(e)** "top" and **(f)** "side" views of the final model rendered as ribbons. Bars =100Å. Green: G-domain, Red: Bundle Signaling Element (BSE), Purple: Stalk region.

Extended data movie Legends

Extended data movie 1: Nucleotide-induced conformational changes in the G-domain and Bundle Signaling Element (BSE).

Extended data movie 2: Nucleotide-induced conformational changes in the G-domain and Bundle Signaling Element (BSE) in the context of a full-length DRP1 dimer ("side" view).

Extended data movie 3: Nucleotide-induced conformational changes in the G-domain and Bundle Signaling Element (BSE) in the context of a full-length DRP1 dimer ("top" view).

Extended data movie 4: MID receptors engage a specific nucleotide-bound conformation of DRP1 tetramers and promote formation of a linear copolymer. Subsequent nucleotide hydrolysis and exchange promotes receptor dissociation and tetramer bending in the closed rings.

Extended data References

1 Gibson, D. G. *et al.* Enzymatic assembly of DNA molecules up to several hundred kilobases. *Nat Methods* **6**, 343-345, doi:10.1038/nmeth.1318 (2009).

2 Kalia, R., Talledge, N. & Frost, A. Structural and functional studies of membrane remodeling machines. *Methods in cell biology* **128**, 165-200, doi:10.1016/bs.mcb.2015.02.007 (2015).

3 Blommel, P. G., Becker, K. J., Duvnjak, P. & Fox, B. G. Enhanced Bacterial Protein Expression During Auto-induction Obtained by Alteration of Lac Repressor Dosage and Medium Composition. *Biotechnol Prog* **23**, 585-598, doi:10.1021/bp070011x (2007).

4 Studier, F. W. Protein production by auto-induction in high density shaking cultures. *Protein Expr Purif* **41**, 207-234 (2005).

5 Frohlich, C. *et al.* Structural insights into oligomerization and mitochondrial remodelling of dynamin 1-like protein. *Embo J* **32**, 1280-1292, doi:10.1038/emboj.2013.74 (2013).

6 Loson, O. C. *et al.* Crystal structure and functional analysis of MiD49, a receptor for the mitochondrial fission protein Drp1. *Protein Sci* **24**, 386-394, doi:10.1002/pro.2629 (2015).

7 Mastronarde, D. N. Automated electron microscope tomography using robust prediction of specimen movements. *Journal of structural biology* **152**, 36-51 (2005).

8 Zheng, S. Q. *et al.* MotionCor2: anisotropic correction of beam-induced motion for improved cryo-electron microscopy. *Nat Methods* **14**, 331-332, doi:10.1038/nmeth.4193 (2017).

9 Zhang, K. Gctf: Real-time CTF determination and correction. *Journal of structural biology* **193**, 1-12, doi:10.1016/j.jsb.2015.11.003 (2016).

10 Rohou, A. & Grigorieff, N. CTFFIND4: Fast and accurate defocus estimation from electron micrographs. *Journal of structural biology* **192**, 216-221, doi:10.1016/j.jsb.2015.08.008 (2015).

11 Bell, J. M., Chen, M., Baldwin, P. R. & Ludtke, S. J. High resolution single particle refinement in EMAN2.1. *Methods* **100**, 25-34, doi:10.1016/j.ymeth.2016.02.018 (2016).

12 Scheres, S. H. W. Semi-automated selection of cryo-EM particles in RELION-1.3. *Journal of structural biology* **189**, 114-122, doi:10.1016/j.jsb.2014.11.010 (2015).

13 Egelman, E. H. Reconstruction of helical filaments and tubes. *Methods Enzymol* **482**, 167-183, doi:10.1016/S0076-6879(10)82006-3 (2010).

14 Ge, P. *et al.* Cryo-EM model of the bullet-shaped vesicular stomatitis virus. *Science (New York, N.Y.)* **327**, 689-693, doi:10.1126/science.1181766 (2010).

15 Pintilie, G. D., Zhang, J., Goddard, T. D., Chiu, W. & Gossard, D. C. Quantitative analysis of cryo-EM density map segmentation by watershed and scale-space filtering, and fitting of structures by alignment to regions. *Journal of structural biology* **170**, 427-438, doi:10.1016/j.jsb.2010.03.007 (2010).

16 Goddard, T. D., Huang, C. C. & Ferrin, T. E. Visualizing density maps with UCSF Chimera. *Journal of structural biology* **157**, 281-287, doi:10.1016/j.jsb.2006.06.010 (2007).

17 Goddard, T. D., Huang, C. C. & Ferrin, T. E. Software extensions to UCSF chimera for interactive visualization of large molecular assemblies. *Structure* **13**, 473-482, doi:10.1016/j.str.2005.01.006 (2005).

18 Meng, E. C., Pettersen, E. F., Couch, G. S., Huang, C. C. & Ferrin, T. E. Tools for integrated sequence-structure analysis with UCSF Chimera. *BMC Bioinformatics* **7**, 339, doi:10.1186/1471-2105-7-339 (2006).

19 Pettersen, E. F. *et al.* UCSF Chimera--a visualization system for exploratory research and analysis. *J Comput Chem* **25**, 1605-1612, doi:10.1002/jcc.20084 (2004).

20 Wang, R. Y. *et al.* Automated structure refinement of macromolecular assemblies from cryo-EM maps using Rosetta. *eLife* **5**, doi:10.7554/eLife.17219 (2016).

21 Song, Y. *et al.* High-resolution comparative modeling with RosettaCM. *Structure* **21**, 1735-1742, doi:10.1016/j.str.2013.08.005 (2013).

22 DiMaio, F., Leaver-Fay, A., Bradley, P., Baker, D. & Andre, I. Modeling symmetric macromolecular structures in Rosetta3. *PloS one* **6**, e20450, doi:10.1371/journal.pone.0020450 (2011).

23 DiMaio, F. *et al.* Atomic-accuracy models from 4.5-A cryo-electron microscopy data with density-guided iterative local refinement. *Nature methods* **12**, 361-365, doi:10.1038/nmeth.3286 (2015).

24 Adams, P. D. *et al.* PHENIX: a comprehensive Python-based system for macromolecular structure solution. *Acta crystallographica. Section D, Biological crystallography* **66**, 213-221, doi:10.1107/S0907444909052925 (2010).

25 Kucukelbir, A., Sigworth, F. J. & Tagare, H. D. Quantifying the local resolution of cryo-EM density maps. *Nat Methods* **11**, 63-65, doi:10.1038/nmeth.2727 (2014).

26 Reubold, T. F. *et al.* Crystal structure of the dynamin tetramer. *Nature* **525**, 404-408, doi:10.1038/nature14880 (2015).

CHAPTER 5

DISCUSSION

5.1 Overview

In this dissertation, I present work that advances our understanding of mitochondrial division and dynamin structure. In Chapters 2 and 3, I present studies that describe the relevance and independence of the receptors of the mitochondrial fission dynamin Drp1. Using yeast genetics and fluorescence microscopy, we and our collaborators show that any individual receptor is sufficient to recruit Drp1 to mitochondria and to cause fission. In addition, I describe the purification, biochemical characterization, and coassembly of Drp1 with its receptor proteins. These methods have led us to understand the oligomeric properties of Drp1 in great detail.

The studies above led to the main focus of my dissertation, where I extend our work to the structural characterization of the coassembly of Drp1 and its receptor MiD49. Having assembled these proteins into linear filaments, I was able to visualize them using cryogenic electron microscopy. I subsequently used the newly developed methods of motion correction and image analysis to determine atomic level details of the complex of Drp1 and MiD49. These studies have led to the atomic resolution structure of Drp1 bound to MiD49 in a state that mimics the recruited state of the Drp1 molecule on the mitochondrial surface. We find that upon nucleotide binding, Drp1 undergoes a substantial elongation and this permits its interaction with the receptor protein. Using this structure, we have discovered new interfaces of interaction both on Drp1 and MiD49. In addition, our studies have identified the structural basis of a human disease allele, Glycine 362 of Drp1, which is present at the interaction interface of Drp1 and MiD49. Mutation of this residue causes encephalopathy in humans, as determined by sequencing of patient samples (Vanstone et al., 2016). The presence of this allele at the Drp1-

receptor interface and the phenotype of this mutation (elongated mitochondria) together suggest that such encephalopathies may result by an imbalance in mitochondrial dynamics owing to defective Drp1-receptor interaction.

Taken together, this work has extended our understanding of dynamin structure and function in multiple ways. In Chapter 3, we find that the receptors of Drp1 have evolved to have different structures but convergent and at least partially redundant functions. In addition, we discovered that the receptors can alter the oligomeric structure of Drp1, and thereby participate in Drp1-based fission activity. In Chapter 4, my work explains how MiD49 recruits Drp1 to the mitochondrial surface and how nucleotide binding enables Drp1 to bind MiD49. In addition, we observe how a path-dependent reaction converts a linear Drp1-MiD49 polymer to Drp1 rings that are mechanistically suited to constrict mitochondria. Future work on more receptors and more nucleotide states of Drp1 will be inspired by the work presented in this dissertation.

5.2 Multiple Receptors Regulate Mitochondrial Fission Dynamin Assembly

Fis1 (hFis1) is the only receptor of the mitochondrial fission dynamin that is conserved from yeast to humans. As described previously, yeast Fis1 plays a major role in mitochondrial division. It acts as a recruiter of the Mdv1/Caf4 receptors and this interaction is necessary for the recruitment of Dnm1, the yeast version of Drp1 (Cerveny & Jensen, 2003; Tieu et al., 2002). From our results in Chapter 3 and those of others (Osellame et al., 2016; Otera et al., 2010), it is now established that hFis1 has lost its function of mitochondrial division in mammalian systems. In addition, there is no known Mdv1/Caf4 homolog in mammals. Thus, only the transmembrane receptors MiD49/51

and Mff seem to function in mammalian mitochondrial fission.

An intriguing question is: Why does Drp1 have multiple different receptors in vertebrate cells? No study to date has demonstrated significant mechanistic differences in mitochondrial fission between the receptors. Some reports attribute differential functions to the receptors, suggesting that some receptors may negatively regulate fission (Zhao et al., 2011). This may be true for overexpression studies of MiD49/51, but other studies have definitively shown that at cellular expression levels, all receptors can support fission (Palmer et al. 2013; Osellame et al. 2016). Having three different receptor proteins could be in part related to Drp1 itself. Drp1 is known to undergo posttranslational modifications (PTMs) like phosphorylation, sumoylation, ubiquitination, and nitrosylation (Chang & Blackstone, 2007; Cho et al., 2009; Kar, Dey, & Rahaman, 2017; Taguchi, Ishihara, Jofuku, Oka, & Mihara, 2007; Wasiak, Zunino, & McBride, 2007; Yonashiro et al., 2006). The details of these processes and their implications are only beginning to be understood. It is possible that multiple Drp1 PTM states are differentially recognized by individual receptors. However, our yeast system in Chapter 3 could not have supported humanized PTM's on Drp1, yet Drp1 was recruited to mitochondria by each individual receptor. Thus, Drp1 PTM's may not be the only factor that drives receptor utilization. The developmental stage of the cell or environmental stress conditions may also be important in determining receptor specific roles.

It is intriguing to ask whether multiple receptors may work at the same fission site. Our studies in yeast suggest that each receptor is sufficient to recruit Drp1 and catalyze fission. Having said that, in a mammalian cell, multiple receptors could collaborate to increase the specificity and/or efficiency of division events. As discussed

below, I found that Drp1 interacted with MiD49 only in the presence of a GTP analog. Some authors have suggested that Drp1 may bind Mff in the apo (no nucleotide) state, suggesting that the recruitment of Drp1 by different receptors may depend on the nucleotide state of Drp1 (Francy et al., 2015). If true, this will have major implications on understanding the mechanism of mitochondrial division fully and warrants future investigation and structure-function studies. The Drp1-Mff co-assembly structure may show interesting differences compared to Drp1-MiD49 and may help us understand the requirement of multiple receptors by Drp1.

5.3 The Structure of Drp1 in Complex with MiD49

In Chapter 4, I determined the structure of Drp1 in complex with MiD49 in a nucleotide bound state. This structure is an important milestone in structure-function studies of dynamin-family proteins. To our knowledge, it is currently the only example of a cryo-EM structure of any full-length dynamin family protein at sub-nanometer resolution. The dynamin in the structure is in an active GTP-bound state that differs considerably in comparison to the apo-state structure. As a result of nucleotide binding, the protein displays a conformational change where Drp1 is significantly elongated, thereby revealing receptor binding sites. To my knowledge, this structure is also the only example that shows a dynamin in complex with any receptor protein. Analysis of the structure reveals how conserved Drp1 interfaces contribute towards a linear assembly, while the nucleotide binding helps interaction with the receptor (Figure 5.1). I also identified biochemical conditions that promote the dissociation of these infinite linear polymers into ring-like structures, reminiscent of the ring-like states known for endocytic

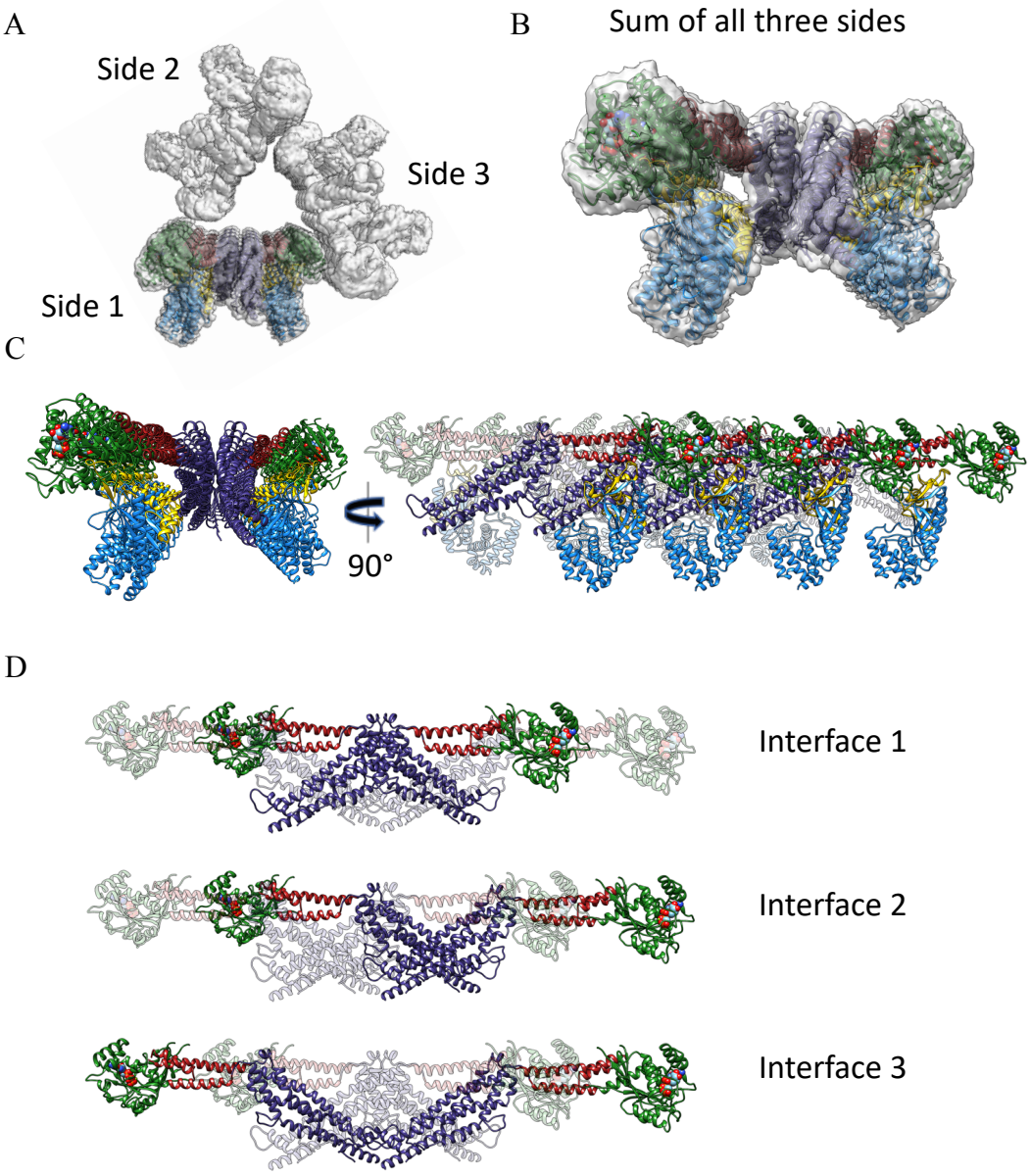

Figure 5.1: Breakdown of the structure to depict the observed Drp1 interfaces:
A) The triangular structure in cross section, side 1 has the model fit in density.
B) Sum of the three sides with the model fit in density.
C) Same as **(B)** but without density. The rotated view shows 8 chains each of Drp1 and MiD49 in a linear arrangement, 4 solid chains of each towards the reader. The chains away from the reader are rendered transparent.
D) Just the tetramer of Drp1, with stalk interfaces 1, 2, and 3 conserved in the dynamin family rendered solid.

dynamins and MxA (Klockow et al., 2002; Kochs et al., 2006). We propose that this conversion of the linear filament into the ring state constricts mitochondria and assists in the fission process.

Previous structural studies of dynamins have utilized truncated and/or mutated versions of the protein to facilitate crystallization (Faelber et al., 2011; Fröhlich et al., 2013; Reubold et al., 2015). Using such constructs, the nucleotide-bound state of the G-domain and the BSE of Drp1 and that of endocytic dynamins have been visualized (Chappie et al., 2010). The hallmark of such structures has been the switch loop movements within the G-domain and the movements within the G-BSE hinge. These movements in the molecule, compared to a powerstroke, have been informative, yet their impact on the full-length molecule has remained unclear.

In our studies in Chapter 4, I use full-length, unmutated Drp1 and the GTP analog GMPPCP for structural studies. Since dynamin samples polymerize under such conditions, they are unlikely to form macroscopic crystals necessary for X-ray diffraction-based studies. We used this situation to our advantage, instead utilizing cryo-EM, where we can freeze these samples under polymerization-enabling conditions and visualize them with electrons instead of X-rays. No crystals are required for such studies and recent developments in single-particle cryo-EM-based imaging and image analysis have enabled us to process our images to near atomic resolution.

The use of full-length Drp1 in this study has finally enabled us to look at nucleotide-dependent conformational changes in the dynamin family in the context of the complete polypeptide. Nucleotide binding causes G-domain switch-loop movements which are relayed to the G-BSE and the BSE-stalk hinges (Figure 4.2a-c). The hinge loop

movements collaborate to cause a 90º rotation of the G-domain and a 40Å movement downwards relative to the stationary stalk (Figure 4.2d). This movement exposes the residues of Drp1 involved in the receptor interfaces 1 & 2 for interaction with MiD49.

The presence of multiple binding interfaces and a large interaction surface collectively explain why point mutations of the dynamin recruitment region (DRR) did not disrupt the Drp1-MiD interaction in vivo. In these studies, a large segment of the DRR had to be removed to see any effect on MiD-based mitochondrial recruitment of Drp1 (Richter et al., 2014). Nevertheless, with the help of our structure, we have recently determined that the Drp1 mutant S611D (discussed ahead, receptor interface 4) and MiD49 mutant R235E both inhibit Drp1-MiD49 interactions. Future studies should focus on Mff, whose predicted structure is different than the MiDs and remains unknown. Such studies will enable us to build a complete picture of Drp1-receptor interactions.

5.3.1 The triangular structure and the functional single sides within it. The path-dependent reaction where the Drp1-MiD49 linear filament breaks up into shorter segments that then curls into rings (Figure 4.3) is reminiscent of the dynamic instability of microtubules (Mitchison & Kirschner, 1984). The shorter intermediates in this reaction, resemble each of the single sides of the triangular filaments in shape and measurement (Figure 4.3). This observation supports the idea that the triangular structure is a fortunate artifact of assembly of three functional sides. Moreover, the interaction between these sides stabilizes the complete oligomer and adds symmetry-related units that can be averaged for structure determination. We recently found that a structure-based mutant of Drp1, E116R, inhibited the trimeric assembly and formed only single-sided filaments when assembled with MiD49. Although shorter, these filaments were linear

(like those in Figure 4.3b), suggesting that the trimeric assembly interfaces helped to introduced stability in the oligomer but the linear assembly with MiD49 is not an artifact of these triangular contacts.

The single side of our structure is a functional assembly because the interfaces within it (e.g., the DRR, $Drp1_{S611}$, $Drp1_{G362}$) have important functional correlates in vivo (Cereghetti et al., 2008; Losón et al., 2015; Vanstone et al., 2016). Moreover, it is this assembly that undergoes curling, giving rise to rings. This conformational plasticity has important consequences in the context of mitochondrial membranes. Multiple studies have reported that Drp1 may assemble on the outer mitochondrial membranes (OMM), but not all assemblies lead to fission (Ji et al. 2015). I propose that the linear intermediates containing MiD49 assemble on the OMM and these assemblies wait for specific signals, yet undiscovered, to convert from the linear to the ring state. The linear assemblies are Drp1-specific and comprise an important mechanistic difference between Drp1 and endocytic dynamins. Mitochondrial membranes are locally very flat surfaces and Drp1 may have evolved to form long, linear assemblies so that it can fully encircle mitochondria.

5.4 How Do Mitochondria Divide? The Role of the Receptors and the Emerging Model

The function of the receptor proteins in mitochondrial fission has been widely studied. Receptor colocalization with Drp1 suggests that the receptor proteins may comprise an integral component of the ultimate fission machine that divides mitochondrial membranes (Otera et al., 2010; Palmer et al., 2011). Alternatively, the role

of the receptors may simply be to recruit Drp1. Two observations support the latter model. First, the ring structure of Drp1 that we believe is capable of constricting mitochondria, revealed no density for MiD49 in our structural studies. Secondly, new roles have been proposed for the endocytic dynamin protein Dyn2 in catalyzing the final membrane scission step (Lee, Westrate, Wu, Page, & Voeltz, 2016). The latter observation suggests that the ultimate fission machinery for mitochondria is similar to the assembly that operates on endocytic necks. The job of the receptor may therefore simply be to increase the avidity of Drp1 binding to membranes, by increasing the Drp1 concentration and enabling the formation of stable linear polymers. Upon specific signals that are yet to be discovered, the recruited Drp1 polymers could curl to constrict mitochondria and Dyn2 could then come in to catalyze the final cut.

Taken together, my work has led to an emerging model for mitochondrial fission that comprises of 3 major steps (Figure 5.2). 1) MiD49 or another receptor recruits Drp1 to the mitochondrial surface and forms linear co-assemblies on the mitochondrial outer membrane. 2) Drp1 hydrolyzes GTP and releases the receptor molecules, which diffuse into the nearby membrane space. Drp1 then binds another molecule of GTP, abundantly present in the cytosol, to undergo the nucleotide-induced conformational change again. This time, due of the absence of a receptor, the G-domain and BSE show a more pronounced downward movement relative to the stalk and the linear assembly curls into rings. The ring state constricts the mitochondria, but the mitochondria do not divide. 3) Finally, the endocytic dynamin Dyn2 finds a membrane constriction comparable to an endocytic neck, perfectly suited for it to bind and catalyze membrane fission.

Figure 5.2: **A Hypothetical Model for Mitochondrial Fission Following Drp1 Recruitment**: Step1: Drp1 is recruited by a receptor protein, in this case MiD49. Step 2: After GTP hydrolysis and release of the receptor, Drp1 oligomers form rings that constrict mitochondria down to 16nm. Step 3: Dyn2 arrives and organizes into helical polymers that carry out assembly mediated hydrolysis of GTP. G-domains for Dyn2 that interact for this purpose shown in blue. Fission takes place and the fission machinery disperses. Dyn2 cartoon adapted from Kraus & Ryan 2017.

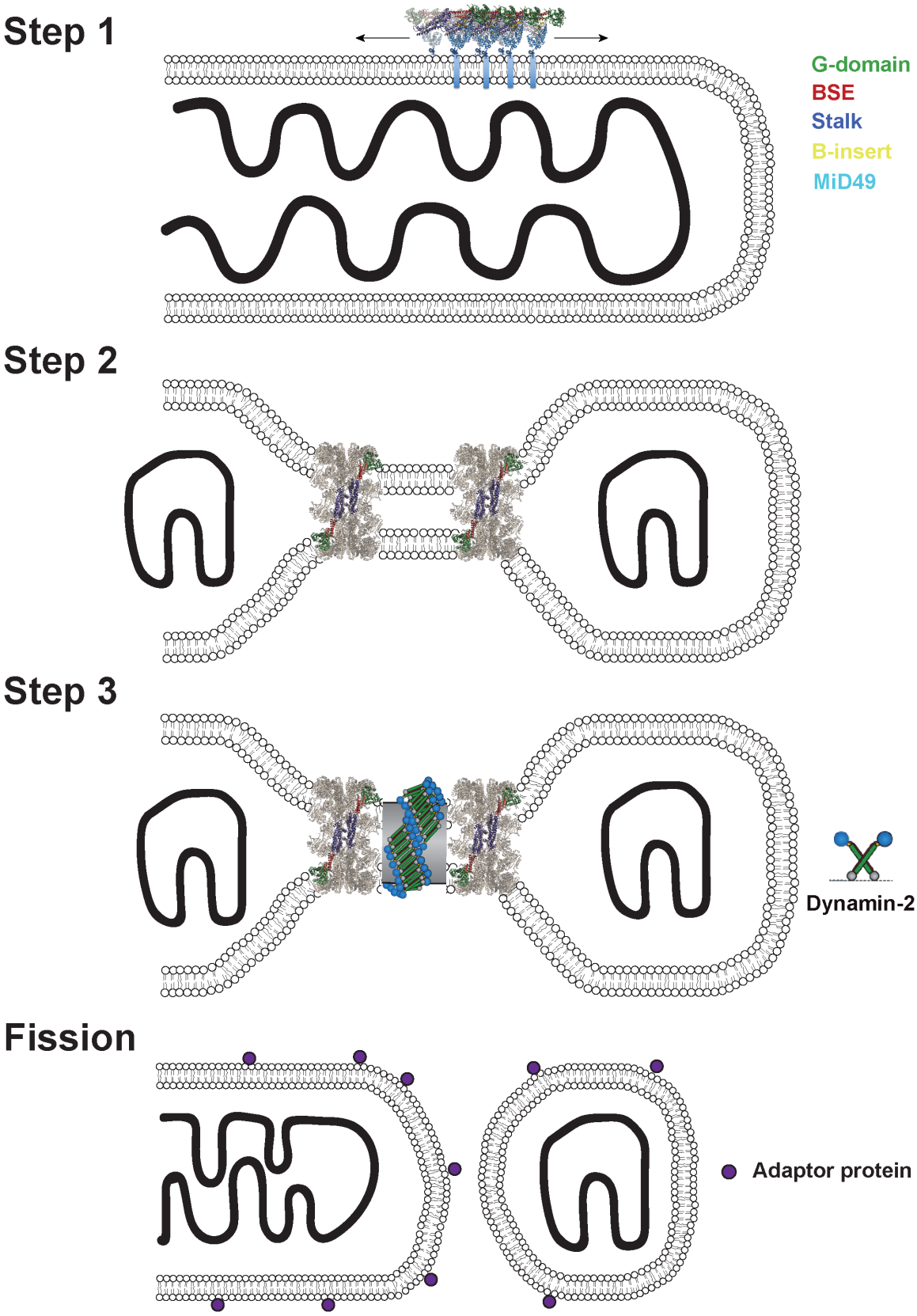
Step 1
G-domain
BSE
Stalk
B-insert
MiD49
Step 2
Step 3
Dynamin-2
Fission
Adaptor protein

Some support for this model already exists. In our structures, Drp1 rings do not show any interaction between their G-domains. Consequently, the prevailing model that G-G interactions execute assembly-mediated hydrolysis of GTP and consequent constriction cannot apply to these structures. The exception to this would be if two rings come together to organize the same G-G interaction and further studies will test this hypothesis. If we assume that no inter ring G-G interaction takes place, then Drp1 is actually a constrictase and not a fissionase. This may be why an endocytic dynamin is required to complete the fission reaction. Once recruited, Dyn2 may oligomerize in helical arrays that lead to the canonical G-G interaction and GTP hydrolysis, leading to further constriction and membrane fission. The structural details of this final step await a high-resolution, GTP-bound structure of Dyn2 on membranes.

5.5 Posttranslational Modifications of Drp1 and Their Consequences on Mitochondrial Fission

Posttranslational Modifications (PTMs) regulate protein activity in a context dependent fashion. Biochemical moieties are added on to proteins by specific enzymes, modulating their charge, stability or binding to partner proteins. Multiple PTMs are known to regulate the activity of Drp1 and consequently mitochondrial fission. In light of our new structure and the interfaces observed within it, some of these are discussed below.

5.5.1 Phosphorylation. Phosphorylation of Drp1 at two key residues is known to regulate its activity. Protein kinase A (PKA) phosphorylates Drp1 at Serine 637 and this PTM inhibits Drp1 activity leading to mitochondrial elongation (Chang & Blackstone,

2007). It was also shown that a Drp1 phosphomimetic mutant, S637D, was cytosolic and defective for mitochondrial recruitment (Cereghetti et al., 2008). Exercise, β-adrenergic signaling, starvation and mTOR pathway inhibition are all known to cause S637 phosphorylation of Drp1 (Gomes, Benedetto, & Scorrano, 2011; Rambold, Kostelecky, Elia, & Lippincott-Schwartz, 2011). During starvation, this PTM of Drp1 leads to elongated mitochondria. The consequence of this elongation is increased ATP production and prevention of phagocytosis of the organelle (Mishra & Chan, 2016). Phosphorylation of Drp1 at S637 is reversible. The phosphatases Calcinuerin and PP2A cause dephosphorylation of Drp1 at S637 and promote mitochondrial fission (Cereghetti et al., 2008; Dickey & Strack, 2011). Calcineurin is activated by Ca^{2+} binding and is thus thought to regulate mitochondrial morphology in response to Ca^{2+} levels (Mishra & Chan, 2016).

MAP-Kinase signaling pathway protein Erk 1 phosphorylates Drp1 at S616 (Kashatus et al., 2015). This PTM is understood to enhance the fission activity of Drp1. In brown fat tissue, PKA has also been shown to phosphorylate Drp1 at S616 (Wikstrom et al., 2014). Since the MAP-Kinase machinery plays crucial roles in cancer progression, misregulation of Drp1 function via S616 phosphorylation may be linked to cancer (Mishra & Chan, 2016). Phosphorylation of Drp1 at S616 is carried out by multiple other kinases. The observation that this phosphorylation supports mitochondrial fission is also consistent across multiple organisms (Kar et al., 2017; Taguchi et al., 2007). Drp1 is not the only protein in the mitochondrial fission pathway that is regulated by phosphorylation. MFF undergoes phosphorylation by AMPK (AMP activated protein kinase) resulting in enhanced mitochondrial fission (Toyama et al., 2016).

How does phosphorylation control Drp1 activity? From our structure, some interesting observations can be made regarding one of these phosphorylation sites. Serine 637 (S611 in isoform 2 used in Chapter 4) resides at the tip of the stalk region and is extremely close to a MiD49 molecule at the receptor interface 4 (Figure 4.1). We hypothesized that phosphorylation of Drp1 at S611 should inhibit the interaction of Drp1 with MiD49. We now report that a phosphomimetic mutant of Drp1, S611D, has impaired interaction with MiD49 in our assembly assays (Figure 5.3). S616 (S590 in our isoform) lies more deeply within the B-insert region and phosphorylation of this residue may modulate Drp1 binding to the phospholipids of the OMM. This serine residue was not visible in our structure.

5.5.2 S-nitrosylation: This PTM involves the addition of a nitroso (NO) group to a cysteine residue and is understood to be important for the regulation of redox reactions (Broillet, 1999). Drp1 is known to be S-nitrosylated during Alzheimer's disease and Huntington's disease (Cho et al., 2009; Haun et al., 2013). Reports suggest that S-nitrosylation at C644 (C618 in isoform 2 used in our studies) promotes self-association of Drp1 and enhances its GTPase activity, which together promote mitochondrial fragmentation. Hyperfragmentation of mitochondria in the Alzheimer's and Huntington's diseases is then thought to contribute to neuronal damage (Cho et al., 2009; Haun et al., 2013; Nakamura et al., 2010). C618 in our structure is close to the tip of the stalk near the receptor interaction interface-4. Any PTM in this region is likely to affect both Drp1-Drp1 interactions and Drp1-MiD49 interactions. How S-nitrosylation at this residue enhances Drp1 self-association is an important question for future studies.

5.5.3 Ubiquitylation. MARCH-V is a ubiquitin ligase that ubiquitylates both

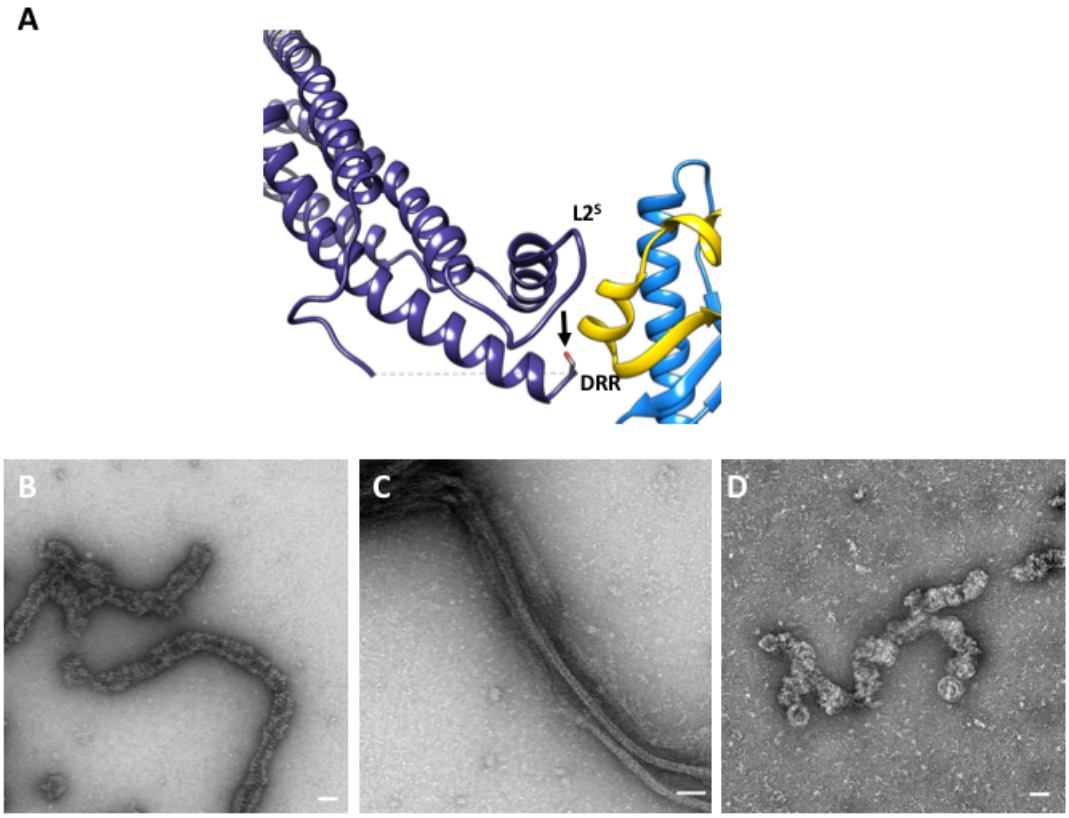

Figure 5.3: Drp1$_{S611D}$ displays impaired interaction with MiD49: A) A view of the receptor interface 4 showing S611 (arrow) in stick model. Dashed lines represent the residues of the B-insert not modeled in the structure. Purple: Drp1 stalk, Blue ribbon: MiD49$_{126-454}$, Yellow: DRR of MiD49. **B)** Drp1 assemblies in isolation. **C)** Drp1 assemblies with MiD49$_{126-454}$. **D)** Drp1$_{S611D}$ assemblies with MiD49$_{126-454}$ look like Drp1 assemblies in isolation. Scale Bars: 50nm.

Drp1 and MiD49 (Karbowski et al., 2007; Nakamura et al., 2006; Xu et al., 2016; Yonashiro et al., 2006). Absence or mutation of the RING CH-V domain of MARCH-V is known to cause aberrant Drp1 localization on the mitochondria, suggesting that in cells, ubiquitylation could play important roles in Drp1 recruitment on to mitochondria (Karbowski et al., 2007). Further, MARCH-V-based ubiquitylation causes proteasomal degradation of MiD49 and promotes mitochondrial fragmentation (Xu et al., 2016). In the light of our structural model, this is an interesting observation. Our model of mitochondrial fission describes a second round of GTP binding by Drp1 after it is recruited initially in the GTP-bound form. This second round of GTP binding enables the formation of the constriction-capable rings of Drp1. However, for the rings to form, MiD49 has to get out of the way in order to cause a more prominent downward motion of the Drp1 G-BSE relative to the stalk (Figure 4.4). Ubiquitylation based degradation of MiD49 could serve as a mechanism that promotes MiD49 recycling, ensuring the progression from the string to the ring state for the polymers described in this dissertation. Future work will test these ideas.

Drp1 is also ubiquitylated by the enzyme Parkin, and this modification is thought to have implications for apoptosis and Parkinson's disease (Tang et al., 2016). Ubiquitylation is also known to regulate the mitochondrial fusion machinery suggesting that it is an important PTM for cellular and mitochondrial homeostasis (Park et al., 2010; Park et al., 2014; Park et al., 2012).

5.5.4 Sumoylation. Addition of SUMO variant 1 to Drp1 stabilizes the membrane associated Drp1 fractions during mitosis and apoptosis (Harder, Zunino, & McBride, 2004; Montessuit et al., 2010; Wasiak et al., 2007). For mitosis, stabilization of

membrane associated Drp1 and resulting division of mitochondria could be related to the faithful distribution of the mitochondria amongst daughter cells. In the case of apoptosis, Drp1 association with the OMM is linked to the formation of the pro-apoptotic Bax oligomers on the mitochondrial surface which subsequently leads to the release of cytochrome C and cell death (Montessuit et al., 2010; Wasiak et al., 2007). SUMOylation of Drp1 takes place in the B-insert region on lysines 594, 597, 606, and 608 (Figueroa-Romero et al., 2009). SUMO variants 2 and 3 are also added to Drp1 in separate contexts and lead to a sequestering of Drp1 to the cytosol, preventing apoptosis via inhibition of Bax oligomer formation. Moreover, SUMOylation of Drp1 is reversible and deSUMOylation is catalyzed by enzymes such as SENP3 (Guo et al., 2013).

How SUMOylation alters Drp1 activity is a focus of active research. Like other PTM's, SUMOYlation may increase (in the case of SUMO 1 addition) or decrease (in the case of SUMO 2/3) membrane association given that the site of modification is the B-insert that interacts with the outer mitochondrial membrane. For example, addition of SUMO 1 may stabilize linear Drp1 polymers on the mitochondrial membrane by increasing the association of Drp1 with the OMM or the receptors.

5.6 Future Perspectives

Our work spanning the diverse fields of molecular biology, biochemistry, electron microscopy, and image analysis has enabled us to look at dynamin family proteins in a new light. The conformational changes that we have observed in Drp1 will likely apply to many if not all dynamin family proteins that sever biological membranes. Future studies will focus on the interaction of Drp1 with other receptors and interacting partners. In

addition, building these fission machines on membranes that mimic cellular conditions remains an unmet challenge. These studies will reveal if and how Drp1 engages differently with other receptors. Collectively, all these efforts should help us build a detailed molecular understanding of how Drp1 and other dynamins function to bring about membrane fission.

Our studies present a wonderful example of how simplified and reconstituted systems can yield high-resolution information that enables us to hypothesize phenomena in cellular contexts. Our results will help other investigators to design their own experiments on dynamin family proteins and other related systems. In addition, future structural studies on these or other protein complexes will focus on adding more components to get a better picture of how these assemblies form, move and how they are regulated.

With improved microscopes and image analysis techniques, we are not far from a future where purified solutions in a test tube will yield detailed structural models with minimum effort. Until that time, studies that focus on minimal systems will continue to enhance our understanding of biological assemblies and protein-based machineries. Solving one piece of the puzzle at a time, we should aim to build a composite high resolution picture of every part of the cell. Collectively these efforts will enable us to know, predict and even utilize the structure-function knowledge for practical use.

5.7 References

Broillet, M. C. (1999). S-nitrosylation of proteins. *Cellular and Molecular Life Sciences : CMLS*, *55*(8–9), 1036–42. https://doi.org/10.1007/s000180050354

Cereghetti, G. M., Stangherlin, A., de Brito, O. M., Chang, C. R., Blackstone, C.,

Bernardi, P., & Scorrano, L. (2008). Dephosphorylation by calcineurin regulates translocation of Drp1 to mitochondria. *Proceedings of the National Academy of Sciences*, *105*(41), 15803–15808. https://doi.org/10.1073/pnas.0808249105

Cerveny, K. L., & Jensen, R. E. (2003). The WD-repeats of Net2p interact with Dnm1p and Fis1p to regulate division of mitochondria. *Molecular Biology of the Cell*, *14*, 4126–4139. https://doi.org/10.1091/mbc.E03

Chang, C.-R., & Blackstone, C. (2007). Cyclic AMP-dependent protein kinase phosphorylation of Drp1 regulates Its GTPase activity and mitochondrial morphology. *Journal of Biological Chemistry*, *282*(30), 21583–21587. https://doi.org/10.1074/jbc.C700083200

Chappie, J. S., Acharya, S., Leonard, M., Schmid, S. L., & Dyda, F. (2010). G domain dimerization controls dynamin's assembly-stimulated GTPase activity. *Nature*, *465*(7297), 435–440. https://doi.org/10.1038/nature09032

Cho, D.-H., Nakamura, T., Fang, J., Cieplak, P., Godzik, A., Gu, Z., & Lipton, S. A. (2009). S-Nitrosylation of Drp1 Mediates β-Amyloid: Related mitochondrial fission and neuronal injury. *Science*, *324*(5923), 102–105. https://doi.org/10.2307/20493645

Dickey, A. S., & Strack, S. (2011). PKA/AKAP1 and PP2A/B 2 regulate neuronal morphogenesis via Drp1 phosphorylation and mitochondrial bioenergetics. *Journal of Neuroscience*, *31*(44), 15716–15726. https://doi.org/10.1523/JNEUROSCI.3159-11.2011

Faelber, K., Posor, Y., Gao, S., Held, M., Roske, Y., Schulze, D., … Daumke, O. (2011). Crystal structure of nucleotide-free dynamin. *Nature*, *477*(7366), 556–60. https://doi.org/10.1038/nature10369

Figueroa-Romero, C., Iniguez-Lluhi, J. A., Stadler, J., Chang, C.-R., Arnoult, D., Keller, P. J., … Feldman, E. L. (2009). SUMOylation of the mitochondrial fission protein Drp1 occurs at multiple nonconsensus sites within the B domain and is linked to its activity cycle. *The FASEB Journal*, *23*(11), 3917–3927. https://doi.org/10.1096/fj.09-136630

Francy, C. A., Alvarez, F. J. D., Zhou, L., Ramachandran, R., & Mears, J. A. (2015). The mechanoenzymatic core of Dynamin-Related Protein 1 comprises the minimal machinery required for membrane constriction. *Journal of Biological Chemistry*, (3), jbc.M114.610881. https://doi.org/10.1074/jbc.M114.610881

Fröhlich, C., Grabiger, S., Schwefel, D., Faelber, K., Rosenbaum, E., Mears, J., … Daumke, O. (2013). Structural insights into oligomerization and mitochondrial remodelling of dynamin 1-like protein. *The EMBO Journal*, *32*(9), 1280–1292. https://doi.org/10.1038/emboj.2013.74

Gomes, L. C., Benedetto, G. Di, & Scorrano, L. (2011). During autophagy mitochondria elongate, are spared from degradation and sustain cell viability. *Nature Cell Biology*, *13*(5), 589–598. https://doi.org/10.1038/ncb2220

Guo, C., Hildick, K. L., Luo, J., Dearden, L., Wilkinson, K. A., & Henley, J. M. (2013). SENP3-mediated deSUMOylation of dynamin-related protein 1 promotes cell death following ischaemia. *The EMBO Journal*, *32*(11), 1514–1528. https://doi.org/10.1038/emboj.2013.65

Harder, Z., Zunino, R., & McBride, H. (2004). Sumo1 conjugates mitochondrial substrates and participates in mitochondrial fission. *Current Biology*, *14*(4), 340–345. https://doi.org/10.1016/S0960-9822(04)00084-3

Haun, F., Nakamura, T., Shiu, A. D., Cho, D.-H., Tsunemi, T., Holland, E. A., … Lipton, S. A. (2013). S-Nitrosylation of Dynamin-Related Protein 1 mediates mutant huntingtin-induced mitochondrial fragmentation and neuronal injury in Huntington's disease. *Antioxidants & Redox Signaling*, *19*(11), 1173–1184. https://doi.org/10.1089/ars.2012.4928

Ji, W., Hatch, A. L., Merrill, R. A., Strack, S., & Higgs, H. N. (2015). Actin filaments target the oligomeric maturation of the dynamin GTPase Drp1 to mitochondrial fission sites. *eLife*, *4:e11553*(November), 1689–1699. https://doi.org/10.1017/CBO9781107415324.004

Kar, U. P., Dey, H., & Rahaman, A. (2017). Regulation of dynamin family proteins by post-translational modifications. *Journal of Biosciences*, *42*(2), 333–344. https://doi.org/10.1007/s12038-017-9680-y

Karbowski, M., Neutzner, A., & Youle, R. J. (2007). The mitochondrial E3 ubiquitin ligase MARCH5 is required for Drp1 dependent mitochondrial division. *Journal of Cell Biology*, *178*(1), 71–84. https://doi.org/10.1083/jcb.200611064

Kashatus, J. A., Nascimento, A., Myers, L. J., Sher, A., Byrne, F. L., Hoehn, K. L., … Kashatus, D. F. (2015). Erk2 phosphorylation of Drp1 promotes mitochondrial fission and MAPK-driven tumor growth. *Molecular Cell*, *57*(3), 537–552. https://doi.org/10.1016/j.molcel.2015.01.002

Klockow, B., Tichelaar, W., Madden, D. R., Niemann, H. H., Akiba, T., Hirose, K., & Manstein, D. J. (2002). The dynamin A ring complex: Molecular organization and nucleotide-dependent conformation changes. *Embo J.*, *21*(3), 240–250.

Kochs, G., Reichelt, M., Danino, D., Hinshaw, J. E., & Haller, O. (2006). Assay and functional analysis of dynamin-like Mx proteins. *Methods in Enzymology*, *404*(5), 632–643. https://doi.org/10.1016/S0076-6879(05)04055-3

Kraus, F., & Ryan, M. T. (2017). The constriction and scission machineries involved in

mitochondrial fission. *Journal of Cell Science*, *130*, 2953-2960. jcs.199562. https://doi.org/10.1242/jcs.199562

Lee, J. E., Westrate, L. M., Wu, H., Page, C., & Voeltz, G. K. (2016). Multiple dynamin family members collaborate to drive mitochondrial division. *Nature*, *540*(7631), 139–143. https://doi.org/10.1038/nature20555

Losón, O. C., Meng, S., Ngo, H., Liu, R., Kaiser, J. T., & Chan, D. C. (2015). Crystal structure and functional analysis of MiD49, a receptor for the mitochondrial fission protein Drp1. *Protein Science*, *24*(3), 386–394. https://doi.org/10.1002/pro.2629

Mishra, P., & Chan, D. C. (2016). Metabolic regulation of mitochondrial dynamics. *Journal of Cell Biology*, *212*(4), 379–387. https://doi.org/10.1083/jcb.201511036

Mitchison, T., & Kirschner, M. (1984). Dynamic instability of microtubule growth. *Nature*, *312*(5991), 237–242. https://doi.org/10.1038/312237a0

Montessuit, S., Somasekharan, S. P., Terrones, O., Lucken-Ardjomande, S., Herzig, S., Schwarzenbacher, R., … Martinou, J. C. (2010). Membrane remodeling induced by the dynamin-related protein Drp1 stimulates Bax oligomerization. *Cell*, *142*(6), 889–901. https://doi.org/10.1016/j.cell.2010.08.017

Nakamura, N., Kimura, Y., Tokuda, M., Honda, S., & Hirose, S. (2006). MARCH-V is a novel mitofusin 2- and Drp1-binding protein able to change mitochondrial morphology. *EMBO Reports*, *7*(10), 1019–1022. https://doi.org/10.1038/sj.embor.7400790

Nakamura, T., Cieplak, P., Cho, D. H., Godzik, A., & Lipton, S. A. (2010). S-Nitrosylation of Drp1 links excessive mitochondrial fission to neuronal injury in neurodegeneration. *Mitochondrion*, *10*(5), 573–578. https://doi.org/10.1016/j.mito.2010.04.007

Osellame, L. D., Singh, A. P., Stroud, D. A., Palmer, C. S., Stojanovski, D., Ramachandran, R., & Ryan, M. T. (2016). Cooperative and independent roles of Drp1 adaptors Mff and MiD49/51 in mitochondrial fission. *Journal of Cell Science*, *129*(April), 2170–2181. https://doi.org/10.1242/jcs.185165

Otera, H., Wang, C., Cleland, M. M., Setoguchi, K., Yokota, S., Youle, R. J., & Mihara, K. (2010). Mff is an essential factor for mitochondrial recruitment of Drp1 during mitochondrial fission in mammalian cells. *The Journal of Cell Biology*, *191*(6), 1141–58. https://doi.org/10.1083/jcb.201007152

Palmer, C. S., Elgass, K. D., Parton, R. G., Osellame, L. D., Stojanovski, D., & Ryan, M. T. (2013). MiD49 and MiD51 can act independently of Mff and Fis1 in Drp1 recruitment and are specific for mitochondrial fission. *The Journal of Biological Chemistry*. https://doi.org/10.1074/jbc.M113.479873

Palmer, C. S., Osellame, L. D., Laine, D., Koutsopoulos, O. S., Frazier, A. E., & Ryan, M. T. (2011). MiD49 and MiD51, new components of the mitochondrial fission machinery. *EMBO Reports*, *12*(6), 565–73. https://doi.org/10.1038/embor.2011.54

Park, Y.-Y., Cho, H., McBride, H., Neuspiel, M., Wasiak, S., Chan, D., … Youle, R. (2012). Mitofusin 1 is degraded at G2/M phase through ubiquitylation by MARCH5. *Cell Division*, *7*(1), 25. https://doi.org/10.1186/1747-1028-7-25

Park, Y.-Y., Lee, S., Karbowski, M., Neutzner, A., Youle, R. J., & Cho, H. (2010). Loss of MARCH5 mitochondrial E3 ubiquitin ligase induces cellular senescence through dynamin-related protein 1 and mitofusin 1. *Journal of Cell Science*, *123*(4), 619–626. https://doi.org/10.1242/jcs.061481

Park, Y. Y., Nguyen, O. T. K., Kang, H., & Cho, H. (2014). MARCH5-mediated quality control on acetylated Mfn1 facilitates mitochondrial homeostasis and cell survival. *Cell Death and Disease*, *5*(4), e1172-12. https://doi.org/10.1038/cddis.2014.142

Rambold, A. S., Kostelecky, B., Elia, N., & Lippincott-Schwartz, J. (2011). Tubular network formation protects mitochondria from autophagosomal degradation during nutrient starvation. *Proceedings of the National Academy of Sciences*, *108*(25), 10190–10195. https://doi.org/10.1073/pnas.1107402108

Reubold, T. F., Faelber, K., Plattner, N., Posor, Y., Ketel, K., Curth, U., … Noe, F. (2015). Crystal structure of the dynamin tetramer. *Nature*, *525*, 404–408. https://doi.org/10.1038/nature14880

Richter, V., Palmer, C. S., Osellame, L. D., Singh, A. P., Elgass, K., Stroud, D. A., … Ryan, M. T. (2014). Structural and functional analysis of MiD51, a dynamin receptor required for mitochondrial fission. *The Journal of Cell Biology*. *204*(4), 477-486. https://doi.org/10.1083/jcb.201311014

Taguchi, N., Ishihara, N., Jofuku, A., Oka, T., & Mihara, K. (2007). Mitotic phosphorylation of dynamin-related GTPase Drp1 participates in mitochondrial fission. *Journal of Biological Chemistry*, *282*(15), 11521–11529. https://doi.org/10.1074/jbc.M607279200

Tang, J., Hu, Z., Tan, J., Yang, S., & Zeng, L. (2016). Parkin protects against oxygen-glucose deprivation/reperfusion insult by promoting Drp1 degradation. *Oxidative Medicine and Cellular Longevity*, *2016*. https://doi.org/10.1155/2016/8474303

Tieu, Q., Okreglak, V., Naylor, K., & Nunnari, J. (2002). The WD repeat protein, Mdv1p, functions as a molecular adaptor by interacting with Dnm1p and Fis1p during mitochondrial fission. *Journal of Cell Biology*, *158*(3), 445–452. https://doi.org/10.1083/jcb.200205031

Toyama, E. Q., Herzig, S., Courchet, J., Lewis Jr., T. L., Losón, O. C., Hellberg, K., …

Franck Polleux, David C. Chan, Reuben J. Shaw. (2016). AMP-activated protein kinase mediates mitochondrial fission in. *Science*, *351*(6270), 275–281. https://doi.org/10.1126/science.aab4138

Vanstone, J. R., Smith, A. M., McBride, S., Naas, T., Holcik, M., Antoun, G., … Lines, M. A. (2016). DNM1L-related mitochondrial fission defect presenting as refractory epilepsy. *European Journal of Human Genetics*, *24*(7), 1084–1088. https://doi.org/10.1038/ejhg.2015.243

Wasiak, S., Zunino, R., & McBride, H. M. (2007). Bax/Bak promote sumoylation of DRP1 and its stable association with mitochondria during apoptotic cell death. *Journal of Cell Biology*, *177*(3), 439–450. https://doi.org/10.1083/jcb.200610042

Wikstrom, J. D., Mahdaviani, K., Liesa, M., Sereda, S. B., Si, Y., Las, G., … Shirihai, O. S. (2014). Hormone-induced mitochondrial fission is utilized by brown adipocytes as an amplification pathway for energy expenditure. *EMBO Journal*, *33*(5), 418–436. https://doi.org/10.1002/embj.201385014

Xu, S., Cherok, E., Das, S., Li, S., Roelofs, B. A., Ge, S. X., … Karbowski, M. (2016). Mitochondrial E3 ubiquitin ligase MARCH5 controls mitochondrial fission and cell sensitivity to stress-induced apoptosis through regulation of MiD49 protein. *Molecular Biology of the Cell*, *27*(2), 349–359. https://doi.org/10.1091/mbc.E15-09-0678

Yonashiro, R., Ishido, S., Kyo, S., Fukuda, T., Goto, E., Matsuki, Y., … Yanagi, S. (2006). A novel mitochondrial ubiquitin ligase plays a critical role in mitochondrial dynamics. *The EMBO Journal*, *25*(15), 3618–3626. https://doi.org/10.1038/sj.emboj.7601249

Zhao, J., Liu, T., Jin, S., Wang, X., Qu, M., Uhlén, P., … Nistér, M. (2011). Human MIEF1 recruits Drp1 to mitochondrial outer membranes and promotes mitochondrial fusion rather than fission. *The EMBO Journal*, *30*(14), 2762–2778. https://doi.org/10.1038/emboj.2011.198